Qualitative study of physical phenomena through geometry of complex foliations

Gabriela Gutierrez Guillen

THÈSE DE DOCTORAT DE L'ÉTABLISSEMENT
UNIVERSITÉ BOURGOGNE FRANCHE-COMTÉ

PRÉPARÉE À L'UNIVERSITÉ DE BOURGOGNE

École doctorale numéro 553
Carnot-Pasteur

Doctorat de mathématiques

Par
Gabriela Jocelyn GUTIERREZ GUILLEN

Qualitative study of physical phenomena through geometry of complex foliations

Thèse présentée et soutenue à Dijon, le 22 février 2024

Composition du Jury :

Pavao MARDESIC	Maître de conférences HDR (Université de Bourgogne)	Directeur de thèse
Dominique SUGNY	Professeur (Université de Bourgogne)	Directeur de thèse
Konstantinos EFSTATHIOU	Maître de conférences HDR (Duke Kunshan University)	Rapporteur
San VU NGOC	Professeur (Université de Rennes)	Rapporteur
Olga LUKINA	Maître de conférences HDR (Leiden University)	Examinateur
Daniel PANAZZOLO	Professeur (Université de Haute-Alsace)	Examinateur
Jose Luis JARAMILLO	Professeur (Université de Bourgogne)	Président

ECOLE DOCTORALE
CARNOT - PASTEUR

Titre : Étude qualitative des phénomènes physiques via la géométrie des feuilletages complexes

Mots clés : corps rigide, dynamique Hamiltonienne, monodromie Hamiltonienne, géométrie complexe, feuilletages complexes

Résumé : Cette thèse aborde deux sujets en physique mathématique : l'effet de la raquette de tennis et la monodromie hamiltonienne.
Grâce à une exploration approfondie de la géométrie sous-jacente, nous fournissons une description mathématique complète de l'effet de la raquette de tennis, un phénomène géométrique observé dans les rotations libres de corps rigides. Nous examinons l'existence, l'origine et la robustesse de cet effet en utilisant la géométrie complexe et la géométrie réelle. Nous détectons également des signatures de contraintes physiques sur les moments d'inertie du corps, dans la structure géométrique de l'effet de la raquette de tennis. L'analyse est étendue à des phénomènes étroitement liés tels que l'effet Dhzanibekov, le monster flip et la phase de Montgomery.
La deuxième partie de la thèse se concentre sur la monodromie Hamiltonienne, qui est l'obstruction topologique la plus simple à l'existence de coordonnées d'action-angles globales pour un système complètement intégrable. Nous montrons que l'utilisation de paires de Lax spectrales fournit une structure géométrique complexe qui permet l'étude de la monodromie Hamiltonienne et le calcul de la matrice de monodromie correspondante.
Tout au long de ce travail de recherche, nous adoptons un cadre général qui utilise des feuilletages complexes pour fournir une structure géométrique aux problèmes posés, ce qui permet de mieux comprendre les phénomènes physiques correspondant.

Title: Qualitative study of physical phenomena through geometry of complex foliations

Keywords: rigid body, Hamiltonian dynamics, Hamiltonian monodromy, complex geometry, complex foliations

Abstract: This thesis studies two topics in mathematical physics: the tennis racket effect and Hamiltonian monodromy.
Through an in-depth exploration of the underlying geometry, we provide a full mathematical description of the tennis racket effect, which is a geometric phenomenon observed in free rotational dynamics of rigid bodies. We examine the existence, origin, and robustness of this effect using the interplay between complex and real geometries. We also detect signatures of physical constraints on the moments of inertia of the body, in the geometric structure of the tennis racket effect. The analysis is extended to closely related phenomena such as the Dhzanibekov effect, the monster flip, and the Montgomery phase.
The second part of the thesis focuses on Hamiltonian monodromy, which is the simplest topological obstruction to the existence of global action-angle coordinates for a completely integrable system. We show that the use of spectral Lax pairs provides a complex geometric structure that enables the study of Hamiltonian monodromy and the calculation of the corresponding monodromy matrix.
Throughout this research work, we adopt a general framework that employs complex foliations to provide a geometric structure for the problems under study, leading to a deeper understanding of these phenomena.

UBFC UNIVERSITÉ BOURGOGNE FRANCHE-COMTÉ
Université Bourgogne Franche-Comté
32 avenue de l'Observatoire
25000 Besançon

ECOLE DOCTORALE
CARNOT - PASTEUR

ARTICLES

Title: Geometric origin of the tennis racket effect

Journal: Physical Review Letters (2020)

Abstract: The tennis racket effect is a geometric phenomenon that occurs in a free rotation of a three-dimensional rigid body. In a complex phase space, we show that this effect originates from a pole of a Riemann surface and can be viewed as a consequence of the Picard-Lefschetz formula. We prove that a perfect twist of the racket is achieved in the limit of an ideal asymmetric object. We give upper and lower bounds to the twist defect for any rigid body, which reveals the robustness of the effect. A similar approach describes the Dzhanibekov effect in which a wing nut, spinning around its central axis, suddenly makes a half-turn flip around a perpendicular axis and the Monster flip, an almost impossible skateboard trick.

Title: Geometrical signatures of physical constraints on rotating rigid bodies

Journal: Journal of Physics A: Mathematical and Theoretical (2023)

Abstract: We study signatures of physical constraints on free rotations of rigid bodies. We show analytically that the physical or non-physical nature of the moments of inertia of a system can be detected by qualitative changes both in the Montgomery phase and in the tennis racket effect.

Title: Hamiltonian monodromy via spectral Lax pairs

Journal: Journal of Mathematical Physics (2024)

Abstract: Hamiltonian Monodromy is the simplest topological obstruction to the existence of global action-angle coordinates in a completely integrable system. We show that this property can be studied in a neighborhood of a focus-focus singularity by a spectral Lax pair approach. From the Lax pair, we derive a Riemann surface which allows us to compute in a straightforward way the corresponding Monodromy matrix. The general results are applied to the Jaynes-Cummings model and the spherical pendulum.

Acknowledgments

First of all, I would like to thank my advisors Pavao Mardesic and Dominique Sugny, without whom this work would not have been possible. The process that led to this thesis has been a real teamwork, in which I learned mathematics from Pavao and physics from Dominique. I thank them for their great academic support.

I am also very grateful to the members of the jury: Konstantinos Efstathiou, San Vu Ngoc, Daniel Panazzolo, Jose Luis Jaramillo, and Olga Lukina. Thank you for kindly accepting to be part of the jury, for coming to Dijon, taking the time to read my work, and giving me valuable comments.

Una pieza fundamental para que estos tres años hayan sido posibles es mi familia. Gracias por criarme con tanto amor y darme todas las bases que me permitieron perseguir y cumplir todas mis metas y sueños. Gracias por siempre apoyarme en todos mis proyectos, los amo y los admiro profundamente a los tres. Gracias mamá por tu dulzura y complicidad, gracias papá por enseñarme a luchar por lo que quiero y gracias hermano por tu silenciosa ternura que reconforta a todos los que te rodeamos.

Pavao y Mirjana, quiero decirles que se convirtieron en mi familia Dijonesa, gracias por todo el apoyo y los domingos de mercado. La mayoría de las cosas prácticas de la vida en Francia las aprendí conversando con ustedes. Gracias por su enorme amabilidad, siempre les tendré mucho cariño a ustedes y a su familia.

A Laura Ortiz Bobadilla, mi asesora de licenciatura y maestría, le agradezco haberme formado como matemática. La forma de hacer matemáticas y muchos valores necesarios dentro de la academia los aprendí de usted. Gracias por su apoyo incondicional y siempre estar presente. A Juan José Borrego Cadena siempre le agradeceré el haberme introducido al mundo de las matemáticas y enseñarme que este es un mundo lleno de creatividad.

Thanks to Laila and Fede, I love and admire you deeply. In an environment mostly formed by men, it is a relief to be able to share the path with strong and wonderful women like you. Thank you for the support, love, and shared moments.

Óscar, gracias por estos casi 4 años de compañía, compañía personal y académica. Ha sido bonito el poder compartir todo el proceso del doctorado con alguien de México, con alguien con quien comparto la misma cultura, el mismo vocabulario y el mismo campo académico! Inti, gracias por tu infinita energía que contagia a todos de felicidad, tu autenticidad nos enseña a todos muchas lecciones. Pablo y Eddy, gracias por siempre estar ahí, cada uno con una manera muy distinta, pero siempre ahí. Les agradezco su apoyo a cada uno. En fin, los quiero mucho a los cuatro.

Lucas, I thank you for all your support, whenever I need something you don't hesitate for a second to tell me that you will do it, and although sometimes you make me angry :P, I am infinitely grateful for your unconditional support. Thanks to my roomies, Deniz and Dimitris, you are the people I spend more time with every day (because the three of us work too much haha) being in the office is better for sharing this space with you.

A la amiga más antigua que tengo, Cielito, quien diría que nos conoceríamos en una primaria de San Cristóbal de las Casas y que 20 años después ambas estaríamos en Francia haciendo un doctorado. Ha sido maravilloso tenerte aquí y poder compartir momentos, te quiero mucho. Julien, gracias por todo tu apoyo en las buenas y en las malas, agradezco mucho el haberte conocido en este proceso del doctorado y de seguir teniendote en mi vida.

To the french team: Thibaut, Armand, Arnaud, Edwin, Victor, vous êtes super sympas et je suis heureux de vous avoir rencontré. Alan, Felipe, Cris tienen un corazon super lindo, gracias por ser parte de este camino. Helal, thank you for showing me videos that made me happy all the time!

Thanks in general to the whole group of PhD students, you taught me that the world is more diverse than I could have ever imagined and with you I learned two languages, so without a doubt, you were a fundamental part of this process.

Enfin, merci à tous les membres de l'IMB, tout le monde m'a toujours bien accueilli et j'apprécie beaucoup la gentillesse de chacun.

Introduction

Historically, mathematics and physics developed side by side with very important interactions. Mathematical concepts help the understanding of physical phenomena and, at the same time, physics inspires the development of mathematics through experimental results. Nowadays, the importance of this vital symbiosis has been affected by the hyper-specialization; which often results in little interaction between the different scientific fields.

Aware of this problem, many scientists worldwide have become interested in strengthening links between different research areas, resulting in the development of these fields and even the emergence of new ones. Mathematical physics is an instance of this process since it is an area that brings mathematicians and physicists, with different backgrounds, to work together, allowing a better understanding of physical phenomena.

This research work is motivated by the fundamental idea of making different research fields interact. Specifically, the goal of this work is to connect the geometry of complex foliations with integrable physical systems. This thesis is divided into two parts. The first part deals with problems related to rigid body dynamics and the second part with problems on Hamiltonian monodromy. In Appendix A different perspectives are described, in particular, in Section A.3 a brief description of a potentially interesting connection between the two parts of this thesis is given.

The main problem under study in the first part is the tennis racket effect (TRE). In short, it can be described as an unexpected π-flip observed (in such a way that the faces of the head of the racket are exchanged) after a complete turn (2π-rotation) of the handle of the racket is performed [61]. Several studies about this effect have been published [5, 70, 69, 47, 74], in which different assumptions were imposed to obtain approximations that allow a better understanding of this effect.

A similar effect is the Dhzanibekov [1] effect, where the unexpected π-flip is observed after an α-rotation of the handle [14]. There exist fewer

[1]Named after the Soviet cosmonaut Vladimir Dzhanibekov, who noticed this effect in space in 1985.

scientific articles about this effect [58]; maybe because the existence of it was kept as a secret for almost ten years [71].

On the other hand, the monster flip is a skateboarding trick where the objective is to perform a complete flip of the skateboard around its intermediate axis avoiding any extra rotation (to be able to continue skating). In particular, this implies that one has to avoid the tennis racket effect. There is no scientific reference studying this trick, but it is a famous skateboard trick and many videos and explanations can be found on the internet [19, 33].

Finally, the Montgomery phase [51] is part of the geometric phases[2] in physics [44]. The Montgomery phase measures a specific rotation of a rigid body in a laboratory frame. When the angular momentum of the rigid body performs a loop in the body-fixed frame, the system rotates by some angle around the fixed direction of the angular momentum in the initial frame. This angle of rotation is the Montgomery phase [52] and it is closely related to the tennis racket effect.

In the first part of this work, we treat the phenomena mentioned before. In the first Chapter, we present an overview of the classical definitions and results that we need to develop this part. In Chapter 2, we address the problem of finding a good mathematical description of the tennis racket effect to understand its origin and, as consequence, the origin of the Dhzanibekov effect and the monster flip. We detect different regions to analyze using complex geometry, and then, perform a study in the real domain for each of these regions; obtaining results explaining the three aforementioned effects. In Chapter 3, we take into account some physical restrictions that the moments of inertia of a rigid body have to fulfill. We detect differences in the rigid body dynamics for the cases in which the moments of inertia fulfill these restrictions and when they do not. We show how to detect such constraints in the TRE and the Montgomery phase. We take advantage of the geometrical structure introduced for this problem to make a global analysis of the tennis racket effect, to study some limit cases, and to obtain results about the existence of the perfect TRE and the existence of the Dhzanibekov effect with a given value of α.

In the second part, the main problem under study is Hamiltonian monodromy, concept introduced by Duistermaat [28] in 1980, which has been extensively studied [13, 22, 76, 8, 67, 30, 53, 46, 66, 31, 49] since then, from many different perspectives.

We now give a brief presentation of the origin of this concept. In 1970, Smale [64] proposed a program to understand mechanical systems in $\mathbb{R}^4$ with

[2] As well as the Berry phase in quantum mechanics, for instance.

symmetries. This program can be described as follows. Let us consider a conservative mechanical system in $\mathbb{R}^4$, with a symmetry described by an action of a group of diffeomorphisms that leave the Hamiltonian invariant. This symmetry defines a first integral, J, and let H be the total energy of the system. Then the energy-momentum map is the mapping from the phase space $\mathbb{R}^4$ to $\mathbb{R}^2$ given by (H, J). The first step of the program is to find the critical values of the energy-momentum map, the second step is to describe the topology of all the regular fibers. The third one is to find the dynamics on each regular fiber and finally, the fourth step is to describe how these regular fibers glue together to understand the global dynamics.

The first step can be done nowadays, in most cases, with the help of computers. The second and third steps were answered by Liouville and then completed by Mineur and Arnold, resulting in their famous Theorem [1] that ensures, under certain hypotheses, the existence of a local change of coordinates that transforms the dynamics into a linear flow over invariant tori. This change of coordinates is called action-angle coordinates. The fourth step of this program was done in a paper [28] by Duistermaat in 1980. In this paper, he introduced the concept of Hamiltonian monodromy, as part of the answer to the fourth and last step of the program. Hamiltonian monodromy is the simplest obstruction to the existence of global action-angle coordinates, and, thus, to a trivial gluing giving the global dynamics of the system.

Nevertheless, for a given system to know whether or not it has trivial Hamiltonian monodromy is not an easy task. There is a large area of study on this subject for different mechanical systems, either in the study of explicit systems or in giving conditions to know when this gluing is non-trivial.

In the second part of this thesis, we address the problem of giving conditions on mechanical systems to ensure that the Hamiltonian monodromy of the system is nontrivial using spectral Lax pairs. The advantage of Lax pairs is that they provide the system with an algebraic structure that is very useful for its study. This part is organized into five chapters. In Chapter 4, we introduce all the concepts mentioned before. In Chapter 5, we state and prove auxiliary results used in the proofs of the main results. In Chapter 6, we properly state and prove that for a mechanical system in $\mathbb{R}^4$ one can introduce a Riemann surface, using spectral Lax pairs, such that the computation of the Hamiltonian monodromy of the system boils down to the computation of a residue at infinity of a meromorphic 1-form defined over this Riemann surface. In Chapter 7, we give a solution for the problem of finding a spectral Lax pair for a given system with a focus-focus singularity. Finally, in Chapter 8, we present two relevant examples in physics to show

how the obtained results simplify some calculations.

The different constructions and ideas of the first and the second part of this work, follow the general idea of using tools of complex foliations to obtain a geometric structure of the problem in hand that leads to the understanding of the corresponding physical system. This is the framework of the present thesis.

Contents

Part I

Rigid body dynamics

Chapter 1

Preliminaries

In this chapter, we introduce all the classical concepts and techniques about rigid body dynamics that we need to derive the results of the following chapters. We stress that the content of this chapter is well-known, we include it here for completeness.

1.1 Quick overview of ODE

Let us recall the definition of an ordinary differential equation to then give the geometric interpretation of it. Let $F\colon \mathbb{R}^n \to \mathbb{R}^n$ be a smooth function, the *ordinary differential equation given by* F is the equation

$$\frac{d}{dt}(x(t)) = F(x(t)). \tag{1.1}$$

If we add the condition $x(0) = x_0$, then we have an *initial value problem.*

A *solution* of the differential equation (1.1) is a smooth function $\varphi\colon \mathbb{R} \to \mathbb{R}^n$ such that

$$\frac{d}{dt}(\varphi(t)) = F(\varphi(t)).$$

If the function φ fulfills $\varphi(0) = x_0$, then φ is a solution to the initial value problem.

We describe the geometric meaning of these concepts. A differential equation can be interpreted as follows: for each point, $p_0 \in \mathbb{R}^n$ we have the vector given by $F(p_0)$, and this vector represents a tangent vector at the point p_0. In this way, finding solutions of the differential equation (1.1) is the same as finding curves such that at each point of the curve, the vector given by F represents the velocity vector of the curve (see Figure 1.1).

We obtain important information from these curves, called *integral curves.* For this reason, the following concept is introduced.

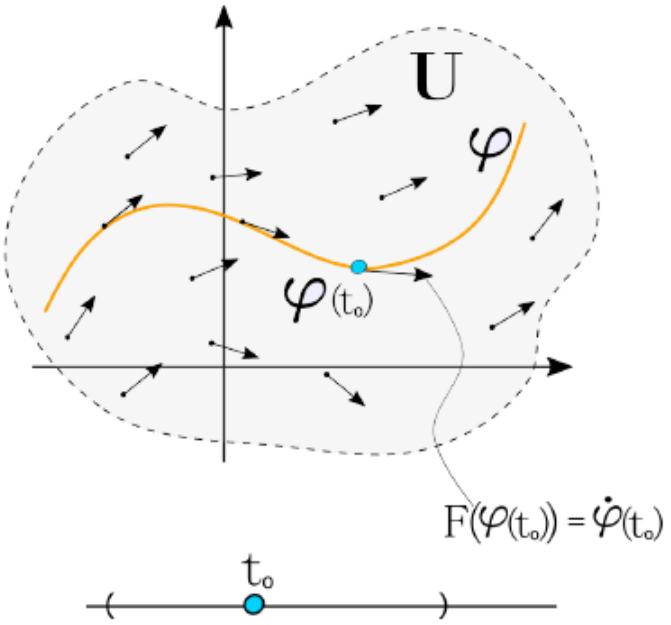

Figure 1.1: Geometric interpretation of an ODE. U is an open subset of $\mathbb{R}^2$ where the differential equation $\frac{d}{dt}(x(t)) = F(x(t))$ is defined. Thanks to G. Martinez-Salgado for the figure.

Consider the ordinary differential equation (1.1). A first integral of this equation is a non-constant smooth function $H\colon \mathbb{R}^n \to \mathbb{R}$, such that for every solution φ of the differential equation (1.1), $H(\varphi)$ is constant (with respect to time). In other words

$$\frac{d}{dt}H(\varphi(t)) = 0.$$

Geometrically, this equation means that the solutions of the differential equation are contained in the level sets of the function H. Notice that, in $\mathbb{R}^2$ this property implies that the integral curves are the level curves of the function H (see Figure 1.2).

On the other hand, if we have a differential equation on $\mathbb{R}^n$, with $n > 2$, then $H = c$ is a hypersurface. In this case, the integral curves are contained in the hypersurface, but one does not get the exact shape of the integral curves. Let us exemplify this with a differential equation that will be useful later since Euler's equations are a particular case of this system.

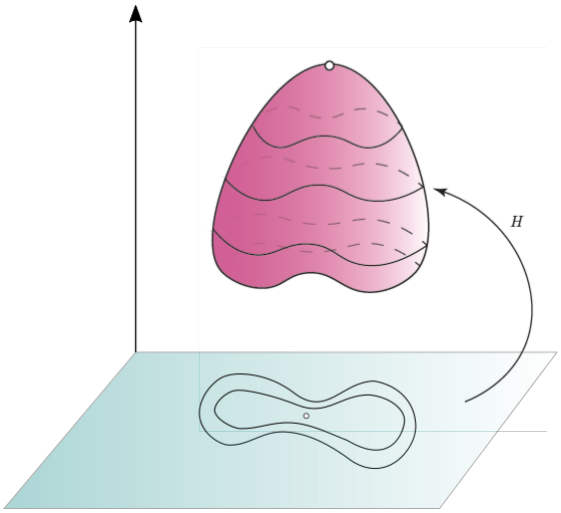

Figure 1.2: Graph and level curves of H.

1. Consider the ordinary differential equation:

$$\begin{aligned}\frac{d}{dt}M_1 &= c_1 M_2 M_3\\ \frac{d}{dt}M_2 &= c_2 M_1 M_3\\ \frac{d}{dt}M_3 &= c_3 M_1 M_2,\end{aligned}$$

where $c_1 + c_2 + c_3 = 0$, and the function $H(M_1, M_2, M_3) = M_1^2 + M_2^2 + M_3^2$. Then, if we consider a solution of the differential equation $\varphi(t) = (M_1(t), M_2(t), M_3(t))$, we obtain

$$\begin{aligned}\frac{d}{dt}H(\varphi(t)) =& \frac{\partial H}{\partial M_1}(\varphi(t))\dot{M}_1(t) + \frac{\partial H}{\partial M_2}(\varphi(t))\dot{M}_2(t) + \frac{\partial H}{\partial M_3}(\varphi(t))\dot{M}_3(t)\\ =& 2M_1(t)(c_1 M_2(t)M_3(t)) + 2M_2(t)(c_2 M_1(t)M_3(t))\\ &+ 2M_3(t)(c_3 M_1(t)M_2(t))\\ =& (c_1 + c_2 + c_3)2M_1(t)M_2(t)M_3(t)\\ =& 0.\end{aligned}$$

We conclude that the function H is a first integral for the system given by this differential equation. Now, we analyze the equation $H(M_1, M_2, M_3) = c$, for different values of the constant c.

Again, we fix a value $c > 0$, the expression $H = c$ is the same as $M_1^2 + M_2^2 + M_3^2 = c$. Hence, we conclude that the level set

$$\{(M_1, M_2, M_3) \in \mathbb{R}^3 \mid H(M_1, M_2, M_3) = c\}$$

is a sphere of radius $\sqrt{c}$. If $c < 0$, then the level set is empty, and if $c = 0$ the level set only contains the origin. Notice that for $c > 0$, we have concentric spheres.

Thus, in $\mathbb{R}^3$, it is not enough to find a first integral to know the integral curves of the differential equation. In this example, the solution curves are contained in a sphere, but we have not found them. For this reason, it is a usual technique to try to find another first integral (or more if the dimension is higher).

1.2 The rigid body

A rigid body is an object in classical mechanics that does not deform in time. Hence, its mass distribution and its shape are fixed. The mathematical definition of the *center of mass* G is given by the integral

$$\overrightarrow{OG} = \frac{1}{M} \iiint_{\mathcal{S}} \rho(Q)\vec{r}(Q)d^3Q,$$

where $\mathcal{S}$ is the rigid body, M is the total mass, ρ is the density function (which indicates how the mass is distributed in the body), r is the position vector of each point of the body. From this equation, one can see that the center of mass can be interpreted as a point on the rigid body such that the mass of the object is well distributed around it.

When we study a rigid body, we need two coordinate frames; the laboratory frame which is fixed, and one frame attached to the rigid body that moves with the body. We analyze free rotations of a rigid body. Since we do not consider translations, the center of mass is fixed in the laboratory frame (standard assumption to remove the global translation of the rigid body). Thus, in this case, the origin of both frames is chosen to be the center of mass of the rigid body.

We now study an illustrative example to introduce the concept of angular velocity.

- Let us consider a point particle in $\mathbb{R}^3$ rotating along a circle around the z-axis in a positive direction (see Figure 1.3) with constant angular

speed ω. We know that the angular velocity is defined as the vector which has the same direction as the axis of rotation, norm equal to the angular speed, and the orientation given by the right-hand rule. In this example, the angular velocity is the vector $(0, 0, \omega)$.

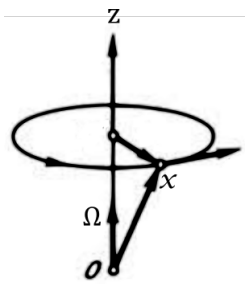

Figure 1.3: Point particle rotating around the vertical axis.

We denote as $x(t)$ the vector that describes the position of the particle, and R is the radius of the circle. Then

$$x(t) = (R\cos(\omega t), R\sin(\omega t), \|x\|\cos(\theta)),$$

where θ is the angle between the z-axis and the vector x. The derivative is

$$\dot{x}(t) = (-\omega R\sin(\omega t), \omega R\cos(\omega t), 0).$$

Since $\|x\|$ and θ do not depend on time. Now, we compute the product $\mathbf{\Omega} \times x(t)$:

$$\mathbf{\Omega} \times x(t) = (-\omega R\sin(\omega t), \omega R\cos(\omega t), 0).$$

Concluding that $\dot{x}(t) = \mathbf{\Omega} \times x(t)$. Observe that the angular speed is equal to $\|\mathbf{\Omega}\|$. The computations here are made for a vector along the z-axis, but it is possible to do the same for any vector and the same result is obtained.

Similarly, we consider a point on the rigid body and the vector going from the center of mass to this point. Then, if the rigid body rotates around a fixed axis, the movement of this vector is described by the equation obtained in the previous example, *i.e.*, if we attach a vector x to the center of mass of the rigid body, and the rigid body is rotating around a fixed axis with angular speed $\omega = \|\mathbf{\Omega}\|$, then the time evolution of x is

$$\dot{x}(t) = \mathbf{\Omega} \times x(t).$$

Consider that the observer is on the surface of the rigid body, the rigid body is rotating, and the observer follows the evolution of a vector X belonging to the laboratory frame then, the observer notices the same movement described before for the vector x, but in the opposite direction. Hence, one obtains

$$\dot{X}(t) = -\mathbf{\Omega} \times X(t) = X(t) \times \mathbf{\Omega}.$$

When the rigid body is rotating in an arbitrary way (not around a fixed axis), in a short time dt, the rotation is very similar to the aforementioned rotation (around a fixed axis with constant speed), so one expects a similar time evolution.

The equations describing this time evolution are [7]:

$$\dot{x}(t) = \mathbf{\Omega}(t) \times x(t) \tag{1.2}$$

$$\dot{X}(t) = X(t) \times \mathbf{\Omega}(t). \tag{1.3}$$

A formal derivation of these two equations can be found in [3]. In this later text a formal result is given assuring that for every time t, there exists a vector $\mathbf{\Omega}(t)$ which fulfills the equation $\dot{x}(t) = \mathbf{\Omega}(t) \times x(t)$. In this general case, the function $\mathbf{\Omega}(t)$ is defined as the angular velocity of the rigid body. Then, it can also be proved that for every time t the vector $\mathbf{\Omega}(t)$ fulfills the equation $\dot{X}(t) = X(t) \times \mathbf{\Omega}(t)$, where X is a vector of the laboratory frame.

The angular momentum is formally defined as

$$\mathbf{J}(t) = \int\int_{\mathcal{S}}\int \rho(Q) r(Q) \times \dot{r}(Q) d^3Q. \tag{1.4}$$

If the rigid body is rotating freely, *i.e.*, without external forces, then the angular momentum $\mathbf{J}$ does not depend on time. This fact is known as the angular momentum Theorem and it is a consequence of Newton's laws[34]. For this reason, we can consider the vector $\mathbf{J}$ as a vector in the laboratory frame. The usual convention is to consider it aligned with the Z-axis of the laboratory.

Finally, using Eq. (1.3), one gets

$$\dot{\mathbf{J}}(t) = \mathbf{J}(t) \times \mathbf{\Omega}(t). \tag{1.5}$$

The definition of *moment of inertia* with respect to a rotational axis E can be interpreted as a quantity that measures the resistance that the rigid body puts to turn around a rotational axis E (or how dispersed the mass of the body is with respect to the E-axis), and is given by

$$I_E = \int\int_{\mathcal{S}}\int \rho(Q) r_E^2(Q) d^3Q,$$

where r_E is the distance of each point of the rigid body $\mathcal{S}$ to the rotational axis E.

Given the fact that the cross product by a fixed vector is a linear operator in a 3-dimensional Euclidean space, one can prove that there is a linear operator relating the angular momentum to the angular velocity using equations (1.4) and (1.5). This fact can be stated as follows.

Theorem 1.1. The angular momentum $\mathbf{J}$ of a rigid body with one stationary point G depends linearly on the angular velocity $\mathbf{\Omega}$, *i.e.*, there exists a constant linear operator I such that $I\mathbf{\Omega} = \mathbf{J}$. Moreover, I is a symmetric operator and the total energy of the body can be written as the quadratic form $\frac{1}{2}I\mathbf{\Omega} \cdot \mathbf{\Omega}$.

A coordinate system in which I is diagonal is called a principal axis system and the eigenvalues of I are called moments of inertia of the body. A usual convention is to choose the frame attached to the body as the coordinate system made up of the three principal rotational axes whose origin is at the center of mass of the body.

Thus, in this body fixed frame, the angular momentum vector $\mathbf{J}$ is related to the angular velocity $\mathbf{\Omega}$ through the relation

$$\mathbf{J} = I\mathbf{\Omega},$$

with I diagonal, since the three principal rotational axes are given by the directions of the three eigenvectors of this matrix. Thus, one has the following relations

$$\begin{aligned}
\Omega_x &= \frac{J_x}{I_x} \\
\Omega_y &= \frac{J_y}{I_y} \\
\Omega_z &= \frac{J_z}{I_z},
\end{aligned}$$

where, (x, y, z) is the frame attached to the rigid body (made up of the three principal rotational axes) and I_x, I_y, I_z are the corresponding moments of inertia (the three corresponding eigenvalues). Using Eq. (1.5), we obtain

$$\begin{aligned}
\dot{J}_x &= \left(\frac{1}{I_z} - \frac{1}{I_y}\right) J_y J_z \\
\dot{J}_y &= \left(\frac{1}{I_x} - \frac{1}{I_z}\right) J_x J_z \\
\dot{J}_z &= \left(\frac{1}{I_y} - \frac{1}{I_x}\right) J_x J_y,
\end{aligned}$$

These equations are the *Euler's equations* describing the dynamics of free rotations of a rigid body. There exist different approaches to introduce these equations of motion see [7] or [1, 65] for a Lie group point of view. Notice that, since we consider only rotations, we neglect gravity. This system is also called Euler-Poinsot system [45]. Let us now analyze these equations.

First notice that

$$\left(\frac{1}{I_z}-\frac{1}{I_y}\right)+\left(\frac{1}{I_x}-\frac{1}{I_z}\right)+\left(\frac{1}{I_y}-\frac{1}{I_x}\right)=0.$$

Thus, Euler's equations are a particular case of the differential equations considered in Section 1, where we proved that the function $J^2(J_x,J_y,J_z)=J_x^2+J_y^2+J_z^2$ is a first integral of the system. In this case, it corresponds to the square of the norm of the angular momentum. We also showed that the level curves of the function J^2 are spheres of radii J for non-negative values of J.

As explained in Section 1, to find the integral curves of the differential equation it is not sufficient to have only one first integral. Nevertheless, for this system, the total energy is conserved and is given in Theorem 1.1 as $\frac{1}{2}I\boldsymbol{\Omega}\cdot\boldsymbol{\Omega}$, obtaining

$$E(J_x,J_y,J_z)=\frac{J_x^2}{2I_x}+\frac{J_y^2}{2I_y}+\frac{J_z^2}{2I_z}.$$

We conclude that this system has two first integrals, which is enough to obtain the integral curves. In the following paragraphs, we explain how to obtain these curves.

We assume the relation $I_z<I_y<I_x$, which means that we analyze an asymmetric rigid body. Then, for non-positive values of the energy the level sets are empty, and for positive values of the energy the level sets are ellipsoids with radii: $\sqrt{2EI_x}$, $\sqrt{2EI_y}$, $\sqrt{2EI_z}$. If we fix both, the value of E and J^2, we obtain curves that have to be integral curves of our differential equation.

Now, we consider a fixed value of J^2 and we change the value of E to analyze all the possible curves that one can obtain. This means that we fix a sphere and analyze the different curves that we can obtain when the ellipsoid given by E is changing.

For a fixed sphere, the integral curves are represented in Figure 1.5, they correspond to the intersections between the fixed sphere given by J^2 and the different level sets of E. On each sphere, we have six fixed points, four of them are stable and two are unstable. The trajectory connecting two unstable points is called *separatrix* and its equation is given by $\frac{2I_yE}{J^2}=1$.

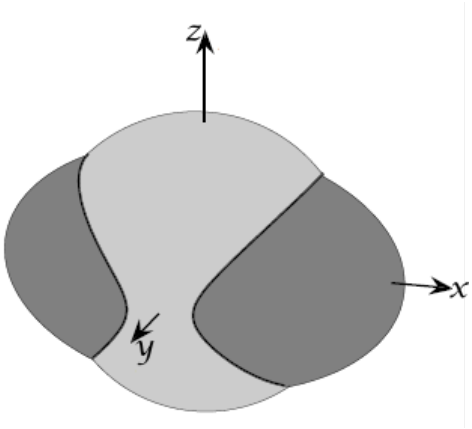

Figure 1.4: Intersection between a level set of J^2 (light grey sphere) and a level set of E (grey ellipsoid) [68].

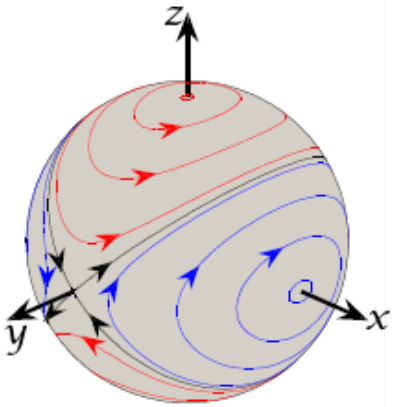

Figure 1.5: Solutions obtained on a fixed sphere [68]. We have 4 stable fixed points and 2 unstable points that are connected through the black trajectory called separatrix. The red trajectories are called oscillating trajectories and the blue ones are called rotating trajectories.

Thus, we define the distances of a given integral curve to the separatrix as

$$c = \frac{2I_y E}{J^2} - 1. \tag{1.6}$$

1.3 Euler angles

Since we are interested in free rotations of rigid bodies, the natural coordinates are given by rotation angles.

For this reason, we introduce a new coordinate system which is known as the *Euler angles*. This new coordinate system describes the rotation of the laboratory frame (X, Y, Z) with respect to the frame attached to the body (x, y, z).

This coordinate system is not unique. We follow the ZYZ convention in which, to go from the laboratory frame to the body frame, the following three successive rotations are considered:

- The first one is a rotation of an angle ϕ around the Z axis, this movement gives us a new position of the vectors X and Y, let us denote these new positions as X' and Y'. (See the first panel in Figure 1.6)

- The second one is a rotation of an angle θ around the new axis Y'. Then, the position of the axes X' and Z have changed to the new positions X'', Z''. (See the second panel in Figure 1.6)

- The last one is a rotation of an angle ψ around the new axis Z''.

After these successive rotations, we have arrived at the frame attached to the rigid body (x, y, z). We denote by $\mathcal{N}$ the *line of nodes* which is located where the vector Y' is located (it is also the line of intersection of the planes (X, Y) and (x, y)). (See third drawing on Figure 1.6)

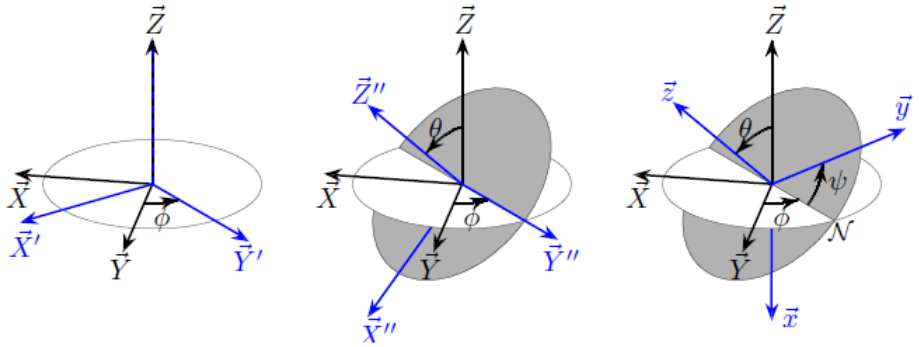

Figure 1.6: Construction of the Euler angles [68].

The new coordinate system is given by (ϕ, θ, ψ) and is known as *the Euler angles*. Let us find the equations of motion in this new coordinate system.

As explained before, for each angle, its derivative (the angular velocity) is a vector in the direction of the rotation axis, and the direction is given by the right-hand rule. Thus, one has that $\dot{\boldsymbol{\phi}}$ is along the line given by the Z-axis. The angular velocity $\dot{\boldsymbol{\theta}}$ is along the line of nodes and $\dot{\boldsymbol{\psi}}$ is along the line given by the axis z; and its coordinates in the frame (x, y, z) are given by

$$\begin{array}{lll} \dot{\phi}_x = -\dot{\phi}\sin(\theta)\cos(\psi) & \dot{\theta}_x = \dot{\theta}\sin(\psi) & \dot{\psi}_x = 0 \\ \dot{\phi}_y = \dot{\phi}\sin(\theta)\sin(\psi) & \dot{\theta}_y = \dot{\theta}\cos(\psi) & \dot{\psi}_y = 0 \\ \dot{\phi}_z = \dot{\phi}\cos(\theta) & \dot{\theta}_z = 0 & \dot{\psi}_z = \dot{\psi}, \end{array}$$

where $\dot{\phi}$, $\dot{\theta}$, and $\dot{\psi}$ represent the angular speed.

These expressions are obtained by considering the projections of each vector on the coordinate system (x, y, z). As an example, we now analyze $\dot{\phi}_x$. All the other expressions are obtained in the same way, but the procedure is easier.

The goal is to find the x-coordinate of the vector Z. First, we note that the vector Z and the line of nodes are orthogonal since the line of nodes is located where the vector Y' was located (see Figure 1.6). For this reason, when we project the vector Z onto the plane (x, y), this projection is on a line (on this plane) which is orthogonal to the line of nodes. Moreover, the x-coordinate is negative for the configuration of the two coordinate systems (x, y, z) and (X, Y, Z) (*i.e.* for our convention ZYZ). Finally, when we project the vector Z onto the plane (x, y), the length of this projection is $\dot{\phi}\sin(\theta)$. With this information, it is easy to find the expression of $\dot{\phi}_x$ given before.

Thus, the components of the angular velocity $\boldsymbol{\Omega}$ of the rigid body are given by

$$\begin{aligned} \Omega_x &= \dot{\phi}_x + \dot{\theta}_x + \dot{\psi}_x \\ \Omega_y &= \dot{\phi}_y + \dot{\theta}_y + \dot{\psi}_y \\ \Omega_z &= \dot{\phi}_z + \dot{\theta}_z + \dot{\psi}_z \end{aligned}$$

As said before, the vector $\mathbf{J}$ is aligned with the vector Z of the laboratory frame. Thus, we have an expression for $\mathbf{J}$ similar to the one we obtained for the angular velocity associated with ϕ, *i.e.*

$$\mathbf{J} = (-J\sin(\theta)\cos(\psi), J\sin(\theta)\sin(\psi), J\cos(\theta)).$$

On the other hand, using the relation between $\mathbf{J}$ and $\mathbf{\Omega}$ we have

$$\mathbf{J} = (I_x\Omega_x, I_y\Omega_y, I_z\Omega_z).$$

By equating coordinate to coordinate of these two expressions of $\mathbf{J}$, one obtains a system of 3 linear equations that can be solved for $\dot{\phi}$, $\dot{\theta}$ and $\dot{\psi}$, giving

$$\begin{aligned}
\dot{\phi} &= J\left(\frac{1}{I_x}\cos^2(\psi) + \frac{1}{I_y}\sin^2(\psi)\right) \\
\dot{\theta} &= J\left(\frac{1}{I_y} - \frac{1}{I_x}\right)\sin(\theta)\cos(\psi)\sin(\psi) \\
\dot{\psi} &= J\cos(\theta)\left(\frac{1}{I_z} - \frac{1}{I_x}\cos^2(\psi) - \frac{1}{I_y}\sin^2(\psi)\right).
\end{aligned} \tag{1.7}$$

These are the Euler equations of the rigid body in terms of Euler angles.

1.4 Physical constraints on the moments of inertia

Recall that, in the body-fixed frame, the angular momentum of the body $\mathbf{J}$ is connected to the angular velocity $\mathbf{\Omega}$ through the relation $\mathbf{J} = I\mathbf{\Omega}$, where I is a 3×3 symmetric matrix, called the inertia matrix. Its eigenvalues are the inertia moments denoted I_x, I_y, and I_z and correspond to the three axes of the body-fixed frame. For any rigid body there exist the following physical restrictions on the values of the moments of inertia

$$I_i + I_j \geq I_k \tag{1.8}$$

with $\{i, j, k\} = \{x, y, z\}$ and not equal. This constraint can be established from the definition of the moments of inertia in the principal axis frame

$$I_i = \int_S \rho(\mathbf{r})\left(x_j^2 + x_k^2\right) d\mathbf{r}, \tag{1.9}$$

where ρ is the mass density, V the volume of the body and x_j the coordinates of the position vector $\mathbf{r}$, $(x_1, x_2, x_3) \equiv (x, y, z)$. We deduce that

$$I_i = \int \rho(\mathbf{r})\left(x_j^2 + x_k^2\right) d\mathbf{r} \leq \int \rho(\mathbf{r})\left(2x_i^2 + x_j^2 + x_k^2\right) d\mathbf{r} = I_j + I_k. \tag{1.10}$$

In the case of an asymmetric rigid body such that

$$I_z < I_y < I_x, \tag{1.11}$$

the only constraint to satisfy is

$$I_y + I_z \geq I_x. \tag{1.12}$$

Definition 1.2. Let I_x, I_y, I_z be the moments of inertia of an asymmetric rigid body such that $I_z < I_y < I_x$. A rigid body is said to be *physical* if the values of the moments of inertia fulfill Eq. (1.12).

We introduce the parameters a and b, describing the asymmetry of the body, defined as

$$a = \frac{I_y}{I_z} - 1 \ , \qquad b = 1 - \frac{I_y}{I_x}. \tag{1.13}$$

The parameter a measures how different the moments of inertia I_y and I_z are (measuring the asymmetry of the object in these directions) and b does the same with I_x and I_y. Note that, by definition, $a > 0$ and $0 < b < 1$.

The physical constraint (1.12) can be easily written by introducing a constant $\mathcal{I} = \mathcal{I}(a, b)$, which we call the *geometric constant*. For further use, we also introduce a *second geometric constant* $\mathcal{J} = \mathcal{J}(a, b)$. These constants are defined by the following formulas

$$\mathcal{I} = \frac{1-b}{\sqrt{b\,(a+b)}}, \quad \mathcal{J} = \frac{a+1}{\sqrt{a\,(a+b)}} - 1. \tag{1.14}$$

Proposition 1.3. Let I_x, I_y, I_z be the moments of inertia of an asymmetric rigid body such that $I_z < I_y < I_x$. The moments of inertia I_x, I_y, I_z describe a physical rigid body if and only if the geometric constant $\mathcal{I}$ satisfies the inequality $\mathcal{I} \geq 1$.

Proof. From Eq. (1.13), we get

$$I_y = (1-b)\, I_x \ , \qquad I_z = \left(\frac{1-b}{1+a}\right) I_x. \tag{1.15}$$

Since $I_x \neq 0$, we have $I_y + I_z \geq I_x$, if and only if

$$1 - b + \frac{1-b}{1+a} \geq 1. \tag{1.16}$$

Using $0 < 1 + a$, Eq. (1.16) is verified if and only if

$$(1-b)\,(1+a) + 1 - b \geq 1 + a, \tag{1.17}$$

which is equivalent to $ab + b^2 \leq 1 - 2b + b^2$ and finally to $\mathcal{I} \geq 1$. □

The set of points of coordinates (a, b) that fulfill the constraint $\mathcal{I} \geq 1$ is represented in Fig. 1.7.

This physical constraint will be a key point in Chapter 3.

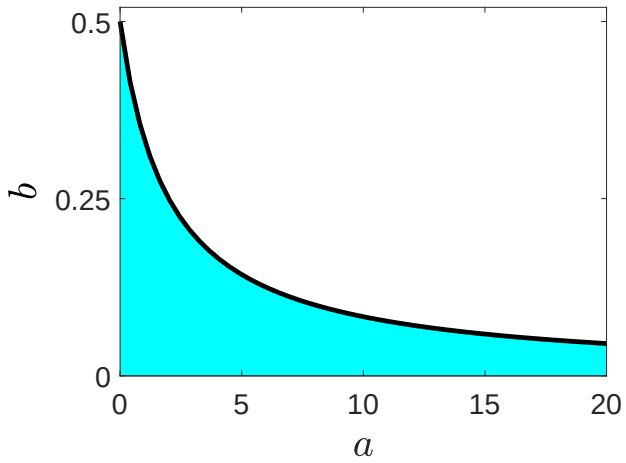

Figure 1.7: Set of points (a, b) (blue area) such that $\mathcal{I} = \frac{1-b}{\sqrt{b(a+b)}} \geq 1$. The solid black line represents the points for which $\mathcal{I} = 1$.

Chapter 2

Geometric origin of the tennis racket effect

Rigid body dynamics is a classical topic treated in several books [34, 41, 3, 22]. Nevertheless, the tennis racket effect is not widely studied. There exist few texts about this geometric effect [5, 22], where different approaches are used to study particular cases. The goal of this work is then to give a complete mathematical description of this effect obtaining results about the existence, the origin, and the mathematical structure of this problem. We introduce a suitable description of the problem that allows us to treat also the Dzhanibekov effect [58] and the monster flip, for which there is no scientific reference. The content of this chapter has been published in the journal Physical Review Letters [48].

Before describing the tennis racket effect, let us point out that our interest in it was sparked by the cover of the book by Cushman and Bates [22] where there is a nice representation of this effect. Then, results published in 2017 in Scientific Report [69] linked the tennis racket effect to the control of spin 1/2-particles employing electromagnetic fields; turning out to be an interesting effect connecting classical and quantum mechanics.

The tennis racket effect can be described as follows: Consider an experiment that every tennis player has already made. The tennis racket is held by the handle and thrown in the air so that the handle makes a full turn before catching it. Assume that the two faces of the head can be distinguished. It is then observed, once the racket is caught, that the two faces have been exchanged. The racket did not perform a simple rotation around its axis, but also an extra half-turn. This twist is called the tennis racket effect (TRE). An intuitive understanding of TRE is given in [71]. It is also known as Dzhanibekov's effect (DE), named after the Russian cosmonaut who made a similar experiment in 1985 with a wing nut in zero

gravity [54, 14]. The wing nut spins rapidly around its central axis and flips suddenly after many rotations around a perpendicular axis [14]. The Monster Flip (MF) is a freestyle skateboard trick. It consists of jumping with the skateboard and making it turn around its transverse axis with the wheels falling back to the ground. This trick is very difficult to execute since TRE predicts precisely the opposite, turning about this axis should produce a π- flip, and the wheels should end up in the air. The video [19] shows that this trick can be made with success after many attempts.

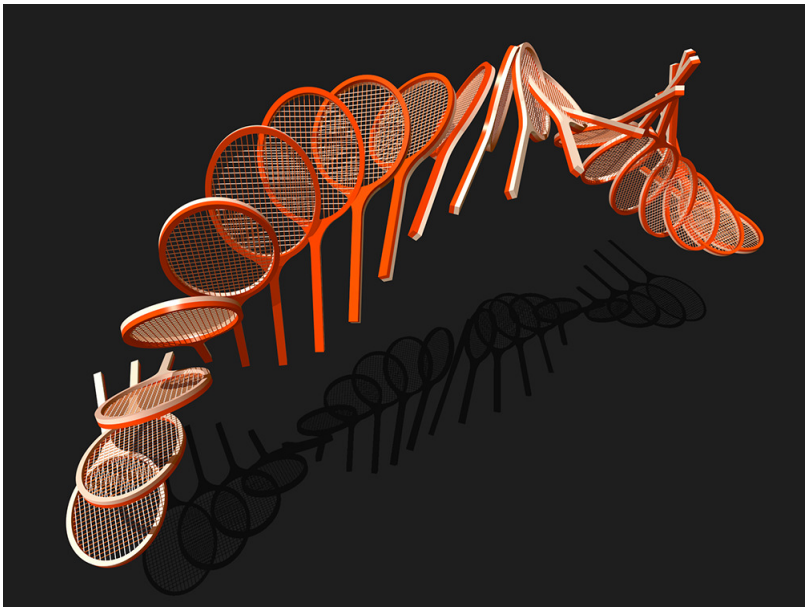

Figure 2.1: Representation of the tennis racket effect [48]. After one complete turn of the handle of the racket an extra flip is observed, so the faces of the head of the racket are exchanged. Thanks to S. J. Glaser for providing this figure.

This chapter is organized as follows: In Section 2.1, we introduce the mathematical structure of the problem that allows to study it. In Section 2.2, we present the results concerning the TRE. In Section 2.3, we obtain similar results for the DE. Finally, in Section 2.4, we use approximations to obtain results on the MF.

2.1 Notations and conventions

To link the introductory chapter and the aforementioned effects, we describe explicitly the frame attached to the following rigid bodies: a tennis racket, a skateboard, and a wing-nut. We assume the relation $I_z < I_y < I_x$. This inequality implies:

1. For the tennis racket, the axis with the smallest moment of inertia is the axis that goes through the handle of the racket, so this axis has to be the z-axis, and the axis with the largest moment of inertia is the axis that is perpendicular to the plane formed by the head of the racket (see Figure 2.2), thus this corresponds to the x-axis.

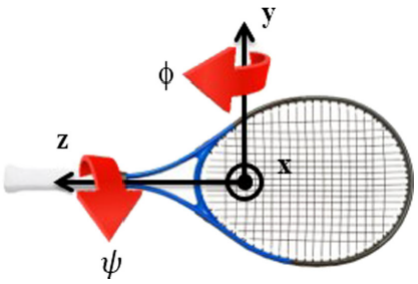

Figure 2.2: Principal rotational axes for the tennis racket [68].

2. For the skateboard we have a similar configuration to the one for the tennis racket (See Figure 2.3).

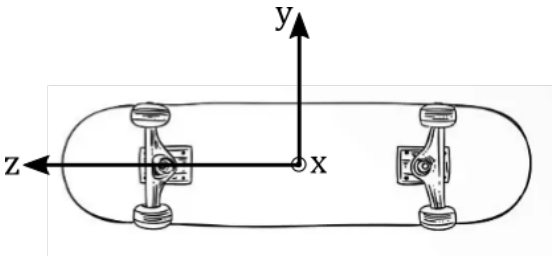

Figure 2.3: Principal rotational axes for the skateboard.

3. Finally, for the wing-nut we assume that the "wings" are larger than the height and we obtain the configuration shown in Figure 2.4.

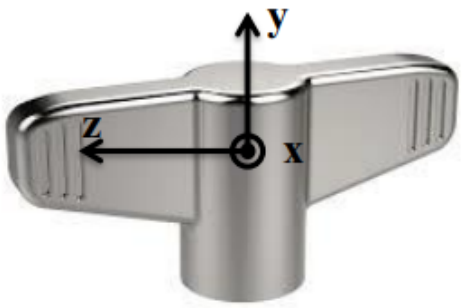

Figure 2.4: Principal rotational axes for the wing-nut [68].

We recall that $\mathbf{J} = (I_x\Omega_x, I_y\Omega_y, I_z\Omega_z)$. If the object turns around a fixed axis (x, y or z-axis), then the angular velocity Ω is aligned with this axis, and therefore $\mathbf{J}$ is too. For the tennis racket, one wants to perform a pure rotation around the y-axis. Hence, when the experiment starts, $\mathbf{J}$ is almost aligned with the y-axis, in other words, we consider a trajectory with an initial condition near one of the unstable points (see 1.5). This means that we need to consider the initial conditions: $\theta_0 \approx \frac{\pi}{2}$, $\psi_0 \approx -\frac{\pi}{2}$.

Moreover, if we consider $\theta_0 \approx \frac{\pi}{2}$, $\psi_0 \approx -\frac{\pi}{2}$, $\phi_0 = 0$ with final conditions $\theta_f \approx \theta_0 \approx \frac{\pi}{2}$, $\psi_f \approx \frac{\pi}{2}$, $\phi_f = 2\pi$, following the construction[1] of Euler angles described in Section 1.3, one gets that the Euler angles ϕ and ψ are the angles that we want to study, *i.e.*, the angles shown in Fig. 2.2.

Thus, the tennis racket effect can be defined in terms of Euler angles as $\Delta\psi \approx \pi$ when $\Delta\phi = 2\pi$. The monster flip is $\Delta\phi = 2\pi$ when $\Delta\psi \approx 0$; that is, no flip is observed. Finally, the Dzhanibekov effect is very similar to the TRE, but at the beginning, the movement is guided (by a screw). For this reason, we need a large number of flips to observe a half-flip in the other direction. Thus, this problem can be described as $\Delta\psi \approx \pi$ when $\Delta\phi = k2\pi$, with $k \in \mathbb{R}$.

These are geometric effects in the sense that we are not interested in the time parametrization of the solutions, we are just interested in the variation of the angle ψ for a given variation of the angle ϕ, or vice-versa.

Thus, to study the TRE, we can analyze the evolution of ψ with respect to ϕ. Using Euler equations (1.7) one gets

$$\frac{d\psi}{d\phi} = \frac{(a + b\cos^2\psi)\cos\theta}{1 - b\cos^2\psi}. \tag{2.1}$$

[1]Following this construction one notices that these initial and final configurations correspond to the TRE: when the handle performs a complete flip, we observe the other face of the head of the racket.

were a and b are the asymmetry parameters introduced in Section 1.4 as

$$a = \frac{I_y}{I_z} - 1 \ , \qquad b = 1 - \frac{I_y}{I_x}.$$

Moreover, we can do this because of the unicity of solutions for differential equations and because $1 - b\cos^2\psi \neq 0$ implies that we have a good projection of the solutions curves into the coordinate ϕ.

In Section 1.2, we have introduced the distance of an integral curve to the separatrix as $c = \frac{2I_y E}{J^2} - 1$, note that c is a first integral of the system. In terms of Euler angles, we can write it as

$$c = a - \sin^2\theta(a + b\cos^2\psi).$$

Using this last equation, one gets

$$\cos\theta = \pm\sqrt{\frac{c + b\cos^2\psi}{a + b\cos^2\psi}}, \tag{2.2}$$

which leads to

$$\frac{d\psi}{d\phi} = \pm\frac{\sqrt{(a + b\cos^2\psi)(c + b\cos^2\psi)}}{1 - b\cos^2\psi}. \tag{2.3}$$

Equation (2.3) defines a two-dimensional phase portrait concerning ψ and $d\psi/d\phi$, as displayed in Fig. 2.5.

On this reduced[2] phase portrait, we have one stable fixed point and two unstable ones corresponding to stable and unstable fixed points on the momentum sphere, respectively. The separatrix, for which $c = 0$, is the trajectory connecting the two unstable points. The separatrix on this reduced space also corresponds to the separatrix on the momentum sphere (See Chapter 1).

We consider only the positive values of $\frac{d\psi}{d\phi}$ defined in Eq. (2.3). The same analysis can be done for the negative sign and a global analysis where the sign change is done in Chapter 3.

[2]Reduced in the sense that we consider the variation of the angle ψ with respect to the angle ϕ. Hence, we do not consider the parametrization of the integral curves with respect to the original time t.

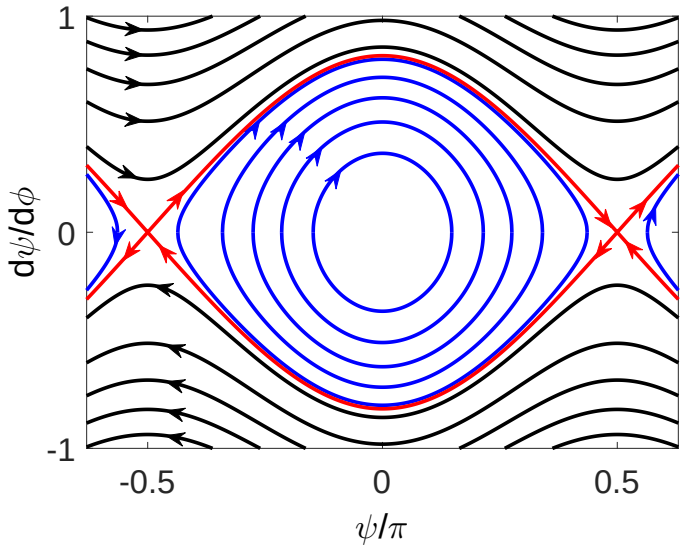

Figure 2.5: Phase portrait $(\psi, d\psi/d\phi)$ with the parameters a and b set respectively to 12 and 0.05. The black and blue lines depict respectively the rotating and oscillating trajectories of the angular momentum. The solid red line represents the separatrix.

2.2 The tennis racket effect

TRE is associated with a trajectory for which $\Delta\psi \simeq \pi$ when $\Delta\phi = 2\pi$, with $\psi_0 \simeq -\frac{\pi}{2}$ and $\psi_f \simeq \frac{\pi}{2}$ as initial and final values[3] of the angle ψ. To simplify the study of TRE, we consider a symmetric configuration, for which $\psi_0 = -\frac{\pi}{2} + \varepsilon$ and $\psi_f = \frac{\pi}{2} - \varepsilon$. A perfect TRE is thus achieved in the limit $\varepsilon \to 0$. The symmetry hypothesis is not very restrictive since ε is small.

Using Eq. (2.3), we obtain that the variation of ϕ is given by

$$\Delta\phi = \int_{-\frac{\pi}{2}+\varepsilon}^{\frac{\pi}{2}-\varepsilon} \frac{1 - b\cos^2\psi}{\sqrt{(a + b\cos^2\psi)(c + b\cos^2\psi)}} d\psi. \tag{2.4}$$

Note that, for oscillating trajectories ($c < 0$), this equation is well defined when $c + b\cos^2\psi \geq 0$. On the interval $(-\frac{\pi}{2} + \varepsilon, \frac{\pi}{2} - \varepsilon)$, this condition leads to the restriction $\sin^2\varepsilon \geq |\frac{c}{b}|$.

From the parity of the integral and the change of variables $x = \cos^2\psi$, one obtains that $\Delta\phi$ can be expressed as an incomplete elliptic integral,

[3]This is due to the expanation in the precedent Section 2.1 and because we are considering positive values of $\frac{d\psi}{d\phi}$

$\Delta\phi(\varepsilon) = \int_{\sin^2\varepsilon}^{1} \omega$, with

$$\omega = \frac{1}{b}\frac{1-bx}{\sqrt{x(x-\beta)(1-x)(x-\alpha)}}dx, \tag{2.5}$$

where $\alpha = -\frac{a}{b}$ and $\beta = -\frac{c}{b}$.

Let F be the function defined by

$$F_{a,b,c}(u) = \int_u^1 \omega = \int_\gamma \omega, \tag{2.6}$$

where γ is the integration path with $0 < u < 1$. We have $\Delta\phi_{a,b,c}(\varepsilon) = F_{a,b,c}(\sin^2\varepsilon)$.

We extend below the study to the complex domain and continue analytically all the functions to investigate the geometric origin of the TRE. The multi-valued character of $F_{a,b,c}$, as a complex function, is different for $|u| < |\beta|$ and $|u| > |\beta|$, as shown below. In the first region, the multi-valued character of $F_{a,b,c}$ is square-root-like since the integration path goes around only one branch point, while, in the second region, the multi-valued character of $F_{a,b,c}$ is logarithmic since the integration path goes around two branch points. This difference in the multi-valued character of $F_{a,b,c}$ leads to different asymptotics in the corresponding real domains.

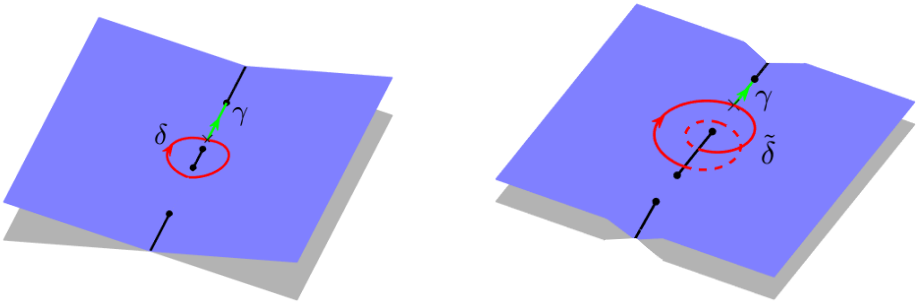

Figure 2.6: Riemann surface of the form ω with the four branch points (black dots) in $x = \alpha$, β, 0 and 1 (from bottom to top). When $c \to 0$, the two points $x = \beta$ and $x = 0$ coincide and give birth to a pole. The left and right panels represent the cases $|\beta| < |u|$ and $|u| < |\beta|$. The solid straight lines represent the branch cuts of the surface. The cycles δ and $\tilde{\delta}$ are depicted by solid red lines. The form ω is integrated along the path γ between the point u (black cross) and the ramification point $x = 1$.

Analysis of the region $|\beta| < |u| < 1$

We study in this subsection the function $F_{a,b,c}$ defined in Eq. (2.6) in both the complex and real domains.

We start with the geometric analysis in the complex space by a complexification of the problem in which $F_{a,b,c}(u)$ can be interpreted as an Abelian integral [75] over the Riemann surface of the form ω. As displayed in Fig. 2.6, this surface has two sheets with four branching points in $x = 0$, 1, β, and α. Branching cuts are introduced to define a single-valued function. In the case where $|\beta| < |u| < 1$, the limit $c \to 0$ leads to the collision of the two branching points $x = 0$ and $x = \beta$, giving rise to a pole whose integral is a logarithmic function, which reveals the geometric origin of the TRE. Notice that, for large values of a, there is no confluence of the branching point $x = \alpha$, with $x = \beta$, or 0.

In order to find precise expressions and bounds, we now study the real integrals considering a logarithmic asymptotic for the function $F_{a,b,c}$, precisely due to this complex structure. We obtain the following theorem which is the main result of this subsection. The notations and the proof can be found below.

Theorem 2.1. Let $0 < b_0 < 1$ and $0 < c_0 < 1$ be fixed and such that $0 < \frac{c_0}{b_0} < 1$. For all $b \in (b_0, 1)$, all $u_0 \in (\frac{c_0}{b_0}, 1)$ and all $c \in (-c_0, c_0)$ such that

$$0 \leq |c| < be^{-2\pi\sqrt{ab} - M(u_0, \frac{c_0}{b_0})},$$

the equation

$$\Delta\phi_{a,b,c}(\varepsilon) = 2\pi,$$

has a unique solution $\varepsilon_S(a, b, c)$, for a large enough, which verifies:

$$\arcsin\left[\sqrt{\frac{|c|}{b}}\right] < \varepsilon_S < \arcsin\left[\exp\left(-\pi\sqrt{ab} - \frac{M(u_0, \frac{c_0}{b_0})}{2}\right)\right]. \tag{2.7}$$

In particular

$$\lim_{a\to\infty} \varepsilon_S(a, b, c) = 0.$$

Notice that a large means that $I_y \gg I_z$, giving a big asymmetry on the corresponding axes. For the rest of this subsection, we analyze $F_{a,b,c}$ in the real case to obtain this result.

We express the function $F_{a,b,c}$ as

$$F_{a,b,c}(u) = \frac{1}{\sqrt{ab}}(h_1(u) + h_2(u)) - \frac{\ln(u)}{\sqrt{ab}},$$

with

$$h_1(u) = \int_u^1 \left(\frac{1}{\sqrt{x(x-\beta)}} - \frac{1}{x} \right) \frac{1-bx}{\sqrt{(1-x)(1-\frac{x}{\alpha})}} dx,$$

and

$$h_2(u) = \int_u^1 \frac{dx}{x} \left[\frac{1-bx}{\sqrt{(1-x)(1-x/\alpha)}} - 1 \right].$$

We now show that, under certain conditions on the parameters, the functions $h_1(u)$ and $h_2(u)$ are bounded.

Lemma 2.2. Let $u_0 \in \mathbb{R}$ be such that $0 < |\beta| < u_0 < 1$. For every $u \in (|\beta|, u_0)$, we have the following bound for the function h_1

$$|h_1(u)| < \frac{2\ln(1+\sqrt{2})}{\sqrt{1-u_0}} + 2M_1\sqrt{1-u_0}, \tag{2.8}$$

where $M_1 = M_1(u_0, |\beta|)$ is given by

$$M_1 = \max\left\{ \frac{1}{\sqrt{u_0(u_0-|\beta|)}} - 1, \frac{1}{u_0} - \frac{1}{\sqrt{1+|\beta|}} \right\}. \tag{2.9}$$

Proof. We have

$$|h_1(u)| \leq \int_u^1 \left| \left(\frac{1}{\sqrt{x(x-\beta)}} - \frac{1}{x} \right) \frac{1-bx}{\sqrt{(1-x)(1-\frac{x}{\alpha})}} \right| dx.$$

Let $u_0 \in \mathbb{R}$ be such that $0 < |\beta| < u_0 < 1$ and $u \in (|\beta|, u_0)$.

Since

$$\frac{1-bx}{(1+xb/a)} \leq 1,$$

then, for $x \in (0, u_0]$,

$$\frac{1-bx}{\sqrt{(1-x)(1+xb/a)}} \leq \frac{1}{\sqrt{1-u_0}}.$$

Notice that both sides of this last inequality are positive. We deduce that

$$\begin{aligned} |h_1(u)| \leq & \frac{1}{\sqrt{1-u_0}} \int_u^{u_0} \left| \frac{1}{\sqrt{x(x-\beta)}} - \frac{1}{x} \right| dx \\ & + \int_{u_0}^1 \left| \frac{1}{\sqrt{x(x-\beta)}} - \frac{1}{x} \right| \frac{1}{\sqrt{(1-x)}} dx. \end{aligned}$$

For β fixed, the sign of the function

$$\frac{1}{\sqrt{x(x-\beta)}} - \frac{1}{x}$$

does not change and, on the interval $[u_0, 1]$, it is a continuous function of x, so there exists a bound M_1 of the modulus of the function. Thus

$$|h_1(u)| \leq \frac{1}{\sqrt{1-u_0}} \left| \int_u^{u_0} \left(\frac{1}{\sqrt{x(x-\beta)}} - \frac{1}{x} \right) dx \right| + M_1 \int_{u_0}^1 \frac{1}{\sqrt{(1-x)}} dx. \tag{2.10}$$

In order to find an explicit bound M_1, we consider two cases:

- For $\beta \geq 0$ ($c \leq 0$), we have

$$\left| \frac{1}{\sqrt{x(x-\beta)}} - \frac{1}{x} \right| \leq \frac{1}{\sqrt{u_0(u_0-\beta)}} - 1 = \frac{1}{\sqrt{u_0(u_0-|\beta|)}} - 1.$$

- For $\beta < 0$ ($c > 0$), we have

$$\left| \frac{1}{\sqrt{x(x-\beta)}} - \frac{1}{x} \right| \leq \frac{1}{u_0} - \frac{1}{\sqrt{1-\beta}} = \frac{1}{u_0} - \frac{1}{\sqrt{1+|\beta|}}.$$

We finally take

$$M_1 = \max\left\{ \frac{1}{\sqrt{u_0(u_0-|\beta|)}} - 1, \frac{1}{u_0} - \frac{1}{\sqrt{1+|\beta|}} \right\}.$$

Now, we compute the integrals in Eq. (2.10); obtaining

$$\int_u^{u_0} \frac{dx}{\sqrt{x(x-\beta)}} = 2 \log \left(\sqrt{x-\beta+\sqrt{x}} \right) \Big|_u^{u_0},$$

from where we get

$$\int_u^{u_0} \left(\frac{1}{\sqrt{x(x-\beta)}} - \frac{1}{x} \right) dx = 2 \log \left(\frac{1+\sqrt{1-\frac{\beta}{u_0}}}{1+\sqrt{1-\frac{\beta}{u}}} \right).$$

One also has that

$$\int_{u_0}^1 \frac{dx}{\sqrt{1-x}} = 2\sqrt{1-u_0}.$$

Thus, we conclude

$$|h_1(u)| < \frac{1}{\sqrt{1-u_0}} \left| 2\log\left(\frac{1+\sqrt{1-\frac{\beta}{u_0}}}{1+\sqrt{1-\frac{\beta}{u}}} \right) \right| + 2M_1\sqrt{1-u_0}.$$

Finally, by doing tedious computations one gets

$$|h_1(u)| < \frac{2\log(1+\sqrt{2})}{\sqrt{1-u_0}} + 2M_1\sqrt{1-u_0}.$$

□

In a second step, we analyze the h_2- function.

Lemma 2.3. Let $0 < b_0 < 1$ fixed. For every $b \in (b_0, 1)$ and for every a such that

$$(\sqrt{1+x(b/a)})\sqrt{1-x} < 1 - bx,$$

we have the following upper bound for the function h_2:

$$|h_2(u)| < 2\ln(2)$$

Proof. We have

$$|h_2(u)| \leq \int_u^1 \frac{dx}{x} \left| \frac{1-bx-\sqrt{(1-x)(1-x/\alpha)}}{\sqrt{(1-x)(1-x/\alpha)}} \right|.$$

Notice that

$$\sqrt{1-x} < 1 - x < 1 - bx.$$

This implies that there exists $d > 1$ close enough to 1 such that

$$d\sqrt{1-x} < 1 - bx,$$

which is equivalent to the existence of a large enough such that

$$(\sqrt{1+xb/a})\sqrt{1-x} < 1 - bx,$$

when $1 > b > b_0$.

Thus, for a, b fulfilling the conditions given in the statement of the Lemma, we have that

$$\int_u^1 \frac{dx}{x} \left| \frac{1-bx-\sqrt{(1-x)(1-x/\alpha)}}{\sqrt{(1-x)(1-x/\alpha)}} \right| = \int_u^1 \frac{1-bx-\sqrt{(1-x)(1-x/\alpha)}}{\sqrt{(1-x)(1-x/\alpha)}} \frac{dx}{x},$$

obtaining

$$|h_2(u)| < \int_u^1 \frac{dx}{x} \frac{1-\sqrt{1-x}}{\sqrt{1-x}}. \tag{2.11}$$

The upper bound of h_2 can be explicitly integrated giving

$$|h_2(u)| < \left|[-2\ln(1+\sqrt{1-x})]_u^1\right| \leq 2\ln(2).$$

From where we obtain the result. □

We finally get, using the two previous Lemmas, that

$$F_{a,b,c}(u) = \frac{h_{a,b,c}(u)}{\sqrt{ab}} - \frac{\ln u}{\sqrt{ab}}, \tag{2.12}$$

where $h_{a,b,c} = h_1 + h_2$ is a bounded function in the region $|\beta| < u < 1$, with

$$|h_{a,b,c}(u)| \leq \frac{2\ln(1+\sqrt{2})}{\sqrt{1-u_0}} + 2M_1\sqrt{1-u_0} + 2\ln(2).$$

We denote by M the function defined by

$$M(u_0, |\beta|) = \frac{2\ln(1+\sqrt{2})}{\sqrt{1-u_0}} + 2M_1(u_0, |\beta|)\sqrt{1-u_0} + 2\ln(2),$$

for $u_0 \in (0,1)$.

Proposition 2.4. Let $0 < b_0 < 1$ and $0 < c_0 < 1$ be fixed and such that $0 < \frac{c_0}{b_0} < 1$. For all $b \in (b_0, 1)$, all $u_0 \in (\frac{c_0}{b_0}, 1)$ and all $c \in (-c_0, c_0)$, such that

$$0 \leq |c| < be^{-2\pi\sqrt{ab} - M(u_0, \frac{c_0}{b_0})}, \tag{2.13}$$

the equation

$$F_{a,b,c}(u) = 2\pi, \tag{2.14}$$

has a unique solution $u = u_S(a,b,c)$ in $(|\frac{c}{b}|, u_0)$, for a large enough, which verifies

$$|\beta| < u_S < e^{-2\pi\sqrt{ab} + M(u_0, \frac{c_0}{b_0})}.$$

In particular,

$$\lim_{a\to\infty} u_S(a,b,c) = 0.$$

Proof. Equation (2.14) becomes:

$$\frac{1}{\sqrt{ab}} h_{a,b,c}(u) - \frac{1}{\sqrt{ab}} \ln u = 2\pi. \tag{2.15}$$

Equation (2.15) can be expressed in terms of a fixed point problem $u = f(u)$, with

$$f(u) = e^{-2\pi\sqrt{ab}+h_{a,b,c}(u)}.$$

Notice that we have $|h_{a,b,c}(u)| < M(u_0, |\beta|)$, with

$$M(u_0, |\beta|) = \frac{2\ln(1+\sqrt{2})}{\sqrt{1-u_0}} + 2M_1(u_0, |\beta|)\sqrt{1-u_0} + 2\ln(2).$$

We also have that $0 < b_0 < b < 1$ and $|c| < c_0$, which implies $|\beta| < \frac{c_0}{b_0}$, giving

$$M_1(u_0, |\beta|) = \max\left\{ \frac{1}{\sqrt{u_0(u_0-|\beta|)}} - 1, \frac{1}{u_0} - \frac{1}{\sqrt{1+|\beta|}} \right\} \leq M_1(u_0, \frac{c_0}{b_0}).$$

Thus, we arrive at

$$e^{-2\pi\sqrt{ab}-M(u_0,\frac{c_0}{b_0})} < f(u) < e^{-2\pi\sqrt{ab}+M(u_0,\frac{c_0}{b_0})}. \tag{2.16}$$

We show, by continuity, the existence of a solution to the fixed point problem, if $f(|\beta|) > |\beta|$ and $f(u_0) < u_0$. The first condition is given by Eq. (2.13) and Eq. (2.16); while the second is trivially verified from inequality (2.16), for a large enough to have $e^{-2\pi\sqrt{ab}+M(u_0,\frac{c_0}{b_0})} < u_0$.

To prove the uniqueness, let us prove the general fact that if the parameters a, b, and c are fixed, then the value u fulfilling the equation $F_{a,b,c}(u) = 2\pi$ has to be unique.

Let us consider fixed values of the parameters a, b, and c. Let u_1, u_2 be such that $F_{a,b,c}(u_1) = 2\pi$ and $F_{a,b,c}(u_2) = 2\pi$, then

$$\frac{1}{b}\int_{u_1}^{1} \frac{1-bx}{\sqrt{x(x-\beta)(1-x)(x-\alpha)}}dx = \frac{1}{b}\int_{u_2}^{1} \frac{1-bx}{\sqrt{x(x-\beta)(1-x)(x-\alpha)}}dx,$$

without loss of generality, let us assume that $u_1 \leq u_2$. Then, one gets

$$\int_{u_1}^{u_2} \frac{1-bx}{\sqrt{x(x-\beta)(1-x)(x-\alpha)}}dx = 0.$$

Since, in the interval of integration, we have the condition

$$\frac{1-bx}{\sqrt{x(x-\beta)(1-x)(x-\alpha)}} > 0,$$

then we conclude that $u_1 = u_2$, getting the unicity of the solution. □

Using Proposition 2.4, we can deduce Theorem 2.1 which gives a precise description of the TRE and is the main result of this subsection.

Proof of Theorem 2.1. The proof follows directly from Proposition 2.4 and the relation $\Delta\phi_{a,b,c}(\varepsilon) = F_{a,b,c}(\sin^2\varepsilon)$, since the change of variables $u = \sin^2\varepsilon$ is a bijection from $[0, \pi/2]$ to $[0, 1]$. □

Analysis of the region $u < |\beta|$

We consider now the function $F_{a,b,c}$ in the region $|u| < |\beta|$. We recall that this analysis only concerns the case with $c > 0$ and that the expression (2.12) does not hold.

Lemma 2.5. There exists a holomorphic function k defined on

$$\mathcal{D} = \{v \in \mathbb{C} : |v| < \sqrt{|\beta|}\}$$

such that

$$F_{a,b,c}(u) = k(\sqrt{u})$$

i.e. $F(v^2) = k(v)$.

Proof. Turning around the origin in u, we do not catch the cycle δ as in the TRE, but a non-closed path. Turning twice around $x = 0$ the path closes giving a closed cycle $\tilde{\delta}$ winding twice around the branch point $x = 0$ only. Note that here $\int_{\tilde{\delta}} \omega = 0$. Indeed, the problem boils down to integrate $x \mapsto \frac{1}{\sqrt{x}}$ on a loop winding twice around zero. Let k be $k(v) = F_{a,b,c}(v^2)$. Then, we deduce that:

$$k(ve^{2\pi i}) = F_{a,b,c}(v^2 e^{4\pi i}) = F_{a,b,c}(v^2) + \int_{\tilde{\delta}} \omega = F_{a,b,c}(v^2) = k(v).$$

Moreover, $k(0) = \int_0^1 \omega < \infty$ is a complete elliptic integral. Hence, k has a removable singularity at the origin and extends to a holomorphic function on $\mathcal{D}$. □

In this case, equation $\Delta\phi_{a,b,c}(\varepsilon) = 2\pi$ becomes $k_{a,b,c}(\sqrt{\sin^2\varepsilon}) = 2\pi$, where $k_{a,b,c}$ is a bounded and analytic function. Note that the nature of this equation, valid in the small region $\mathcal{D}$, is completely different from Eq. (2.15). Since, for c fixed and small, we have that the values of $\Delta\phi_{a,b,c}(\varepsilon)$ in a neighborhood of the origin vary a lot in the first case due to the logarithmic behavior, and they do not in the second case due to the square root behavior.

We conclude that the complex structure does not allow us to deduce a useful asymptotic behavior of the function, as in the previous case. Nevertheless, the problem of the existence of the TRE in this last region will be treated in the next chapter.

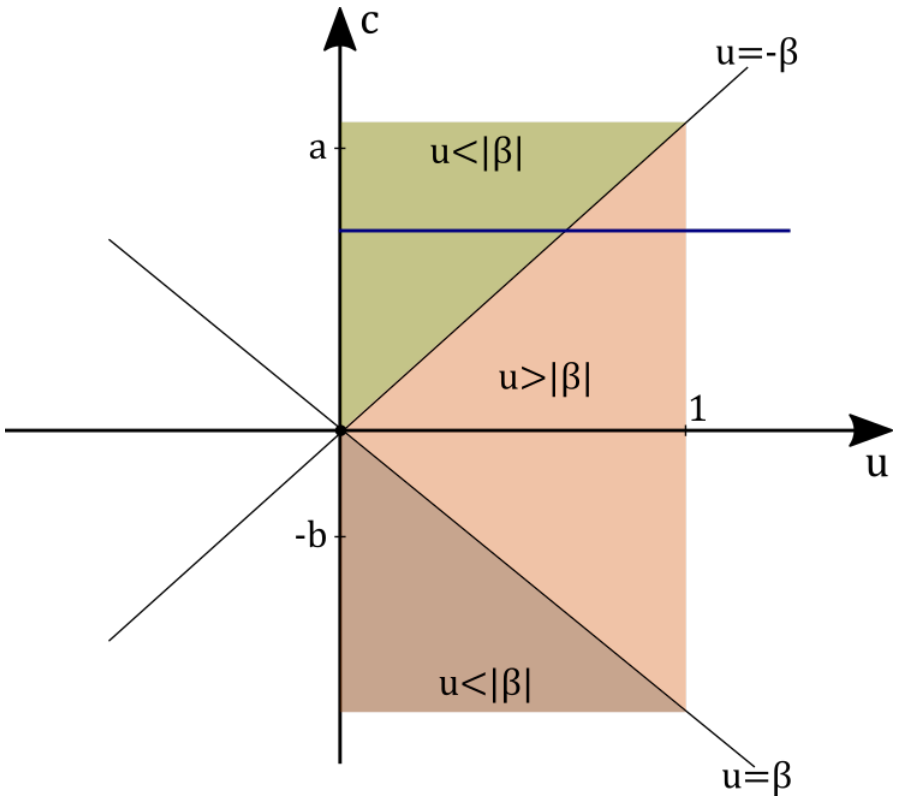

Figure 2.7: The function $\Delta\phi = F_{a,b,c}(u)$ has a logarithmic behavior in the orange region which corresponds to $u > |\beta|$. For the region $u \leq |\beta|$, one has two cases. In the green region, the function $F_{a,b,c}(u)$ has a square-root behavior, while in the brown one, there are no solutions. Considering c as a fixed parameter is equivalent to analyzing horizontal lines, such as the blue one.

2.3 The Dzhanibekov effect

A similar analysis can be used to describe the DE [14]. The video [14] shows that the motion of the wing nut is first guided by a screw which induces an almost perfect rotation around the central axis. In terms of Euler's angles, this leads to a very large angular speed $\dot{\phi}$ with respect to $\dot{\psi}$ (i.e. $\frac{d\psi}{d\phi} \simeq 0$). Since the device generating the rotation of the rigid body blocks the flip motion, the angle ψ is initially of the order of $\pm\frac{\pi}{2}$. We deduce that the initial point of the dynamics is very close to one of the unstable fixed points represented in Fig. 2.5, with a parameter $c \simeq 0$.

Using Eq. (2.4) with $\varepsilon = 0$, DE is described by:

$$\Delta\phi = \int_{-\frac{\pi}{2}}^{\frac{\pi}{2}} \frac{1 - b\cos^2\psi}{\sqrt{(a + b\cos^2\psi)(c + b\cos^2\psi)}} d\psi,$$

with $c > 0$. In this case, we search for the value of the variation $\Delta\phi$ from the beginning of the movement to the moment of the twist of the wing nut. We assume that the wing nut performs a perfect twist for which ψ goes from $-\frac{\pi}{2}$ to $-\frac{\pi}{2}$. In this subsection, we now show that:

$$\Delta\phi = \frac{1}{\sqrt{ab}}[h_{a,b}(c) - \ln(c)], \tag{2.17}$$

where $h_{a,b}$ is a bounded function when $c \to 0$.

Since in this case $\varepsilon = 0$, we analyze the function $F_{a,b,c}$ as a function of c to find the initial conditions such that we observe the Dzhanibekov effect. This is why, in this case, the expression of $\Delta\phi$ is given as a function of c, which corresponds to analyzing the axis c on the figure 2.7. Moreover, the logarithmic divergence of $\Delta\phi$ occurs due to the confluence of the two branch points in $x = \beta$ and $x = 0$, which gives a pole as in the TRE. Consequently, the speed $d\phi/d\psi$ increases tremendously in a neighborhood of this point.

DE with many rotations around the intermediate axis can be observed for a sufficiently small positive value of c. We stress that the number of turns does not need to be complete. We give a more detailed description of this fact in Section 3.1.

Using the same change of coordinates introduced for the TRE, one gets

$$\Delta\phi = \int_0^1 \frac{1}{b} \frac{1 - bx}{\sqrt{x(x - \beta)(1 - x)(x - \alpha)}} dx,$$

with $\alpha = -\frac{a}{b}$ and $\beta = -\frac{c}{b}$. In this case, on the complex plain, one obtains a complete Abelian integral, for a cycle connecting the two branching points 0 and 1. It starts on one sheet of the Riemann surface and ends on the other.

In order to obtain useful approximations, we estimate the integral in the real domain. We have

$$\Delta\phi_{a,b}(c) = \frac{1}{\sqrt{ab}} \int_0^1 \frac{1 - bx}{\sqrt{x(x - \beta)(1 - x)(1 - \frac{x}{\alpha})}} dx.$$

This last integral can be written as the sum of two terms:

$$\Delta\phi_{a,b}(c) = \frac{1}{\sqrt{ab}} \left(f(c) + g(c)\right),$$

with

$$g(c) = \int_0^1 \frac{1}{\sqrt{x(x-\beta)}} dx,$$

and

$$f(c) = \frac{1}{\sqrt{ab}} \int_0^1 \frac{1}{\sqrt{x(x-\beta)}} \left(\frac{1-bx}{\sqrt{(1-x)(1-\frac{x}{\alpha})}} - 1 \right) dx.$$

Proposition 2.6. Let $0 < b_0 < 1$ be fixed. For every $b \in (b_0, 1)$ and every a such that

$$(\sqrt{1+x(b/a)})\sqrt{1-x} < 1 - bx,$$

we have the following upper bound for the function $\Delta\phi_{a,b}(c)$:

$$|\Delta\phi_{a,b}(c)| < \frac{1}{\sqrt{ab}} \left(2\ln(2) + 2\ln\left(\frac{\sqrt{b} + \sqrt{b+c}}{\sqrt{c}} \right) \right).$$

Proof. Straightforward computations lead to

$$g(c) = 2\ln\left(\frac{\sqrt{b} + \sqrt{b+c}}{\sqrt{c}} \right) = \ln\left(\frac{(\sqrt{b} + \sqrt{b+c})^2}{c} \right).$$

We find, in a second step, a bound for the function f :

$$|f(c)| \leq \frac{1}{\sqrt{ab}} \int_0^1 \frac{1}{\sqrt{x(x-\beta)}} \left| \frac{1 - bx - \sqrt{(1-x)(1-\frac{x}{\alpha})}}{\sqrt{(1-x)(1-\frac{x}{\alpha})}} \right| dx.$$

As explained in Lemma 2.3, for a, b fulfilling the conditions given in the statement, we have that

$$\int_u^1 \frac{dx}{x} \left| \frac{1 - bx - \sqrt{(1-x)(1-x/\alpha)}}{\sqrt{(1-x)(1-x/\alpha)}} \right| = \int_u^1 \frac{1 - bx - \sqrt{(1-x)(1-x/\alpha)}}{\sqrt{(1-x)(1-x/\alpha)}} \frac{dx}{x},$$

giving

$$|f(c)| \leq \frac{1}{\sqrt{ab}} \int_0^1 \frac{1}{x} \left(\frac{1 - \sqrt{1-x}}{\sqrt{1-x}} \right) dx \leq 2\ln 2.$$

□

It is then straightforward to derive Eq. (2.17) defining

$$h_{a,b}(c) = 2\ln\left(\sqrt{b} + \sqrt{b+c} \right) + 2\ln(2).$$

We have obtained that

$$|\Delta\phi_{a,b}(c)| < \frac{1}{\sqrt{ab}}\left(2\ln(2) + \ln\frac{(\sqrt{b}+\sqrt{b+c})^2}{c}\right).$$

Thus, a rough estimation of $\Delta\phi$ when $c \to 0$, using this last inequality, is

$$\Delta\phi \simeq \frac{1}{\sqrt{ab}}\left(\ln\left(\frac{4b}{c}\right) + 2\ln 2\right).$$

In the supplementary material of [48], the accuracy of this approximation is investigated numerically for a standard wing nut, showing that, in fact, it is pretty accurate.

Using this estimation of the variation $\Delta\phi$, we conclude that the number of turns that we observe before the flip depends on the shape of the body (because of the dependence of this expression on the parameters a and b) and on the initial condition (encoded on the value of c). Nevertheless, given the fact that the wing nut is guided by the screw at the beginning of the movement, the initial condition will be almost the same every time (and therefore the value of c as well). Thus, the number of turns depends only on the moments of inertia of the wing nut. Finally, a condition on the value of this variation, to observe the DE, is described in Section 3.1.

2.4 The Monster flip

MFE corresponds to a complete turn around the transverse axis together with a small variation of ψ. It can be realized in a neighborhood of the unstable point where $\frac{d\psi}{d\phi} = 0$ (i.e. $\frac{d\phi}{d\psi} = \infty$), as shown in this subsection.

Following the approach used in the previous sections, we consider symmetric initial and final conditions. For rotating trajectories, one gets $\psi_i = -\frac{\pi}{2} - \varepsilon$ and $\psi_f = -\frac{\pi}{2} + \varepsilon$ with $\varepsilon > 0$, regarding the vertical symmetry. For oscillating trajectories near the unstable point $-\frac{\pi}{2}$, we consider the horizontal symmetry, obtaining $\psi_i = \psi_f = -\frac{\pi}{2} + \varepsilon$ (see Fig. 2.5). Notice that, for these later trajectories, the value of ψ varies in $[-\frac{\pi}{2} + \arcsin[\sqrt{|\beta|}], -\frac{\pi}{2} + \varepsilon]$, where $\beta = \frac{-c}{b}$ as in the previous sections.

Thus, we search for a solution ε close to zero, of $\tilde{\Delta}\phi(\varepsilon) = 2\pi$, where

$$\tilde{\Delta}\phi(\varepsilon) = 2\int_{\psi_1}^{\frac{-\pi}{2}+\varepsilon} \frac{1 - b\cos^2\psi}{\sqrt{a + b\cos^2\psi}\sqrt{c + b\cos^2\psi}} d\psi, \tag{2.18}$$

with $\psi_1 = -\pi/2$ or $\psi_1 = -\pi/2 + \arcsin[\sqrt{|\beta|}]$, for rotating and oscillating trajectories respectively.

Using the same change of coordinates as for the TRE, we get $\tilde{\Delta}\phi(\varepsilon) = \int_{\cos^2\psi_1}^{\sin^2\varepsilon} \omega$, where ω is defined by Eq. (2.5). Note that, $\cos^2(\psi_1) = 0$ in the rotating case and, by construction, $\cos^2(\psi_1) = |\beta|$ in the oscillating case.

We introduce the function $\tilde{F}_{a,b,c}(u) = \int_{\cos^2\psi_1}^{u} \omega$ and search for solutions of

$$\tilde{F}_{a,b,c}(u) = 2\pi, \quad 0 \leq u \leq 1, \tag{2.19}$$

in the rotating case or

$$\tilde{F}_{a,b,c}(u) = 2\pi, \quad |\beta| \leq u \leq 1, \tag{2.20}$$

for oscillating trajectories.

In this section we show that, the solution of $\tilde{\Delta}\phi_{a,b,c} = \tilde{F}_{a,b,c}(u)$ can be approximated as $\varepsilon \simeq \frac{\sqrt{|\beta|}}{2} e^{\pi\sqrt{ab}}$. The accuracy of this approximation is shown numerically in supplementary material of [48].

As a consequence, for a body with $ab \geq 1$, MFE can be observed only in a neighborhood of the separatrix, where $|\beta| \ll 1$. The rotation of the skateboard around its transverse axis is constrained by the condition $\varepsilon \geq \sqrt{|\beta|}$. This result quantifies the difficulty of performing MFE. For an angle ε of 30 degrees, this leads for a standard skateboard to $c \simeq 10^{-3}$, while the maximum value of c is of the order of 10.

Following the study done for the TRE, one has the existence of two different behaviors of the function $\tilde{F}_{a,b,c}(u)$ corresponding to the two regions

$0 < u < |\beta|$ and $|\beta| < u < 1$. In the case $0 < u < |\beta|$ (which only concerns rotating trajectories), it can be shown, using the same technique as before, that

$$\tilde{F}_{a,b,c}(u) = \tilde{h}_{a,b,c}(\sqrt{u}),$$

where $\tilde{h}_{a,b,c}$ is a holomorphic function vanishing at the origin. For the region $|\beta| < |u| < 1$, one gets

$$\tilde{F}_{a,b,c}(u) = \frac{1}{\sqrt{ab}}\tilde{h}_{a,b,c}(u) + \frac{1}{\sqrt{ab}}\ln(u),$$

where $\tilde{h}_{a,b,c}$ is a bounded single-valued function. Note the change of sign in front of the logarithmic term with respect to Eq. (2.12).

We consider now the different integrals in the real domain to obtain the approximation mentioned before.

Approximation for $0 < u < |\beta|$

We consider the function $\tilde{F}_{a,b,c}$ in the region $u < |\beta|$. We stress that this analysis only concerns the case with $c > 0$; hence, $\cos^2\psi_1 = 0$.

Since we search for solutions of $\tilde{F}_{a,b,c}(u) = 0$ with $u \ll 1$, we can approximate the function $\tilde{F}$ as follows

$$\tilde{F}_{a,b,c}(u) = \frac{1}{b}\int_0^u \frac{1-bx}{\sqrt{x(x-\beta)(1-x)(x-\alpha)}}dx \simeq \frac{1}{\sqrt{ab}}\int_0^u \frac{dx}{\sqrt{x(x-\beta)}},$$

where we have replaced x by 0 except in the factor $\sqrt{x(x-\beta)}$. Integrating the right-hand side, one obtains

$$\tilde{F}_{a,b,c}(u) \simeq \frac{2}{\sqrt{ab}}\ln\left(\sqrt{1+\frac{u}{|\beta|}} + \sqrt{\frac{u}{|\beta|}}\right).$$

The equation $2\pi = \Delta\phi_{a,b,c} = \tilde{F}_{a,b,c}(u)$ can then be approximated as

$$\sqrt{1+\frac{u}{|\beta|}} + \sqrt{\frac{u}{|\beta|}} \simeq e^{\pi\sqrt{ab}}. \tag{2.21}$$

The variation ε of MFE can be estimated as

$$\varepsilon \simeq \pi\sqrt{ac}. \tag{2.22}$$

using the Taylor expansion for $\exp(v)$, $\sqrt{1+v}$ and $\sin(v)$, and neglecting higher order terms.

Since we are in the case $0 < u < |\beta|$, we have $\sqrt{1+\frac{u}{|\beta}} + \sqrt{\frac{u}{|\beta|}} \leq 1+\sqrt{2}$. From where, it is also possible to recover the fact that the function $\tilde{h}_{a,b,c}$ is bounded. Notice that this inequality also gives a strong constraint on the parameters a and b, when we replace it in Eq. (2.21), obtaining

$$ab \leq \frac{[\ln(1+\sqrt{2})]^2}{\pi^2}.$$

This bound on the product ab is of the order of 0.079 which means that in this situation we cannot have very asymmetric rigid bodies.

Approximation for $0 \leq |\beta| < u$

In this case, we can use the same approximation for the function $\tilde{F}_{a,b,c}$ as in the previous case, but this approximation will be valid just for ab large, since in this case $\cos^2\psi_1 = 0$ or $\cos^2\psi_1 = |\beta|$. Thus, for ab large enough, we have

$$\tilde{F}_{a,b,c}(u) = \frac{1}{b}\int_{\cos^2\psi_1}^{u} \frac{1-bx}{\sqrt{x(x-\beta)(1-x)(x-\alpha)}}dx \simeq \frac{1}{\sqrt{ab}}\int_0^u \frac{dx}{\sqrt{x(x-\beta)}},$$

obtaining again Eq.(2.21).

An approximation for ε can be derived in the limit $u/|\beta| \gg 1$, one gets

$$\sin(\varepsilon) \simeq \frac{\sqrt{|\beta|}}{2}e^{\pi\sqrt{ab}}$$

A first-order Taylor expansion leads to

$$\varepsilon \simeq \frac{\sqrt{|\beta|}}{2}e^{\pi\sqrt{ab}}, \tag{2.23}$$

which also allows to estimate the bounded function $\tilde{h}_{a,b,c}$. The accuracy of these different approximations is illustrated numerically in [48].

2.5 Conclusion

In conclusion, in this chapter we analyzed the tennis racket effect, the Dzhanibekov effect and the monster flip by setting a, b and c as fixed parameters and analyzing these phenomena as functions of ε. In the next chapter, we make a more general analysis fixing only the parameters a and b (describing the shape of the body) and doing a study of c and ε simultaneously which leads to interesting results.

Chapter 3

Signatures of physical constraints in rotating rigid bodies

The parameters a and b play a crucial role in the properties derived in the previous Chapter. These parameters are related to the shape of the body (since they are given in terms of the moments of inertia) and fulfill the physical constraint introduced in Section 1.4.

However, as mentioned before, in the paper [69], a direct link between Euler's equations and Bloch's equations is given, these later equations describe the control of spin 1/2-particles employing electromagnetic fields. In this quantum counterpart, the moments of inertia play the role of additional degrees of freedom used to design control fields, so they are not related to the shape of a rigid body and do not fulfill the aforementioned physical constraint.

Thus, the study of Euler's equations, in both cases, the physical and the non-physical case is interesting. Moreover, these two cases can be differentiated from the parameters a and b as shown by the constraint derived in Proposition 1.3.

In this Chapter, we prove that this constraint has geometrical signatures on the rigid body dynamics, detecting these signatures in the tennis racket effect and in the Montgomery phase [1] .

The results of this chapter have been published in Journal of Physics A: Mathematical and Theoretical [36].

[1]The Montgomery phase is a well-known geometric phase whose definition can be found in Section 3.5

3.1 Geometric and dynamic framework

In the previous chapter and different works [5, 70], a study of the TRE has been made in a neighborhood of the separatrix. The corresponding trajectories are assumed to exhibit the TRE since the separatrix is the curve connecting two unstable points, which are at the origin of this geometric effect [3, 5].

Recall that the TRE is characterized by a variation $\Delta\phi = 2\pi$ when $\Delta\psi = \pi - 2\varepsilon$ [2]. In the previous chapter, c [3] was considered as a small parameter, giving rise to approximations for $\Delta\phi = F_{a,b,c}(\varepsilon)$, when $\varepsilon \simeq 0$. We then obtained different behaviors of F as a function of ε. However, we did not perform a full analysis of F, as a function of two variables c and ε.

In this Chapter, we analyze F, as a function of c and ε. We show that the pairs of values (c, ε), such that $F_{a,b}(c, \varepsilon) = 2\pi$ define a curve denoted $\mathcal{C}$. We find geometrical signatures that the constraint on the parameters a and b imposes on this curve and, in addition, we take advantage of this analysis to make a global study of the TRE [4].

For the rest of the chapter, the parameters a and b are fixed (which is equivalent to fixing the rigid body that we analyze). We start studying the dynamics of the reduced system

$$\frac{d\psi}{d\phi} = \frac{(a + b\cos^2\psi)\cos\theta}{1 - b\cos^2\psi}, \tag{3.1}$$

$$\frac{d\theta}{d\phi} = \frac{b\sin\theta\sin\psi\cos\psi}{1 - b\cos^2\psi}, \tag{3.2}$$

with first integral $c = a - \sin^2\theta\,(a + b\cos^2\psi)$. The phase portrait of this system is represented in Fig. 3.1. In this system, the evolution of the angle ϕ can be analyzed as well since ϕ plays the role of time.

We define the relation $\mathcal{C}$ as the set of pairs (c, ε) such that when considering symmetric initial and final values of ψ, $\psi_i = -\frac{\pi}{2} + \varepsilon$ and $\psi_f = \frac{\pi}{2} - \varepsilon$, for the trajectory given by the value of c, the time taken to go from the initial point to the final point along the trajectory is 2π (*i.e.* $\Delta\phi = 2\pi$).

Equation (3.1) can be used to study this effect, as mentioned in the previous Chapter. A difficulty lies in the fact that the sign of the term $\cos\theta$

[2] A perfect TRE is then described by $\varepsilon = 0$, ε describing the defect to a perfect TRE.

[3] c parametrizes the distance to the separatrix and depends on the initial condition of the dynamics.

[4] A local, versus global, study of the TRE corresponds therefore to a local (close to $c = 0$), or global (any value of c) study of the curve $\mathcal{C}$, respectively.

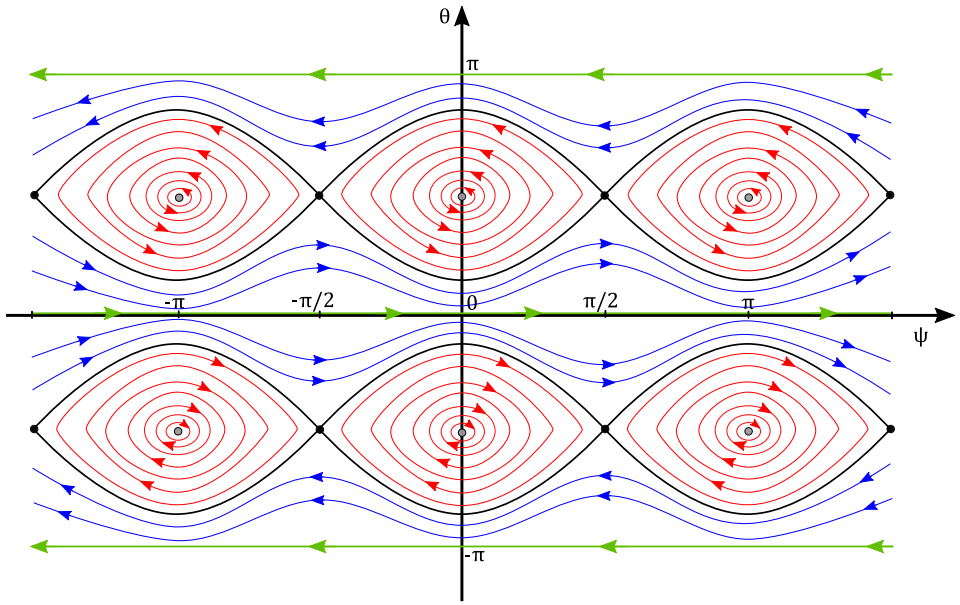

Figure 3.1: Schematic representation of the phase portrait (ψ, θ). The blue and red lines correspond respectively to the rotating and oscillating trajectories. The separatrix $(c = 0)$ is plotted in black. The grey dots and the green curves have the values $c = -b$ and $c = a$ respectively.

given by

$$\cos\theta = \pm\sqrt{\frac{c + b\cos^2\psi}{a + b\cos^2\psi}}, \tag{3.3}$$

changes and then the sign of the derivative $d\psi/d\phi$ depends on the region of the phase space we consider.

To detect this change of sign, we introduce the curve

$$\mathcal{S} = \left\{(c, \varepsilon) \mid c = -b\sin^2(\varepsilon)\right\}, \tag{3.4}$$

for which $\cos\theta$ is equal to 0; ε is determined by the initial condition $\psi = -\pi/2 + \varepsilon$. A change of sign corresponds therefore to an intersection point between the curves $\mathcal{C}$ and $\mathcal{S}$.

In this section, we prove that $\mathcal{C}$ is a curve given as a graph of a function $\varepsilon = \varepsilon(c)$. We derive implicit equations describing this function and we study different properties of the curve leading to a global description of the TRE.

Recall that, at the end of Chapter 1, we defined a *physical rigid body*, we introduced the geometrical constant

$$\mathcal{I} = \frac{1-b}{\sqrt{b\,(a+b)}}, \tag{3.5}$$

and we proved that the moments of inertia I_x, I_y, I_z describe a physical rigid body if and only if $\mathcal{I}$ satisfies the inequality $\mathcal{I} \geq 1$.

The following Theorem is proved in Section 3.3 and is the main signature of the physical constraint on the TRE.

Theorem 3.1. The relation $\mathcal{C}$ is a curve given as a graph of a function $\varepsilon = \varepsilon\,(c)$. Moreover, the function $\varepsilon\,(c)$ is injective, if and only if the geometric constant $\mathcal{I}$ verifies $\mathcal{I} \geq 1$, that is if and only if the rigid body is physical.

3.2 Description of the curve $\mathcal{C}$ associated to the TRE

We first establish different results about the structure of the relation $\mathcal{C}$.

Lemma 3.2. The set $\mathcal{C}$ is a curve in the plane (c, ε) given as a graph of a function $c \mapsto \varepsilon\,(c)$.

Proof. We need to prove that for a fixed value of c, there exists only one value of ε. Let us assume that there exist two values of ε, namely ε_1 and ε_2 fulfilling the definition of the curve $\mathcal{C}$. The time taken to go from $-\frac{\pi}{2}+\varepsilon_k$ to $\frac{\pi}{2}-\varepsilon_k$ along the curve is equal to 2π for $k = 1, 2$. We deduce that the time needed to go from one point to the other (for example between $-\frac{\pi}{2}+\varepsilon_1$ and $-\frac{\pi}{2}+\varepsilon_2$) is 0. We conclude that $\varepsilon_1 = \varepsilon_2$. □

First implicit equation

In this part of the section, we analyze the equation used in the previous Chapter (Eq. (3.6)) from a new perspective, using the curves $\mathcal{S}$ and $\mathcal{C}$.

We consider the derivative $\frac{d\psi}{d\phi}$ for $\theta \in [0, \frac{\pi}{2})$, i.e. in the case $\cos\theta > 0$. Using Eqs. (3.1) and (3.3), one obtains that the TRE can be described as the solutions (c, ε) of the implicit equation

$$2\pi = \int_{-\pi/2+\varepsilon}^{\pi/2-\varepsilon} \frac{1 - b\cos^2\psi}{\sqrt{(b\cos^2\psi + a)\,(b\cos^2\psi + c)}} d\psi. \tag{3.6}$$

The square root in the integrand of Eq. (3.6) is well defined if $c \geq -b\sin^2(\varepsilon)$, *i.e.* before intersecting the curve $\mathcal{S}$.

For non-negative values of ε, one can consider the change of coordinates given by $x = \cos^2\psi$, which leads to

$$2\pi = F_{a,b}(c,u) = \frac{1}{\sqrt{ab}}\int_u^1 \frac{1-bx}{\sqrt{x(1-x)\left(1+\frac{b}{a}x\right)\left(x+\frac{c}{b}\right)}}dx, \tag{3.7}$$

where $u = \sin^2\varepsilon$, a and b are fixed parameters and c and u the variables. Note that $u \geq 0$ and $\mathcal{S} = \{(c,u) \mid c = -bu\}$.

We now establish some properties of $\mathcal{C}$ in the region where the curve is described by Eq. (3.6).

Proposition 3.3. The function $\varepsilon(c)$ given by the solutions of the implicit Eq. (3.6) is an injective decreasing function.

Proof. Using the symmetry of the integrand, we can transform Eq. (3.6) into

$$\pi = I_{a,b}(c,\varepsilon) = \int_0^{\pi/2-\varepsilon} \frac{1-b\cos^2\psi}{\sqrt{(b\cos^2\psi+a)(b\cos^2\psi+c)}}d\psi. \tag{3.8}$$

We analyze the set $\mathcal{C}$ near a point (c_1,ε_1), for which the curve is described by Eq. (3.8). The function given by $I_{a,b}(c,\varepsilon)-\pi$ is a continuously differentiable function such that $I_{a,b}(c_1,\varepsilon_1)-\pi = 0$. Thus, we can use the Implicit Function Theorem to compute the derivative of the function $\varepsilon(c)$. The partial derivative of the function with respect to ε is

$$\begin{aligned}
&\frac{\partial\left(I_{a,b}(c,\varepsilon)-\pi\right)}{\partial\varepsilon}(c_1,\varepsilon_1)\\
&= -\frac{1-b\cos^2(\pi/2-\varepsilon_1)}{\sqrt{(b\cos^2(\pi/2-\varepsilon_1)+a)(b\cos^2(\pi/2-\varepsilon_1)+c_1)}}\\
&\neq 0.
\end{aligned}$$

This partial derivative is not equal to 0. Thus, the Implicit Function Theorem gives the existence of a local solution near the point (c_1,ε_1) and leads to the following expression for the derivative

$$\frac{d\varepsilon}{dc} = -\frac{\partial I_{a,b}}{\partial c}\Bigg/\frac{\partial I_{a,b}}{\partial\varepsilon}\Bigg|_{\varepsilon(c)}. \tag{3.9}$$

Using the definition of $I_{a,b}$, we obtain

$$\frac{d\varepsilon}{dc} = -\frac{\int_0^{\pi/2-\varepsilon(c)} \frac{1-b\cos^2\psi}{\sqrt{b\cos^2\psi+a}} \frac{1}{2(b\cos^2\psi+c)^{\frac{3}{2}}} d\psi}{\frac{1-b\cos^2(\pi/2-\varepsilon(c))}{\sqrt{(b\cos^2(\pi/2-\varepsilon(c))+a)(b\cos^2(\pi/2-\varepsilon(c))+c)}}} \leq 0. \tag{3.10}$$

Since Eq. (3.10) is valid near any point for which the curve $\mathcal{C}$ is described by the first implicit equation, we conclude that this part of the curve is strictly decreasing (the expression (3.10) has a discrete set of zeros). The injectivity follows from this property. □

Equation (3.7) can be used to study the existence of a TRE on the separatrix and a perfect TRE as shown by the following result.

Proposition 3.4.

1. The TRE always occurs on the separatrix.
2. A perfect TRE occurs if and only if $\mathcal{J} < 2$.

Proof.

1. Having a TRE on the separatrix is equivalent to finding $u_0 = \sin^2(\varepsilon_0)$ such that

$$2\pi = F_{a,b}(0, u_0) = \frac{1}{\sqrt{ab}} \int_{u_0}^{1} \frac{1-bx}{x\sqrt{(1-x)\left(1+\frac{b}{a}x\right)}} dx. \tag{3.11}$$

   Using the expression on the right-hand side of Eq. (3.11), we observe that $F_{a,b}(0,u)$ goes respectively to $+\infty$ and 0 when u goes to 0 and 1. Thus, we conclude that there exists $u_0 \in (0,1)$ such that $2\pi = F_{a,b}(0,u_0)$.

2. Showing the existence of a perfect TRE ($\varepsilon = 0$) amounts to show the existence of $c_0 \in (-b, a)$ such that

$$2\pi = F_{a,b}(c_0, 0) = \frac{1}{\sqrt{ab}} \int_{0}^{1} \frac{1-bx}{\sqrt{x(1-x)\left(1+\frac{b}{a}x\right)\left(x+\frac{c_0}{b}\right)}} dx. \tag{3.12}$$

   We have that $F_{a,b}(c,0)$ goes to ∞, when c goes to 0, and following the computations of Sec. 3.5, we know that $2F_{a,b}(c,0)$ is a decreasing function with a greatest lower bound equal to $2\pi\mathcal{J}$. We conclude that a perfect TRE occurs if and only if $\mathcal{J} < 2$.

□

The values ε_0 and c_0 represent the TRE on the separatrix and a perfect TRE respectively. A schematic representation is given in Fig. 3.2. In Section 3.4, we study the dependence of these effects on the parameter a.

Intersection of $\mathcal{C}$ and $\mathcal{S}$

In the previous subsection, we used the first implicit equation to obtain properties of the curve $\mathcal{C}$ and we explained that this equation is valid until the point where the curve $\mathcal{C}$ intersects $\mathcal{S}$ (i.e. when $\cos\theta$ changes sign). We now describe under which conditions these two curves intersect.

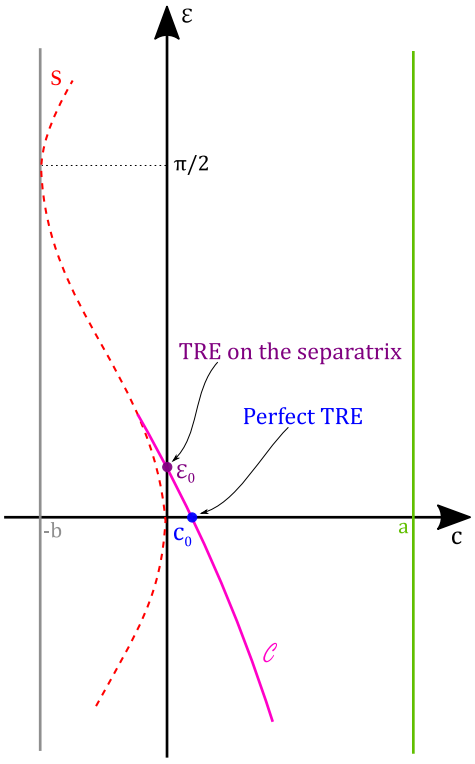

Figure 3.2: Schematic representation in the space (c, ε) of the part of the curve $\mathcal{C}$ (solid magenta line) described by the first implicit equation. The red dashed line represents the set $\mathcal{S}$. The grey and green vertical lines have respectively the equations $c = -b$ and $c = a$. The points ε_0 and c_0 indicate the positions of a TRE on the separatrix and of a perfect TRE (see the text for details).

First, notice that in the region $b\sin^2(\varepsilon) + c < 0$ the integrand of the integral of Eq. (3.6) is not well defined and that the curve $\mathcal{S}$ is delimiting this region. If there exists an intersection point between $\mathcal{C}$ and $\mathcal{S}$, then the coordinate c of the intersection point has to be negative, which corresponds to a positive value of ε since in this case, $\mathcal{C}$ is a decreasing curve (see Fig. 3.2). Thus, we can use Eq. (3.7) to analyze whether or not there exists an intersection point between these curves.

Lemma 3.5. The curves $\mathcal{C}$ and $\mathcal{S}$ intersect in $(0, 1]$, if and only if $\mathcal{I} \leq 2$.

Proof. If $\mathcal{C}$ and $\mathcal{S}$ intersect in $(0, 1]$, then there exists $u^* \in (0, 1]$ such that $F_{a,b}(-bu^*, u^*) = 2\pi$. Using Lemmas 3.16 and 3.17 of Section 3.5, we deduce that $u = 1$ is the minimum of the function $F_{a,b}(-bu, u)$. Thus $F_{a,b}(-b, 1) \leq F_{a,b}(-bu^*, u^*)$, which implies that $\mathcal{I} \leq 2$.

Conversely, an intersection point between the two curves is characterized by the equation $F_{a,b}(c, u) = 2\pi$, with $c = -bu$. The function $F_{a,b}(-bu, u)$ is a continuous function which goes to ∞, when u goes to 0 and verifies

$$F_{a,b}(-bu, u) \to \pi\mathcal{I} \leq 2\pi, \tag{3.13}$$

when u goes to 1 (using Lemma 3.17). We conclude that there exists $u^* \in (0, 1]$, such that $F(-bu^*, u^*) = 2\pi$, and thus, an intersection point between these curves. □

Notice that $u \in (0, 1]$ is equivalent to $\varepsilon \in (0, \frac{\pi}{2}]$, and that the intersection point is unique since $F_{a,b}(-bu, u)$ is a decreasing function (See Lemma 3.16).

Remark 3.6. Using the preceding proof, we deduce that the intersection point is exactly in $u = 1$, if and only if $\mathcal{I} = 2$.

We derived a condition on the parameters that ensures the existence of an intersection point between $\mathcal{C}$ and $\mathcal{S}$. After this intersection point the implicit equation describing the solution curve $\mathcal{C}$ changes as described below. We first recall that the first implicit equation describes the curve $\mathcal{C}$ in the region $\theta \in [0, \frac{\pi}{2})$, i.e. $\cos\theta > 0$. Notice that, if there exists an intersection point between $\mathcal{C}$ and $\mathcal{S}$, then $c < 0$, which corresponds to oscillating trajectories. The period T_ϕ of these closed orbits can be calculated using the relation

$$\frac{d\phi}{d\psi} = \pm\frac{1 - b\cos^2\psi}{\sqrt{(b\cos^2\psi + a)(b\cos^2\psi + c)}}. \tag{3.14}$$

Indeed, since the solutions are symmetric and we consider the whole orbit to compute the period, one arrives at

$$T_\phi(c) = 2\int_{-\frac{\pi}{2}+\varepsilon^*}^{\frac{\pi}{2}-\varepsilon^*} \frac{1-b\cos^2\psi}{\sqrt{(b\cos^2\psi+a)(b\cos^2\psi+c)}}d\psi = 2F_{a,b}(-bu,u). \tag{3.15}$$

The last equality in Eq. (3.15) is obtained by performing the change of coordinates that we have used before, $x=\cos^2\psi$ and $c=-bu=-b\sin^2(\varepsilon)$. Lemma 3.16 proves that the period $T_\phi(c)$ decreases when c decreases. In Fig. 3.1, this means that the smaller orbits have a smaller period (ϕ plays the role of time in this phase space). This latter result implies that the sign of $\cos(\theta)$ changes after the intersection point between $\mathcal{C}$ and $\mathcal{S}$, since for the values of c between $-b$ and the value of this intersection point the periods are smaller.

The second implicit equation takes the following form

$$\begin{aligned}\int_{-\pi/2+\varepsilon}^{-\pi/2+\varepsilon^*} -h_{a,b,c}(\psi)\,d\psi + \int_{-\pi/2+\varepsilon^*}^{\pi/2-\varepsilon^*} h_{a,b,c}(\psi)\,d\psi + \int_{\pi/2-\varepsilon^*}^{\pi/2-\varepsilon} -h_{a,b,c}(\psi)\,d\psi \\ =2\pi\end{aligned} \tag{3.16}$$

where $\varepsilon^* \in \left(0,\frac{\pi}{2}\right)$ and

$$h_{a,b,c}(\psi) = \frac{1-b\cos^2\psi}{\sqrt{(a+b\cos^2\psi)(c+b\cos^2\psi)}}. \tag{3.17}$$

Notice that $\varepsilon \in [\varepsilon^*, \pi-\varepsilon^*]$. Hence $\varepsilon^* < \varepsilon$. Straightforward computation leads to the following expressions in terms of $F_{a,b}$

$$2F_{a,b}\left(c,-\frac{c}{b}\right) - F_{a,b}(c,u) = 2\pi, \tag{3.18}$$

for $\varepsilon < \frac{\pi}{2}$ and

$$2F_{a,b}\left(c,-\frac{c}{b}\right) + F_{a,b}(c,u) = 2\pi, \tag{3.19}$$

for $\varepsilon \geq \frac{\pi}{2}$.

After each intersection point between the curves $\mathcal{C}$ and $\mathcal{S}$, the implicit equation describing the curve $\mathcal{C}$ changes as it is explicitly shown in the last part of the following subsection.

3.3 The curve $\mathcal{C}$ in the physical and non-physical cases

In this section, we show that the physical nature of a rigid body can be detected from the structure of the curve $\mathcal{C}$, in the sense that the properties of the curve $\mathcal{C}$ differs between a physical and a non-physical rigid body.

The physical case

The proof of Theorem 3.1 is given at the end of this part. First, we show two results on which the proof of Theorem 3.1 is based.

Lemma 3.7. There exists an intersection point $(c_1, \varepsilon(c_1))$ between $\mathcal{C}$ and $\mathcal{S}$ and a point $\left(c^*, \frac{\pi}{2}\right) \in \mathcal{C}$ such that $c^* \in (c_2, c_1)$, if and only if $\mathcal{I} < 1$. Here c_2 is either the coordinate of the second intersection point or equal to $-b$ if there is no second intersection point.

Proof. Since the point $\left(c^*, \frac{\pi}{2}\right) \in \mathcal{C}$ is found between the first and the second intersection point (in the sense that $c^* \in (c_2, c_1)$), then the implicit equation describing $\mathcal{C}$ in this point is given by Eq. (3.16), leading for $c = c^*$ and $\varepsilon = \frac{\pi}{2}$ to the following expression

$$2\int_{-\pi/2+\varepsilon^*}^{\pi/2-\varepsilon^*} \frac{1 - b\cos^2\psi}{\sqrt{(a + b\cos^2\psi)(c^* + b\cos^2\psi)}} = 2\pi,$$

which is equivalent to

$$F_{a,b}(-bu^*, u^*) = \pi,$$

where $u^* = -\frac{c^*}{b}$. Since the minimum value of $F_{a,b}(-bu, u)$ is $\mathcal{I}\pi$ and $c^* \neq -b$, we arrive at $\pi\mathcal{I} < \pi$ concluding that $\mathcal{I} < 1$.

Conversely, the condition $\frac{1-b}{\sqrt{b(a+b)}} < 1 < 2$ implies the existence of an intersection point on the interval $u \in (0, 1)$ (due to Lemma 3.5), which leads to $-b < c_1$. Let us set $u_1 = -\frac{c_1}{b}$. As a first step, we prove that the condition $\mathcal{I} < 1$ gives the existence of a solution $u^* \in (u_1, 1)$ to the implicit equation $F_{a,b}(-bu, u) = \pi$. Using the same analysis as the one done in Lemma 3.5, we observe that $F_{a,b}(-bu, u)$ is equal to 2π, for u equal to u_1, and goes to $\pi\mathcal{I}$, when u goes to 1. By hypothesis, $\pi\mathcal{I} < \pi$, we conclude that there exists $u^* \in (u_1, 1)$, such that $F_{a,b}(-bu^*, u^*) = \pi$.

Now, we define $c^* = -bu^* < c_1$ and prove that the point $(c, \varepsilon) = \left(c^*, \frac{\pi}{2}\right)$ belongs to $\mathcal{C}$. We consider expression (3.16), since we analyze $\mathcal{C}$ after the

first intersection point.

$$\int_{0}^{-\pi/2+\varepsilon^*} -h_{a,b,c^*}(\psi)\,d\psi + \int_{-\pi/2+\varepsilon^*}^{\pi/2-\varepsilon^*} h_{a,b,c^*}(\psi)\,d\psi + \int_{\pi/2-\varepsilon^*}^{0} -h_{a,b,c^*}(\psi)\,d\psi$$
$$= 2\int_{-\pi/2+\varepsilon^*}^{\pi/2-\varepsilon^*} h_{a,b,c^*}(\psi)\,d\psi.$$

Using the change of coordinates $x = \cos^2\psi$, we get

$$2\int_{-\pi/2+\varepsilon^*}^{\pi/2-\varepsilon^*} h_{a,b,c^*}(\psi)\,d\psi = 2F_{a,b}\left(c^*, \frac{-c^*}{b}\right) = 2F_{a,b}\left(-bu^*, u^*\right) = 2\pi.$$

Thus, $\left(c^*, \frac{\pi}{2}\right)$ belongs to $\mathcal{C}$. Since it is a solution of the second implicit equation, we also get $c^* \in (c_2, c_1)$, where c_2 is either the coordinate of the second intersection point or $-b$, if there is no second intersection point. □

Following the preceding proof, the same result can be established when $c^* = -b$ and $\mathcal{I} = 1$.

Proposition 3.8. The function $\varepsilon(c)$ is not injective if and only if there exists a point $\left(c^*, \frac{\pi}{2}\right) \in \mathcal{C}$, with $c^* \in (-b, 0)$.

Proof. As the function $\varepsilon(c)$ is not injective, there exists an intersection point $(c_1, \varepsilon(c_1))$ between $\mathcal{C}$ and $\mathcal{S}$. This is because we proved that the function $\varepsilon(c)$ is injective in the part described by the first implicit equation. Since we have an intersection point, we analyze Eq. (3.18) and prove that $\varepsilon(c)$ is a strictly decreasing function when it is described by this last equation. Let us consider $c_3 < c_2 < c_1 < 0$. The period $T_\phi(c)$ being decreasing, when c decreases, implies $2F_{a,b}\left(c_3, \frac{-c_3}{b}\right) < 2F_{a,b}\left(c_2, \frac{-c_2}{b}\right)$. Thus, we have

$$2F_{a,b}\left(c_3, \frac{-c_3}{b}\right) - 2\pi < 2F_{a,b}\left(c_2, \frac{-c_2}{b}\right) - 2\pi. \tag{3.20}$$

Using $c_3 < c_2$, we get

$$0 < \frac{1-bx}{\sqrt{x(1-x)\left(1+\frac{b}{a}x\right)\left(x+\frac{c_2}{b}\right)}} < \frac{1-bx}{\sqrt{x(1-x)\left(1+\frac{b}{a}x\right)\left(x+\frac{c_3}{b}\right)}}. \tag{3.21}$$

Thus, if u_2 and u_3 are such that

$$\frac{1}{\sqrt{ab}}\int_{u_2}^{1}\frac{1-bx}{\sqrt{x\left(1-x\right)\left(1+\frac{b}{a}x\right)\left(x+\frac{c_2}{b}\right)}}=2F_{a,b}\left(c_2,\frac{-c_2}{b}\right)-2\pi,$$
$$\frac{1}{\sqrt{ab}}\int_{u_3}^{1}\frac{1-bx}{\sqrt{x\left(1-x\right)\left(1+\frac{b}{a}x\right)\left(x+\frac{c_3}{b}\right)}}=2F_{a,b}\left(c_3,\frac{-c_3}{b}\right)-2\pi.$$

Using Eq. (3.20) and (3.21), we obtain $u_2 < u_3$, which is equivalent to

$$\varepsilon(c_2)=\arcsin\left(\sqrt{u_2}\right)<\varepsilon(c_3)=\arcsin\left(\sqrt{u_3}\right). \tag{3.22}$$

We just have proved that when the function $\varepsilon(c)$ is described by Eq. (3.18), it is a strictly decreasing function. For this reason, $\varepsilon(c)$ is injective in the region where it is described by the first implicit equation and by Eq. (3.18). Since $\varepsilon(c)$ is not injective globally, we conclude that there exists a point $\left(c^*,\frac{\pi}{2}\right)\in\mathcal{C}$, with $c^*\in(-b,0)$.

Conversely, we have that $\varepsilon(c^*)=\frac{\pi}{2}$ and, notice that for the TRE on the separatrix we have $\varepsilon(0)\in\left(0,\frac{\pi}{2}\right)$. Thus, all the values in $[\varepsilon(0),\frac{\pi}{2}]$ are taken by the function $\varepsilon(c)$. If the function $\varepsilon(c)$ is less than $\frac{\pi}{2}$, for values of c in $(-b,c^*)$, then the function is not injective. If it is not the case, then there exist $\delta_1>0$ and $\delta_2>0$ such that

$$\left(\frac{\pi}{2}-\delta_2,\frac{\pi}{2}+\delta_2\right)\subset\varepsilon\left(\left(c^*-\delta_1,c^*+\delta_1\right)\right). \tag{3.23}$$

We also have

$$\varepsilon(c)\in\left[\arcsin\left(\sqrt{\frac{-c}{b}}\right),\pi-\arcsin\left(\sqrt{\frac{-c}{b}}\right)\right]. \tag{3.24}$$

Since $\arcsin\left(\sqrt{\frac{-c}{b}}\right)\to\frac{\pi}{2}$, when $c\to-b$, then there exists $\tilde{c}$ such that $\tilde{c}<c^*-\delta_1$ and close enough to $-b$ so that

$$\left[\arcsin\left(\sqrt{\frac{-\tilde{c}}{b}}\right),\pi-\arcsin\left(\sqrt{\frac{-\tilde{c}}{b}}\right)\right]\subset\left(\frac{\pi}{2}-\delta_2,\frac{\pi}{2}+\delta_2\right). \tag{3.25}$$

Finally, we conclude that $\varepsilon(\tilde{c})\in\left(\frac{\pi}{2}-\delta_2,\frac{\pi}{2}+\delta_2\right)$, *i.e.*, the function $\varepsilon(c)$ is not injective. □

Proof of Theorem 3.1. If the function $\varepsilon(c)$ is not injective, then there exists an intersection point $(c_1,\varepsilon(c_1))$ between $\mathcal{C}$ and $\mathcal{S}$ and a point $\left(c^*,\frac{\pi}{2}\right)\in\mathcal{C}$,

where $c^* \in (-b, c_1)$. This is a consequence of the proof of Proposition 3.8. Using Lemma 3.7, we obtain that $\mathcal{I} < 1$. Conversely, if $\mathcal{I} < 1$, using Lemma 3.7, we deduce that there exists an intersection point $(c_1, \varepsilon(c_1))$ between $\mathcal{C}$ and $\mathcal{S}$ and a point $\left(c^*, \frac{\pi}{2}\right) \in \mathcal{C}$, where $c^* \in (-b, c_1)$, which implies that the function $\varepsilon(c)$ is not injective (due to Proposition 3.8). The first claim follows.

The second claim now follows directly from Proposition 1.3. □

The curve $\mathcal{C}$ in the non-physical case

Theorem 3.1 shows that for physical rigid bodies, the curve $\mathcal{C}$ is described by an injective decreasing function, while, for non-physical systems, this function is non-injective. In this latter case, the function has an oscillating behavior with respect to the curve $\mathcal{S}$, i.e. the curves $\mathcal{C}$ and $\mathcal{S}$ intersect several times. Moreover, the number of intersection points depends on the value of the geometric constant $\mathcal{I}$. Fig. 3.3 illustrates these different behaviors.

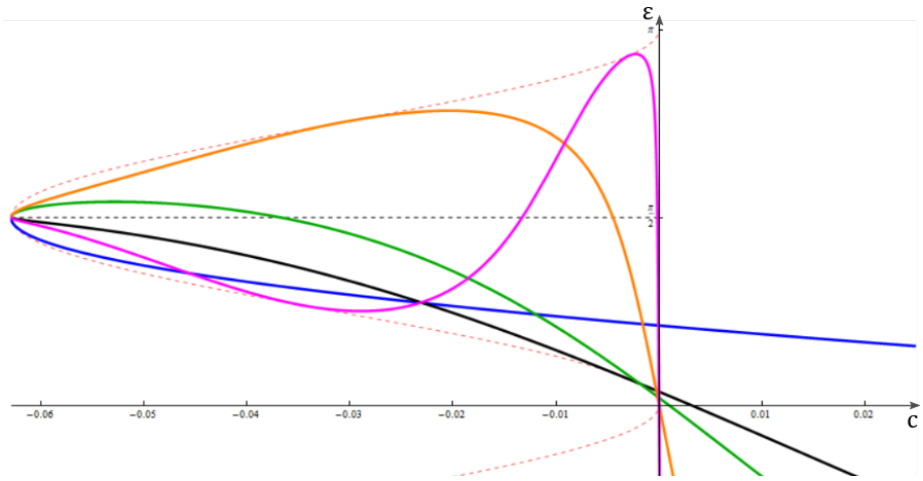

Figure 3.3: Representation of the oscillatory behavior observed, in the non-physical case, with respect to the curve $\mathcal{S}$ which is represented by the red dashed curve.

The following Theorem is the main result for the non-physical case and states the aforementioned structure of the curve $\mathcal{C}$.

Theorem 3.9. For every $n \in \mathbb{N} \setminus \{0\}$, if the parameters a and b are such that $\mathcal{I} < \frac{2}{2n+1}$, then there exist at least n intersection points between $\mathcal{C}$ and $\mathcal{S}$. Moreover, if $(c_n, \varepsilon(c_n))$ are the coordinates of the n-th intersection point,

then there exist $c^* \in (-b, c_n)$ such that $\varepsilon(c^*) = \frac{\pi}{2}$ and another intersection point $(c_{int}, \varepsilon(c_{int}))$ such that $c_{int} \in (-b, c_n)$.

The proof generalizes the ideas used in the preceding Lemmas and is given at the end of this part of the text. We start by introducing the generalization of the implicit equations describing the curve $\mathcal{C}$.

The same derivation as the one used for the second implicit equation can be done after each intersection point between $\mathcal{C}$ and $\mathcal{S}$, since the period $T_\phi(c)$ is a decreasing function. We deduce that the implicit equation describing $\mathcal{C}$ depends on the number of intersection points.

After the first n intersection points, the implicit equation that describes $\mathcal{C}$ is

$$\begin{aligned} 2\pi = &\int_{-\pi/2+\varepsilon}^{-\pi/2+\varepsilon^*} -h_{a,b,c}(\psi)\, d\psi + (2n-1)\int_{-\pi/2+\varepsilon^*}^{\pi/2-\varepsilon^*} h_{a,b,c}(\psi)\, d\psi \\ &+ \int_{\pi/2-\varepsilon^*}^{\pi/2-\varepsilon} -h_{a,b,c}(\psi)\, d\psi, \end{aligned} \tag{3.26}$$

for n odd and

$$\begin{aligned} 2\pi = &\int_{-\pi/2+\varepsilon}^{\pi/2-\varepsilon^*} h_{a,b,c}(\psi)\, d\psi + (2n-1)\int_{-\pi/2+\varepsilon^*}^{\pi/2-\varepsilon^*} h_{a,b,c}(\psi)\, d\psi \\ &+ \int_{-\pi/2+\varepsilon^*}^{\pi/2-\varepsilon} h_{a,b,c}(\psi)\, d\psi, \end{aligned} \tag{3.27}$$

for n even. Using $x = \cos^2\psi$, we get four different expressions

$$2nF_{a,b}\left(c, -\frac{c}{b}\right) - F_{a,b}(c,u) = 2\pi,\ n \text{ odd},\ \varepsilon < \frac{\pi}{2} \tag{3.28}$$

$$2nF_{a,b}\left(c, -\frac{c}{b}\right) + F_{a,b}(c,u) = 2\pi,\ n \text{ odd},\ \varepsilon \geq \frac{\pi}{2} \tag{3.29}$$

$$2nF_{a,b}\left(c, -\frac{c}{b}\right) - F_{a,b}(c,u) = 2\pi,\ n \text{ even},\ \varepsilon > \frac{\pi}{2} \tag{3.30}$$

$$2nF_{a,b}\left(c, -\frac{c}{b}\right) + F_{a,b}(c,u) = 2\pi,\ n \text{ even},\ \varepsilon \leq \frac{\pi}{2} \tag{3.31}$$

Lemma 3.10. Assume that the parameters a and b are such that $\mathcal{I} < \frac{2}{3}$. Let $(c_1, \varepsilon(c_1))$ be the coordinates of the first intersection point between $\mathcal{C}$ and $\mathcal{S}$. Then, there exists an intersection point $(c_{int}, \varepsilon(c_{int}))$ such that $c_{int} \in (-b, c_1)$.

Proof. First notice that the condition $\mathcal{I} < \frac{2}{3} < 2$ implies the existence of an intersection point on the interval $\varepsilon \in \left(0, \frac{\pi}{2}\right)$, due to Lemma 3.5, which

gives $-b < c_1$. Then, we stress that $\mathcal{I} < \frac{2}{3} < 1$ leads to the existence of a point $c^* \in (-b, c_1)$, such that $\varepsilon(c^*) = \frac{\pi}{2}$.

If there exists another intersection point between c^* and c_1, the proof is done. If not, then we look for one after c^*, i.e., on the interval $(-b, c^*)$. For this reason we use the expression (3.29), for $n = 1$

$$2F_{a,b}\left(c, -\frac{c}{b}\right) + F_{a,b}(c, u) = 2\pi. \tag{3.32}$$

We analyze this equation along the curve $c = -bu$ to find intersection points, getting

$$2\pi = 2F_{a,b}(-bu, u) + F_{a,b}(-bu, u) = 3F_{a,b}(-bu, u). \tag{3.33}$$

Thus, our problem is equivalent to the problem of finding solutions to the implicit equation given by

$$F_{a,b}(-bu, u) = \frac{2\pi}{3}. \tag{3.34}$$

Using the same techniques as before, we notice that $F_{a,b}(-bu, u)$ is equal to π, for $u^* = \frac{c^*}{-b}$ and goes to $\mathcal{I}\pi < \frac{2}{3}\pi$, when u goes to 1. We deduce that there exists $u_{int} \in (u^*, 1)$ such that $F_{a,b}(-bu, u)$ is equal to $\frac{2\pi}{3}$. Then the point (c_{int}, u_{int}), where $c_{int} = -bu_{int}$, is an intersection point such that $-b < c_{int} < c^* < c_1$. □

Proof of Th. 3.9. We proceed by induction

- Base case. For $n = 1$, we get the condition $\mathcal{I} < \frac{2}{3} < 1 < 2$. Using Lemma 3.5, we have the existence of at least one intersection point. Using Lemma 3.7 and Lemma 3.10, we have respectively the existence of c^* and of the intersection point $(c_{int}, \varepsilon(c_{int}))$.

- Induction step. Assuming that the statement holds for $n > 1$, we prove that it holds for $n + 1$. The condition $\mathcal{I} < \frac{2}{2(n+1)+1} < \frac{2}{2n+1}$ implies the existence of at least $n+1$ intersection points (the statement holds for n). Let $(c_{n+1}, \varepsilon(c_{n+1}))$ be the coordinates of the $(n+1)$-st intersection point and $u_n + 1 = -\frac{c_{n+1}}{b}$. Notice that $-b < c_{n+1}$ and, hence, $u_{n+1} < 1$ (the statement holds for n).

  First, we prove that the condition $\mathcal{I} < \frac{2}{2(n+1)+1} < \frac{1}{n+1}$ implies the existence of a solution $u^* \in (u_{n+1}, 1)$ to the implicit equation given by $F_{a,b}(-bu, u) = \frac{\pi}{n+1}$. Using the same analysis as the one done in Lemma 3.5, we observe that $F_{a,b}(-bu, u)$ is equal to $\frac{2\pi}{2n+1}$, for u equal

to u_{n+1}, and goes to $\mathcal{I}\pi$, when u goes to 1. Using the hypothesis, we get

$$\mathcal{I}\pi < \frac{\pi}{n+1} < \frac{2\pi}{2n+1}. \tag{3.35}$$

We conclude that there exists $u^* \in (u_{n+1}, 1)$ fulfilling the equation $F_{a,b}(-bu^*, u^*) = \frac{\pi}{n+1}$. Now, we define $-b < c^* = -bu^* < c_{n+1}$ and we show that the point $(c, \varepsilon) = \left(c^*, \frac{\pi}{2}\right)$ belongs to $\mathcal{C}$. We study the set $\mathcal{C}$ after the first $n+1$ intersection points and we observe that Eq. (3.26) and (3.27) transform into

$$2(n+1) \int_{-\pi/2+\varepsilon^*}^{\pi/2-\varepsilon^*} h_{a,b,c^*}(\psi)\, d\psi, \tag{3.36}$$

for the point $\left(c^*, \frac{\pi}{2}\right)$. Using the change of coordinates $x = \cos^2\psi$, we get

$$\begin{aligned} 2(n+1) \int_{-\pi/2+\varepsilon^*}^{\pi/2-\varepsilon^*} h_{a,b,c^*}(\psi)\, d\psi &= 2(n+1) F_{a,b}\left(c^*, \frac{-c^*}{b}\right) \\ &= 2(n+1) F_{a,b}(-bu^*, u^*) \\ &= 2\pi. \end{aligned} \tag{3.37}$$

Thus, $\left(c^*, \frac{\pi}{2}\right)$ belongs to $\mathcal{C}$, which implies that $\varepsilon(c^*) = \frac{\pi}{2}$.

Finally, we prove the existence of the intersection point $(c_{int}, \varepsilon(c_{int}))$. If there exists another intersection point between c^* and c_{n+1}, the proof is done. If not, then we look for one after c^*, i.e., on the interval $(-b, c^*)$. For this reason, we use the implicit equation (3.29), or (3.31), along the curve $c = -bu$. Both equations transform into

$$2\pi = 2(n+1)F_{a,b}(-bu, u) + F_{a,b}(-bu, u) = (2(n+1)+1)F_{a,b}(-bu, u). \tag{3.38}$$

Thus, our problem is equivalent to the problem of finding solutions to the implicit equation given by

$$F_{a,b}(-bu, u) = \frac{2\pi}{2(n+1)+1}. \tag{3.39}$$

Using the same techniques as before, we notice that $F_{a,b}(-bu, u)$ is equal to $\frac{\pi}{n+1}$, for $u^* = \frac{c^*}{-b}$ and goes to $\frac{1-b}{\sqrt{b(a+b)}}\pi$, when u goes to 1. We get

$$\frac{1-b}{\sqrt{b(a+b)}}\pi < \frac{2\pi}{2(n+1)+1} < \frac{\pi}{n+1}. \tag{3.40}$$

We conclude that there exists $u_{int} \in (u^*, 1)$, such that $F_{a,b}(-bu, u)$ is equal to $\frac{2\pi}{2(n+1)+1}$. Then, the point (c_{int}, u_{int}), where $c_{int} = -bu_{int}$, is an intersection point such that $-b < c_{int} < c^* < c_{n+1}$.

□

Numerical calculations show the different behaviors in Fig. 3.4.

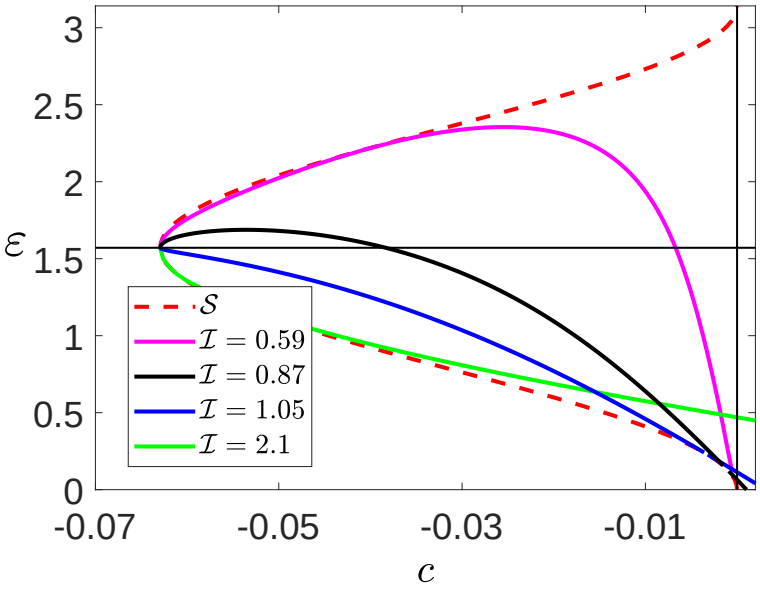

Figure 3.4: Plot of the function $\varepsilon(c)$. We have used a fixed value of $b = 0.0629$ and varied the value of a. The solid purple, black, blue, and green curves correspond respectively to $a = 39.95, a = 18.27$, $a = 12.65$ and $a = 3.1$, which leads to $\mathcal{I} = 0.59$, 0.87, 1.05 and 2.1. The dashed red curve represents the set $\mathcal{S}$. The black horizontal and vertical lines have the equations $\varepsilon = \pi/2$ and $c = 0$, respectively.

3.4 Global behavior of the tennis racket effect with respect to the geometric parameters a and b

Once the analysis of the curve $\mathcal{C}$ has been done for a fixed rigid body (for a and b fixed), the next step is to analyze the behavior of this curve when the parameters a and b vary. In this part of the text we study two particular cases of this problem.

Evolution of c_0 and ε_0 as a function of a

Recall that c_0 and ε_0, introduced in Proposition 3.4, represent respectively a perfect TRE and the TRE on the separatrix. In this section, we prove that the values of $c_0(a,b)$ and $\varepsilon_0(a,b)$ decrease when a increases. This result allows to analyze the behavior of $\mathcal{C}$ when the parameter a varies. Since we consider different values of (a,b), in this section we use the notation $\mathcal{C}_{a,b}$ instead of $\mathcal{C}$.

Lemma 3.11. Let us consider two values of the parameter a such that $0 < a_1 < a_2$ and the solutions $(0, c_0(a_1)) \in \mathcal{C}_{a_1,b}$, $(0, c_0(a_2)) \in \mathcal{C}_{a_2,b}$. Then $c_0(a_1) > c_0(a_2)$.

Proof. We have that $(0, c_0(a_1)) \in \mathcal{C}_{a_1,b}$ and $(0, c_0(a_2)) \in \mathcal{C}_{a_2,b}$. Thus

$$\begin{aligned}\pi &= \int_0^{\pi/2} \frac{1 - b\cos^2\psi}{\sqrt{(b\cos^2\psi + a_1)(b\cos^2\psi + c_0(a_1))}} d\psi \\ &= \int_0^{\pi/2} \frac{1 - b\cos^2\psi}{\sqrt{(b\cos^2\psi + a_2)(b\cos^2\psi + c_0(a_2))}} d\psi. \end{aligned} \tag{3.41}$$

Since $a_1 < a_2$, then $\sqrt{b\cos^2\psi + a_1} < \sqrt{b\cos^2\psi + a_2}$. This latter inequality implies

$$\frac{1 - b\cos^2\psi}{\sqrt{b\cos^2\psi + a_2}} < \frac{1 - b\cos^2\psi}{\sqrt{b\cos^2\psi + a_1}}. \tag{3.42}$$

From the two previous equations, we obtain

$$\frac{1}{\sqrt{b\cos^2\psi + c_0(a_2)}} > \frac{1}{\sqrt{b\cos^2\psi + c_0(a_1)}}, \tag{3.43}$$

which leads to

$$c_0(a_1) > c_0(a_2). \tag{3.44}$$

□

Lemma 3.12. Let us consider two values of the parameter a such that $0 < a_1 < a_2$ and the solutions $(\varepsilon_0(a_1), 0) \in \mathcal{C}_{a_1,b}$, $(\varepsilon_0(a_2), 0) \in \mathcal{C}_{a_2,b}$. Then $\varepsilon_0(a_1) > \varepsilon_0(a_2)$.

Proof. We follow the same idea as in the previous proof. The fact that $(\varepsilon_0(a_1), 0) \in \mathcal{C}_{a_1,b}$ and $(\varepsilon_0(a_2), 0) \in \mathcal{C}_{a_2,b}$ leads to

$$\begin{aligned}\pi &= \int_0^{\pi/2-\varepsilon_0(a_1)} \frac{1-b\cos^2\psi}{\sqrt{(b\cos^2\psi+a_1)\,b\cos^2\psi}}d\psi \\ &= \int_0^{\pi/2-\varepsilon_0(a_2)} \frac{1-b\cos^2\psi}{\sqrt{(b\cos^2\psi+a_2)\,b\cos^2\psi}}d\psi. \end{aligned} \tag{3.45}$$

Since $a_1 < a_2$, then $\sqrt{(b\cos^2\psi+a_1)\,b\cos^2\psi} < \sqrt{(b\cos^2\psi+a_2)\,b\cos^2\psi}$, giving

$$\frac{1-b\cos^2\psi}{\sqrt{(b\cos^2\psi+a_2)\,b\cos^2\psi}} < \frac{1-b\cos^2\psi}{\sqrt{(b\cos^2\psi+a_1)\,b\cos^2\psi}}. \tag{3.46}$$

From the two previous equations, we get

$$\frac{\pi}{2} - \varepsilon_0(a_1) < \frac{\pi}{2} - \varepsilon_0(a_2). \tag{3.47}$$

We conclude that $\varepsilon_0(a_1) > \varepsilon_0(a_2)$. □

Notice that, when we change the value of a, but not the value of b we have the same limit curve $\mathcal{S}_b$ that cannot be crossed, but the set $\mathcal{C}_{a,b}$ is modified. According to these results, we know that when the value of a increases the curve $\mathcal{C}_{a,b}$ goes down, in the sense that its intersection points with the two axes decrease (See Figs. 3.2 and 3.5). An illustrative numerical example is given in Fig. 3.5 for physical and non-physical rigid bodies. We observe that the evolution of ε as a function of c is similar in the two cases. When a goes to ∞ for a fixed value of b, the curve $\mathcal{C}$ is tangent to $\mathcal{S}$ in $c = \varepsilon = 0$. This limit case has been already described in the previous Chapter, obtaining that we have a perfect tennis racket effect on the separatrix.

Remark 3.13. From this analysis, one observes that the only possibility to have a perfect TRE on the separatrix is to consider the abstract limit $a \to \infty$. This case has been already described in the previous chapter in Theorem 6.1. Moreover, as explained in Sec. 1.4, the physical constraint corresponds to $2b + ab \leq 1$. If this inequality is fulfilled when $a \to \infty$, then $b \to 0$. This case ($a \to \infty$, $b \to 0$) is described below. Note that when $a \to \infty$ and $b \to 0$, the physical constraint becomes $ab \leq 1$.

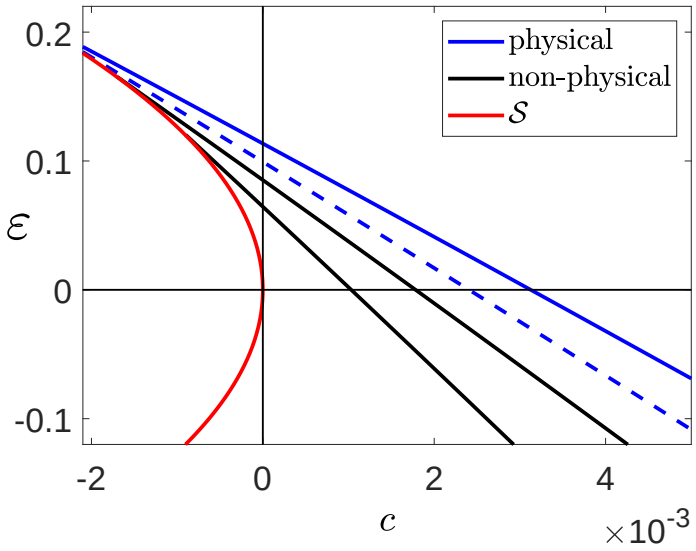

Figure 3.5: Plot of the defect ε as a function of c (curve $\mathcal{C}_{a,b}$) for different values of a, the parameter b being fixed to 0.06. The parameter a is respectively set to 12.65, 13.89, 15.38 and 18.27 (solid blue, dashed blue and solid black lines), which leads to $\mathcal{I}$ equal to 1.045, 1, 0.951 and 0.872. The horizontal and vertical solid lines indicate respectively the position of a perfect TRE ($\varepsilon = 0$) and of the separatrix ($c = 0$). The set $\mathcal{S}$ is plotted in red.

Behavior of the flip defect ε when $a \to \infty$ and $b \to 0$

In [36], an explicit expression for the flip defect ε is obtained in the limit case $a \to \infty$ and $b \to 0$ by using incomplete elliptic integrals.

The parameters χ and β defined as follows

$$\chi = ab, \qquad \beta = \frac{c}{b}, \tag{3.48}$$

are introduced and the expression obtained is

$$\varepsilon = \frac{\pi}{2} - \mathrm{am}\left(\pi\sqrt{\chi(1+\beta)}\middle|\frac{1}{1+\beta}\right), \tag{3.49}$$

where am is the Jacobi amplitude. Recall that the Jacobi amplitude is defined as the inverse of the incomplete elliptic integral of the first kind, i.e. if $u = F(\varphi|m)$, then $\varphi = \mathrm{am}(u|m)$.

According to Lemma 3.12, we know that the value of the flip defect on the separatrix ε_0 decreases when a increases, and so the smallest possible

value of ε_0 will occur when $a \to \infty$. Therefore, we can use expression (3.49) to determine the minimum value of ε_0 subject to the physical constraint $\chi \leq 1$. It turns out that in the case of $c < 0$, there is a minimum value for ε when $\chi \to 1$ and $\beta \to 0$. In this limit case, we have

$$\varepsilon_{0,min} = \frac{\pi}{2} - \text{am}\,(\pi|1) = \pi - 2\arctan\left(e^{\pi}\right) = 0.086374. \tag{3.50}$$

While in the case $c > 0$, there is a minimum value of $\beta \neq 0$ such that $\varepsilon = 0$ that happens when $\chi \to 1$, namely

$$\frac{\pi}{2} - \text{am}\left(\pi\sqrt{1+\beta}\middle|\frac{1}{1+\beta}\right) = 0 \quad \Rightarrow \quad \beta = 0.028973. \tag{3.51}$$

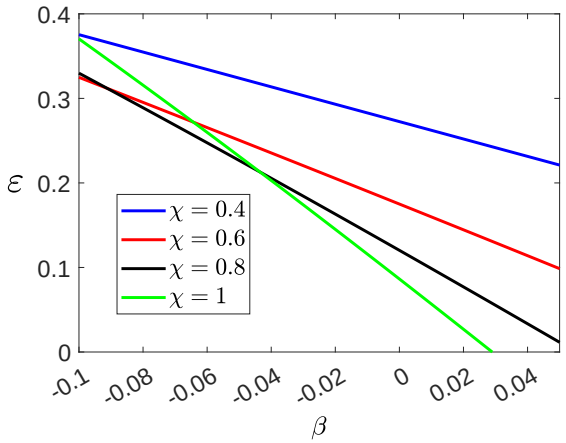

Figure 3.6: Plot of the function $\varepsilon = \frac{\pi}{2} - \text{am}\left(\pi\sqrt{\chi\,(1+\beta)}\middle|\frac{1}{1+\beta}\right)$. The values of $\chi = 1$, 0.8, 0.6 and $\chi = 0.4$ correspond to the green, black, red and blue curves respectively.

Figure 3.6 illustrates the analysis carried out above. For instance, we observe that when we are very close to the separatrix $\beta = 0$, there is no physical rigid body (in the sense that $\chi \leq 1$) that can achieve a perfect $\Delta\psi = \pi$ twist (i.e., $\varepsilon_0 = 0$). Nevertheless, we observe that when $\beta = 0$, the smallest possible value of ε_0 happens for $\chi \to 1$, and therefore such a physical rigid body characterized by $\chi = 1$ performs the best quasi-perfect twist, $\Delta\psi = \pi - 2\varepsilon_{0,min} = 2.96884$, on the separatrix.

3.5 The Montgomery phase

The Montgomery phase is a geometric phase that can be seen, for rotational dynamics, as the analog of the Berry phase for quantum systems [51, 17]. We now introduce this concept.

As shown in figure 1.6, the solutions to Euler's equations are periodic functions (except for the fixed points and the separatrix). For a periodic solution, after one period T, the angular momentum vector $\vec{J}$ as seen in the rotating rigid body frame has returned to the initial position. In the laboratory frame, the rigid body has rotated by some angle around $\vec{J}$ with respect to its initial orientation. The Montgomery phase is this angle of rotation.

In our convention for the Euler's angles, for one period, the angle that measures the rotation around $\vec{J}$ is given by $\Delta\phi$.

Montgomery's formula [52] gives this angle as

$$\Delta\phi = \frac{2HT}{J} - \frac{A}{J} \tag{3.52}$$

where H is the energy and A is the area of the region bounded by the orbit on the angular momentum sphere as represented in Fig. 3.7 (the sign is chosen according to whether or not the orientation of the periodic orbit is induced by the standard orientation of this region). The first term is usually called dynamical phase and the second one geometric phase.

We study in this section the signature of the physical constraint introduced in Proposition 1.3 on the Montgomery phase. Different analytical properties described by Theorems 3.14 and 3.15 are found for oscillating and rotating trajectories.

Theorem 3.14.

1. For any $(a, b) \in (0, \infty) \times (0, 1)$, the greatest lower bound or infimum, $\inf_{c\in(-b,0)} \Delta\phi\,(a, b)$, of the Montgomery phase $\Delta\phi$, for oscillating trajectories, is given by

$$\inf_{c\in(-b,0)} \Delta\phi\,(a, b) = 2\pi\mathcal{I},$$

   where $\mathcal{I} = \mathcal{I}\,(a, b)$ is the geometric constant given by (1.14).

2. A rigid body is physical (i.e. such that $\mathcal{I} \geq 1$), if and only if

$$\inf_{c\in(-b,0)} \Delta\phi\,(a, b) \geq 2\pi.$$

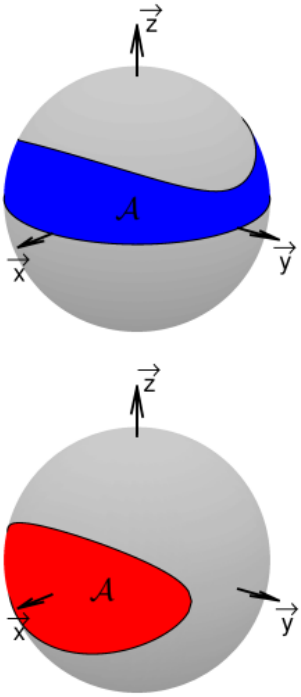

Figure 3.7: Representation of the area A of the geometric phase corresponding to the rotating and oscillating trajectories (top and bottom respectively).

Theorem 3.15. For any $(a,b) \in (0,\infty) \times (0,1)$, the greatest lower bound $\inf_{c\in(0,a)} \Delta\phi\,(a,b)$ of the Montgomery phase $\Delta\phi\,(a,b)$, for rotating trajectories is given by

$$\inf_{c\in(0,a)} \Delta\phi\,(a,b) = 2\pi\mathcal{J},$$

where $\mathcal{J} = \mathcal{J}\,(a,b)$ is the second geometric constant given by (1.14).

The corresponding proofs are given below. We observe that Theorem 3.14 gives a direct way to detect the physical nature of the rigid body. The evolution of $\Delta\phi$ with respect to c in the oscillating and rotating cases is presented in Fig. 3.8 for two generic pairs (a,b) corresponding to a physical and a non-physical rigid body.

The function $F_{a,b}(-bu,u)$

In this subsection, we prove the properties of the function $F_{a,b}(-bu,u)$ that are used to study the case of rotating and oscillating trajectories.

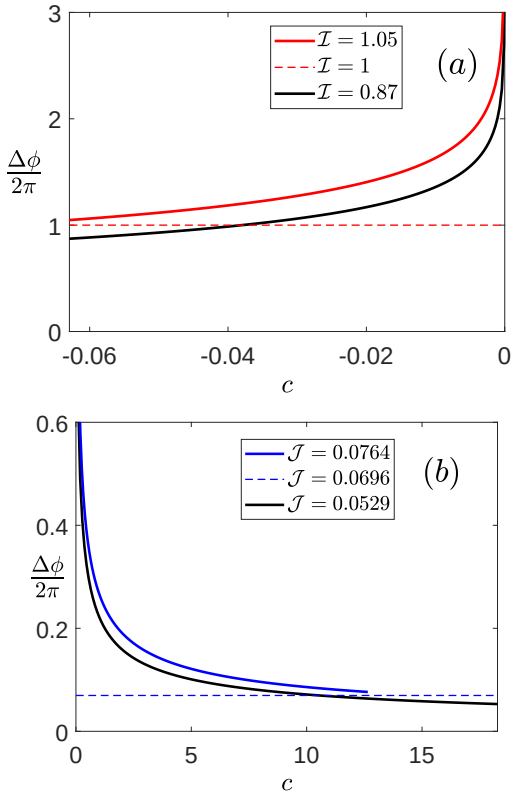

Figure 3.8: Plot of the Montgomery phase $\Delta\phi$ as a function of the parameter c, for oscillating (panel (a)) and rotating (panel (b)) trajectories. A physical and a non-physical rigid body is considered with the parameters $(a = 12.65, b = 0.0629)$ and $(a = 18.27, b = 0.0629)$ respectively. The parameter c belongs to the interval $(-b, a)$. The physical and non-physical cases are depicted respectively in red, blue, or black. The horizontal dashed line represents the boundary between the physical and the non-physical bodies. The small inserts give the corresponding values of $\mathcal{I}$ and $\mathcal{J}$.

Lemma 3.16. The function $F_{a,b}(-bu, u)$ is a decreasing function on the interval $[0, 1]$, and thus, its minimum value is taken in $u = 1$.

Proof. Recall that the function $F_{a,b}(-bu, u)$ has been defined as

$$F_{a,b}(-bu, u) = \frac{1}{\sqrt{ab}} \int_u^1 \frac{1 - bx}{\sqrt{x\,(1-x)\left(1 + \frac{b}{a}x\right)(x-u)}} dx. \tag{3.53}$$

Let us perform the following change of variables

$$x = u + (1-u)\, y^2, \tag{3.54}$$

so for $x \in (u, 1)$, in terms of y, we have $y \in (0, 1)$. Therefore the integral (3.53) can be written as

$$F_{a,b}\left(-bu, u\right) = \frac{2}{\sqrt{ab}} \int_0^1 \frac{1 - b\left(u + (1-u)\, y^2\right)}{\sqrt{\left(1-y^2\right)\left(u + (1-u)\, y^2\right)\left(1 + \frac{b(u+(1-u)y^2)}{a}\right)}} dy. \tag{3.55}$$

Since now the limits of integration (3.55) do not depend on the variable u, to compute the derivative $\partial_u F_{a,b}\left(-bu, u\right)$, we simply perform the following computation

$$\begin{aligned}
&\partial_u F_{a,b}\left(-bu, u\right) \\
&= \frac{2}{\sqrt{ab}} \int_0^1 \partial_u \left[\frac{1 - b\left(u + (1-u)\, y^2\right)}{\sqrt{\left(1-y^2\right)\left(u + (1-u)\, y^2\right)\left(1 + \frac{b(u+(1-u)y^2)}{a}\right)}} \right] dy \\
&= -\frac{b}{(ab)^{3/2}} \int_0^1 \frac{\sqrt{1-y^2}\left(a + (a+2)\, b\left(u + (1-u)\, y^2\right)\right)}{\left(\left(u + (1-u)\, y^2\right)\left(1 + \frac{b(u+(1-u)y^2)}{a}\right)\right)^{3/2}} dy.
\end{aligned} \tag{3.56}$$

Note that we have an explicit minus sign on the right-hand side of Eq. (3.56), and since all the quantities inside the integrand are positive, we conclude that the derivative $\partial_u F_{a,b}\left(-bu, u\right)$ is always negative. This implies that the function $F_{a,b}\left(-bu, u\right)$ is an injective decreasing function on the interval $u \in [0, 1]$, and so its global minimum corresponds to the point where $u \to 1$. □

Lemma 3.17. The function $F_{a,b}\left(-bu, u\right)$ has the following limiting behaviors

$$\lim_{u \to 0} F_{a,b}\left(-bu, u\right) = \infty, \tag{3.57}$$

$$\lim_{u \to 1} F_{a,b}\left(-bu, u\right) = \frac{1-b}{\sqrt{b\,(a+b)}}\pi = \mathcal{I}\pi. \tag{3.58}$$

Proof. Given the expression Eq. (3.53) of the function $F_{a,b}\left(-bu, u\right)$, it is straightforward to deduce that this function diverges when $u \to 0$. The second statement of the Lemma can be shown as follows. When u is close

to one, the function $F_{a,b}(-bu,u)$ can be approximated as follows

$$\begin{aligned} F_{a,b}(-bu,u) =& \frac{1}{\sqrt{ab}}\int_u^1 \frac{1-bx}{\sqrt{x(1-x)\left(1+\frac{b}{a}x\right)(x-u)}}dx \\ \sim& \frac{1-b}{\sqrt{ab\left(1+\frac{b}{a}\right)}}\int_u^1 \frac{1}{\sqrt{(1-x)(x-u)}}dx. \end{aligned} \tag{3.59}$$

By computing the second integral, we obtain

$$\frac{1-b}{\sqrt{ab\left(1+\frac{b}{a}\right)}}\int_u^1 \frac{1}{\sqrt{(1-x)(x-u)}}dx = \frac{1-b}{\sqrt{ab\left(1+\frac{b}{a}\right)}}\pi. \tag{3.60}$$

Then we estimate the error $\mathcal{E}$ of this approximation

$$\begin{aligned} |\mathcal{E}| =& \left| \frac{1}{\sqrt{ab}}\int_u^1 \frac{1-bx}{\sqrt{x(1-x)\left(1+\frac{b}{a}x\right)(x-u)}}dx \right. \\ & \left. - \frac{1-b}{\sqrt{ab\left(1+\frac{b}{a}\right)}}\int_u^1 \frac{1}{\sqrt{(1-x)(x-u)}}dx \right| \\ =& \frac{1-b}{\sqrt{ab\left(1+\frac{b}{a}\right)}}\left| \int_u^1 \frac{1}{\sqrt{(1-x)(x-u)}}\left(\frac{(1-bx)\sqrt{1+\frac{b}{a}}}{(1-b)\sqrt{x\left(1+\frac{b}{a}x\right)}} - 1 \right) dx \right| \\ \leq& \frac{1-b}{\sqrt{ab\left(1+\frac{b}{a}\right)}}\int_u^1 \frac{dx}{\sqrt{(1-x)(x-u)}} \max_{x\in[u,1]} \left| \frac{(1-bx)\sqrt{1+\frac{b}{a}}}{(1-b)\sqrt{x\left(1+\frac{b}{a}x\right)}} - 1 \right| \\ =& \frac{1-b}{\sqrt{ab\left(1+\frac{b}{a}\right)}}\pi \max_{x\in[u,1]} \left| \frac{(1-bx)\sqrt{1+\frac{b}{a}} - (1-b)\sqrt{x\left(1+\frac{b}{a}x\right)}}{(1-b)\sqrt{x\left(1+\frac{b}{a}x\right)}} \right|, \end{aligned}$$

and we get that $|\mathcal{E}| \to 0$, when $u \to 1$.

Using this result and Eq. (3.60), we get

$$F_{a,b}(-bu,u) \to \frac{1-b}{\sqrt{ab\left(1+\frac{b}{a}\right)}}\pi, \tag{3.61}$$

when $u \to 1$. □

The case of oscillating trajectories

The MP is defined as the variation of the angle ϕ for a loop in the reduced phase space $\left(\psi, \frac{d\psi}{d\phi}\right)$ as shown in Fig. 3.9. For the oscillating trajectories, the condition $c + b\cos^2\psi \geq 0$ bounds the evolution of ψ and leads to $\sin^2\varepsilon \geq \frac{|c|}{b}$. We denote by $\varepsilon^* = \arcsin\sqrt{\frac{-c}{b}}$ this minimal value.

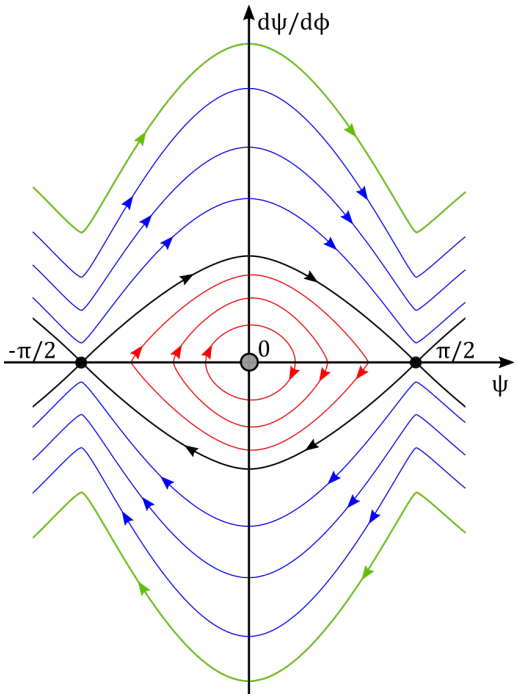

Figure 3.9: Reduced phase space $\left(\psi, \frac{d\psi}{d\phi}\right)$. In this subsection, we analyze oscillating trajectories, which are the red trajectories on this figure.

Using the symmetry of the trajectory with respect to $\frac{d\psi}{d\phi} = 0$, the variation $\Delta\phi$ can be expressed as

$$\Delta\phi = 2\int_{-\frac{\pi}{2}+\varepsilon^*}^{\frac{\pi}{2}-\varepsilon^*} \frac{1 - b\cos^2\psi}{\sqrt{(a + b\cos^2\psi)\,(c + b\cos^2\psi)}} d\psi. \tag{3.62}$$

Proof of Theorem 3.14. The integral (3.62) is also symmetric with respect to the line defined by $\psi = 0$, so that

$$\Delta\phi = 4\int_{0}^{\frac{\pi}{2}-\arcsin\left(\sqrt{\frac{-c}{b}}\right)} \frac{1 - b\cos^2\psi}{\sqrt{(a + b\cos^2\psi)\,(c + b\cos^2\psi)}} d\psi. \tag{3.63}$$

Performing the change of variables $x = \cos^2\psi$, we get

$$\Delta\phi = \frac{2}{\sqrt{ab}} \int_{-c/b}^{1} \frac{1-bx}{\sqrt{x\,(1-x)\left(1+\frac{b}{a}x\right)\left(x+\frac{c}{b}\right)}} dx. \tag{3.64}$$

Introducing $u = -c/b$, so that for $c \in (-b, 0)$, $u \in (0, 1)$, we get

$$\Delta\phi = 2F_{a,b}\left(-bu, u\right), \tag{3.65}$$

where the function $F_{a,b}\left(-bu, u\right)$ described in the previous Subsection is the incomplete elliptic integral

$$F_{a,b}\left(-bu, u\right) = \frac{1}{\sqrt{ab}} \int_{u}^{1} \frac{1-bx}{\sqrt{x\,(1-x)\left(1+\frac{b}{a}x\right)(x-u)}} dx. \tag{3.66}$$

According to Lemma 3.16 of 3.5, giving the monotonic behavior of the function $F_{a,b}\left(-bu, u\right)$, we know that the greatest lower bound of the function $F_{a,b}\left(-bu, u\right)$ occurs when $u \to 1$, which is computed in Lemma 3.17, namely

$$\lim_{u\to 1} F_{a,b}\left(-bu, u\right) = \frac{1-b}{\sqrt{b\,(a+b)}}\pi = \pi\mathcal{I}, \tag{3.67}$$

thus showing the first claim. It is then straightforward to show the second statement. □

The case of rotating trajectories

For rotating trajectories, the angular momentum performs a loop when the angle ψ goes from $-\frac{\pi}{2}$ to $\frac{3\pi}{2}$. Using the symmetries of $\cos^2\psi$, we obtain that the corresponding variation of ϕ is given by

$$\Delta\phi = 4\int_{0}^{\frac{\pi}{2}} \frac{1-b\cos^2\psi}{\sqrt{(a+b\cos^2\psi)\,(c+b\cos^2\psi)}} d\psi. \tag{3.68}$$

Proof of Theorem 3.15. The proof follows the same general lines as the proof of Th. 3.14. One shows that the function $c \mapsto \Delta\phi\,(c)$ is decreasing. Thus, the greatest lower bound is obtained for $c \to a$, since $0 \le c < a$. We obtain by direct calculations,

$$\begin{aligned}\lim_{c\to a}\Delta\phi &= 4\int_{0}^{\frac{\pi}{2}} \frac{1-b\cos^2\psi}{a+b\cos^2\psi} d\psi = 4\int_{0}^{\frac{\pi}{2}} \left[\frac{1+a}{a+b\cos^2\psi} - 1\right] d\psi \\ &= 2\pi\left[\frac{a+1}{\sqrt{a\,(a+b)}} - 1\right] = 2\pi\mathcal{J}.\end{aligned} \tag{3.69}$$

□

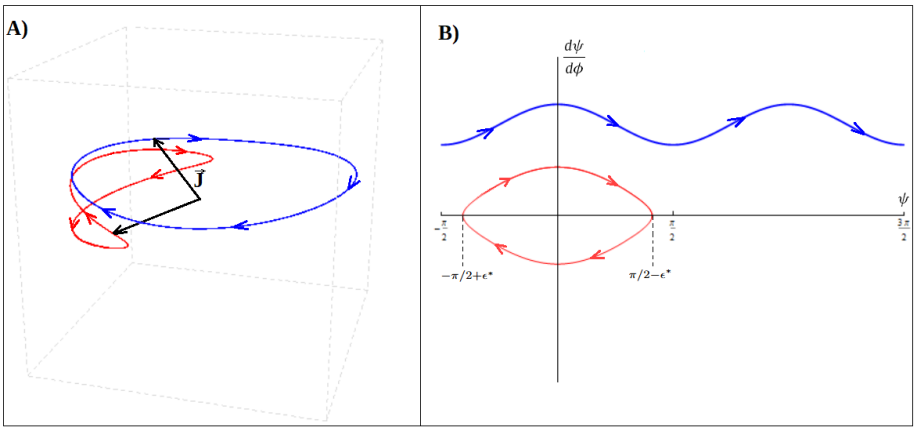

Figure 3.10: On the left panel the complete turn of the momentum vector is represented for oscillating (red) and rotating (blue) trajectories. On the right panel, we have the corresponding trajectories on the reduced phase space $\frac{d\psi}{d\phi}$.

3.6 Lower bound for the Dzhanibekov effect

A similar analysis, as the one used for rotating trajectories, can be done to describe the existence of the Dzhanibekov effect with a given value of the variation of the angle ϕ.

Notice that for the Dzhanibekov effect, we have that the variation of the angle ψ is exactly π. Thus, in this framework, the Dzhanibekov effect is only observed for rotating trajectories. *i.e.*, for $0 \leq c < a$.

The result describing the existence of the Dzhanibekov effect is stated as follows.

Proposition 3.18. Given a value $\alpha \in \mathbb{R}$, the Dzhanibekov effect with value $\Delta\phi = \alpha$ occurs if and only if $\pi\mathcal{J} < \alpha$. In other words, the infimum of the possible values angles to observe the Dzhanibekov effect is given by $\pi\mathcal{J}$, which is only reached in the limit $c \to a$.

Proof. Showing the existence of the Dzhanibekov effect with value $\Delta\phi = \alpha$ amounts to show the existence of $c_D \in (0, a)$ such that

$$\alpha = F_{a,b}(c_D, 0) = \frac{1}{\sqrt{ab}} \int_0^1 \frac{1 - bx}{\sqrt{x(1-x)\left(1 + \frac{b}{a}x\right)\left(x + \frac{c_D}{b}\right)}} dx. \tag{3.70}$$

We have that $F_{a,b}(c, 0)$ goes to ∞, when c goes to 0. Moreover, following computations done for the rotating trajectories, one obtains that $F_{a,b}(c, 0)$

is a decreasing function on $(0, a)$ with greatest lower bound equal to $\pi\mathcal{J}$. In other words, one obtains

$$\lim_{c\to a} F_{a,b}(c, 0) = \pi\mathcal{J}. \tag{3.71}$$

We conclude that the Dzhanibekov effect with value $\Delta\phi = \alpha$ occurs if and only if $\pi\mathcal{J} < \alpha$. The second part of the proposition is now a direct result. □

Notice that, this greater lower bound $\pi\mathcal{J}$ is one-half of the one found for the Montgomery phase.

Below, some values of this greater lower bound are shown for different objects.

Object	a	b	$\mathcal{J}$	$\pi\mathcal{J}$
Racket	12.54	0.06	0.0771	0.2424
Wing nut	2.92	0.0972	0.3209	1.008
Skate board	8.82	0.078	0.1084	0.3507
Mobile phone	2.97	0.198	0.2941	0.924
Book	1.11	0.31	0.6828	2.1451

Table 3.1: Values of the greatest lower bound $\pi\mathcal{J}$ for different objects [48].

3.7 Conclusions

The problems analyzed in this first part of the present thesis are holonomy phenomena, that is, detecting the variation of something given along a solution of the differential equation. These phenomena are strongly related to monodromy phenomena, the next part of the thesis studies Hamiltonian monodromy; and, in Chapter A of perspectives, we explain an explicit link between these two parts of the thesis.

Part II

Hamiltonian monodromy

Chapter 4

Preliminaries

Hamiltonian integrable systems with a finite number of degrees of freedom have a long history going back from Liouville in the mid-nineteenth century to Arnold one hundred years later [3]. A modern description of integrable systems was formulated in the last decades in terms of Lax pairs [42, 9]. In this context, a Lax pair consists of two matrix-valued functions on the phase space satisfying a differential equation equivalent to the Hamiltonian dynamics. When one can derive such a Lax pair, this approach is a powerful tool for finding the constants of motion of the integrable system.

Additionally, geometric and topological properties are known to provide valuable insights into the dynamics and the structure of such systems [18, 3]. One of these geometrical properties is Hamiltonian Monodromy (HM) which was introduced by Duistermaat in 1980 [28]. In short, HM is the simplest topological obstruction to the existence of global action-angle coordinates in a completely integrable Hamiltonian system. The quantum analog of HM was formulated mathematically few years later [23, 35, 72] and was also at the origin of many studies in physics, as a way to describe the global structure of quantum spectra [62, 25, 24, 20, 10, 6, 57, 29].

For completely integrable systems with compact fibers, the phase space is fibered by tori or by disjoint union of tori over the set of regular values. HM describes the possible nontriviality of the torus bundle over a loop in the set of such regular values [22, 30]. HM is characterized by a matrix with integer coefficients, the Monodromy matrix, that corresponds to the transformation of a basis of the first homology group of a compact regular fiber along a loop. In this study, we consider two degrees of freedom systems with a global circle action over the phase space [22, 30]. In this case, HM can be studied by analyzing a function on the phase space, namely the rotation number Θ.

A similar concept of Monodromy appears in complex geometry with the Picard-Lefschetz theory for Riemann surfaces [4, 75]. A natural question is to determine what relation may exist between these two forms of Monodromy. We propose, in this part, to do this analysis in an explicit way by showing in particular how to compute the variation of the rotation number from the Lax pair formalism. More precisely, starting from the Lax pair of the Hamiltonian system under study, we show that a complex reduced phase space can be defined as a set of Riemann surfaces depending on the constants of motion of the system. We establish generic conditions that this complex fibration must satisfy to exhibit a non-trivial monodromy. In this setting, we show that the rotation number is expressed as an Abelian integral of a meromorphic one-form with a nonzero residue at infinity. The last step of our approach consists of combining the two results to get the Monodromy matrix of the system.

Since non-trivial monodromy is not limited to systems for which a Lax pair is known, we introduce, what we call a quasi-Lax pair formalism. It corresponds to a Lax pair up to higher order terms valid in a neighborhood of focus-focus point. It can be derived for any Hamiltonian system locally around this singularity. Using the procedure described above with some adaptations, we obtain the monodromy matrix characterizing the focus-focus singularity. Some open questions and generalizations to higher-dimensional integrable systems are discussed in Appendix A.

4.1 Hamiltonian monodromy

In the first chapter of the previous part, we introduced the concept of Hamiltonian differential equation and first integral. We explained that in higher dimensions more first integrals are needed in order to find the solutions, but we did not specify how many of them are required. Locally, in $\mathbb{R}^{2n}$ only n first integrals are necessary to find the solutions to the Hamiltonian differential equation. This is a well-known result called *Arnold-Liouville* Theorem. In this chapter, we properly state this result, we introduce a coordinate system called action-angle coordinates and the concept of Hamiltonian monodromy. Let us begin with some basic definitions [43].

Definition 4.1. Let $F\colon M \to N$ be a smooth map between smooth manifolds. A point $p \in M$ is said to be a regular point of F, if $dF_p\colon T_pM \to T_{F(p)}N$ is surjective; it is a critical point otherwise.

Definition 4.2. Let $F\colon M \to N$ be a smooth map between smooth manifolds. A point $c \in N$ is said to be a regular value of F if every point of the level set $F^{-1}(c)$ is a regular point, and a critical value otherwise.

Definition 4.3. Let $F\colon M \to N$ a smooth map between smooth manifolds. A level set $F^{-1}(c)$ is called a regular fiber, if c is a regular value of F.

We introduce the set Σ_F which denotes the set of all critical values of the map F. By Sard's Theorem, Σ_F has measure zero in N. This set is a key element in understanding the concept of Hamiltonian monodromy.

Let us now consider a Hamiltonian differential equation in $\mathbb{R}^{2n}$ with coordinates $(q_1, \ldots, q_n, p_1, \ldots, p_n)$ and Hamiltonian $H\colon \mathbb{R}^{2n} \to \mathbb{R}$. Thus, the differential equation can be written as

$$\begin{aligned} \dot{q}_i &= \frac{\partial H}{\partial p_i}, \\ \dot{p}_i &= -\frac{\partial H}{\partial q_i}, \end{aligned} \tag{4.1}$$

with $i \in \{1, \ldots, n\}$.

Given two smooth functions defined over this phase space, $f\colon \mathbb{R}^{2n} \to \mathbb{R}$, $g\colon \mathbb{R}^{2n} \to \mathbb{R}$, we define the Poisson bracket of these functions as follows

$$\{f, g\} = \sum_{i=1}^{n} \left(\frac{\partial f}{\partial q_i}\frac{\partial g}{\partial p_i} - \frac{\partial f}{\partial p_i}\frac{\partial g}{\partial q_i} \right). \tag{4.2}$$

Since the functions are defined over the phase space, we have that $\dot{f} = \{f, H\}$. Thus, a function f is a first integral, of the Hamiltonian differential equation (4.1), if and only if $\{f, H\} = 0$.

Definition 4.4. Let $f_1, \ldots, f_k$ be k first integrals of the Hamiltonian differential equation (4.1). The set $\{f_1, \ldots, f_k\}$ is said to be in involution if $\{f_i, f_k\} = 0$, for all $1 \leq i, j \leq k$.

Geometrically, this definition is equivalent to requiring that the level sets of each function are invariant under the flow of each other function.

Definition 4.5. Let $f_1, \ldots, f_k$ be k first integrals of the Hamiltonian differential equation (4.1). The set $\{f_1, \ldots, f_k\}$ is said to be independent if the set of critical points of $F = (f_1, \ldots, f_k)$ has measure zero in $\mathbb{R}^{2n}$

This definition is introduced in order to have "new" information with each first integral.

Definition 4.6. A Hamiltonian system with first integrals $f_1 = H, \ldots, f_k$ is called a completely integrable system if $k = n$ and the set $\{f_1, \ldots, f_k\}$ is independent and in involution.

For a completely integrable system, the map $F = (f_1, \ldots, f_k)$ is called energy-momentum map and in $\mathbb{R}^2$ we denote it as $\mathcal{EM}$. The definition of completely integrable system is linked with the result that we mentioned before and that we now formally state.

Theorem 4.7 (Arnold-Liouville Theorem)**.** Let us consider a completely integrable system $f_1 = H, \ldots, f_n$ in $\mathbb{R}^{2n}$, with energy-momentum map $F = (f_1, \ldots, f_n)$ with compact fibers. Under these conditions, each connected component of a regular fiber of F is diffeomorphic to a real torus $\mathbb{T}^n$. Moreover, for an open subset $U \subset \mathbb{R}^n$ such that $U \cap \Sigma_F = \emptyset$, there exists a local diffeomorphism

$$\begin{aligned} \Phi \colon F^{-1}(U) &\to U \times \mathbb{T}^n \\ (q, p) &\mapsto (I, \varphi), \end{aligned}$$

which transforms the Hamiltonian differential equation into

$$\begin{aligned} \dot{I} &= 0 \\ \dot{\varphi} &= V(I). \end{aligned}$$

Notice that the local diffeomorphism gives a local change of coordinates that allows solving the differential equation. This is the reason why these systems are called completely integrable systems. This local change of coordinates is called action-angle coordinates.

The new form of the differential equation allows to detect the geometric structure of the Hamiltonian dynamics since it is a linear flow over invariant tori.

In 1980, Duistermaat [28] described the conditions to have global action-angle coordinates. In this article, the concept of Hamiltonian monodromy is introduced. We now describe it.

Assume that the fibers of F are compact and connected. Consider a regular value $c_0 \in F(\mathbb{R}^{2n}) \setminus \Sigma_F$ and an element $[\Gamma] \in \pi_1(F(\mathbb{R}^{2n}) \setminus \Sigma_F, c_0)$. Using the Arnold-Liouville Theorem, we have that $F^{-1}(\Gamma)$ is a fiber bundle over Γ with $\mathbb{T}^n$ as fiber and local trivializations given by the action-angle coordinates. This bundle is trivial if it is diffeomorphic to $\mathbb{S}^1 \times \mathbb{T}^n$.

Definition 4.8. A completely integrable system with compact connected fibers has monodromy (or non-trivial Hamiltonian monodromy), if there exists a class $[\Gamma] \in \pi_1(F(\mathbb{R}^{2n}) \setminus \Sigma_F, c_0)$ for which the fiber bundle $F^{-1}(\Gamma)$ over Γ is not trivial [30].

It turns out that Hamiltonian monodromy is the simplest topological obstruction to the existence of global action-angle coordinates [28].

Theorem 4.9 (Duistermaat)**.** A system with non-trivial Hamiltonian monodromy has no globally defined action-angle coordinates.

There exists another obstruction to the existence of global action-angle coordinates, we briefly describe it in Appendix A.

Notice that, if there exists globally defined action-angle coordinates, we have all the information about the system, since we can solve the dynamical equations. This is the importance of knowing if a given system can have global action-angle coordinates, or not.

We now describe a geometric way of studying Hamiltonian monodromy and we introduce the monodromy matrix. For other descriptions of Hamiltonian monodromy see [63].

Using Arnold-Liouville Theorem, we know that for each point $c \in \Gamma$, the corresponding fiber is a real torus $\mathbb{T}^n$. We can fix n generators of the first homology group of this fiber $H_1(F^{-1}(c), \mathbb{Z})$, and using the local trivializations, analyze how these elements change when the point on Γ changes. After a complete turn following Γ, we arrive at the initial fiber, and hence, we can compare the generators that we fix at the beginning with the final elements that we obtain. If these elements are the fixed generators, then the Hamiltonian monodromy is trivial and it is non-trivial otherwise.

Notice that this construction gives a linear map from $H_1(F^{-1}(c), \mathbb{Z})$ into itself. Thus we can describe this map with a matrix with integer coefficients. This matrix only depends on the homotopy class of $[\Gamma]$ and we denote it as $\mathcal{M}_\Gamma$. In terms of this matrix, we say that the Hamiltonian monodromy along Γ is trivial if $\mathcal{M}_\Gamma = \mathrm{Id}$, where Id is the identity matrix, and it is non-trivial otherwise.

Given a physical system, the computation of this matrix is not an easy task. In fact, in higher dimensions, it is very difficult to compute it. Even on $\mathbb{R}^4$ it is not straightforward to calculate it. Nevertheless, there exists a particular case where generators of the first homology group can be obtained from the flows of the first integrals. We describe this case.

Most physical systems admit symmetries, in the sense that the system is invariant under certain transformations. Emmy Noether proved that these symmetries always correspond to a first integral of the system. This result is known as Noether's Theorem [3].

Theorem 4.10 (Noether's Theorem)**.** Let $(M = \mathbb{R}^{2n}, H)$ be a Hamiltonian system and $\{g_s \colon M \to M\}_{s\in\mathbb{R}}$ a one-parameter group of diffeomorphisms. If H is invariant under this family of diffeomorphisms, then the Hamiltonian

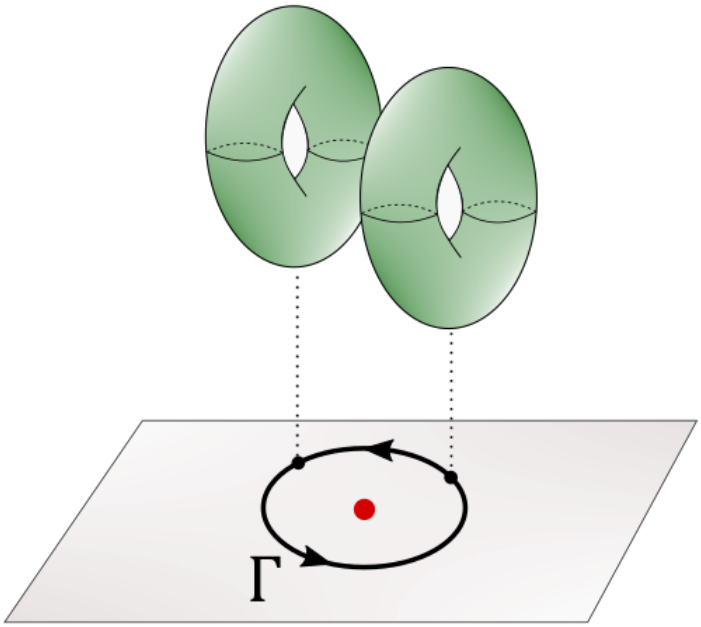

Figure 4.1: Geometrical description of Hamiltonian monodromy.

differential equation corresponding to H admits a first integral I that can be written in terms of g_s.

Thus, due to this correspondence, a system with a symmetry has always a first integral associated with the symmetry. The special case that we study in this thesis, is a system in $\mathbb{R}^4$ with a symmetry given by an $\mathbb{S}^1$-action. We explain why this case is easier to analyze.

Let us consider a completely integrable system in $\mathbb{R}^4$ and let $\mathcal{EM}$ be its energy-momentum map, *i.e.*, $\mathcal{EM} = (H, K)\colon \mathbb{R}^4 \to \mathbb{R}^2$. As mentioned before, this map defines a fibration and we assume that the fibers are compact and connected. *The bifurcation diagram* is the image of the energy-momentum map. We consider a system with a symmetry given by a global $\mathbb{S}^1$-action whose first integral (in the sense of Noether's Theorem) is K. In this case, we can analyze the first homology group of the fibers $H_1(F^{-1}(c), \mathbb{Z})$ with the Hamiltonian flows of H and K as follows.

Since K defines an $\mathbb{S}^1$-action, its Hamiltonian flow has closed orbits [30] of period 2π, and, we can define the rotation number. Consider a point (q, p) belonging to a regular torus $\mathcal{EM}^{-1}(h, k)$, and the closed orbit of K starting at this point. Let γ be the orbit of the flow generated by H starting at (q, p) and ending at the first point of intersection with the orbit of K at

positive time T called the first return time. The rotation number is defined as the time taken to go, with the Hamiltonian flow defined by K, from the point (q, p) to this first point of intersection (see Fig. 4.2).

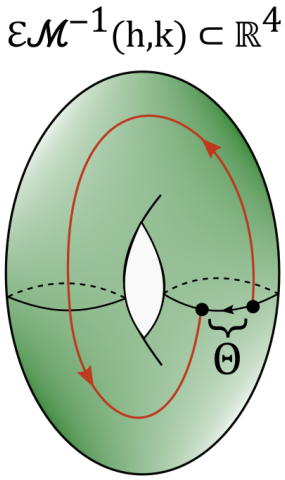

Figure 4.2: Definition of the first return time and the rotation number.

If we denote by θ the canonically conjugate angle to K, *i.e.* $\{\theta, K\} = 1$,then the rotation number Θ can be defined as

$$\Theta = \int_\gamma d\theta = \int_0^T \{\theta, H\}\, dt = \int_0^T \dot{\theta} dt.$$

An important property of T and Θ is that they only depend on the fiber that we consider, in other words, they only depend on the values of H and K [31].

These two functions allow to codify the information on the first homology group of the fiber, in terms of the Hamiltonian flows of H and K, since we can consider an orbit of K and the closed curve obtained by following the Hamiltonian flow of H during the time T and then close it following the Hamiltonian flow of K during a time Θ. These two closed curves form a basis of the first homology group of the fiber and we can study the variation of these elements by following the Hamiltonian flows defined by H and K.

The results that are obtained in Chapter 6 are established in this framework, where we study Hamiltonian monodromy along loops around an isolated critical value of $\mathcal{EM}$, via spectral Lax pairs. Thus, we now introduce spectral Lax pairs.

4.2 Spectral Lax pairs

In this section, we introduce the concept of Spectral Lax pairs and describe some of their properties, which are used later in this study.

Definition 4.11. Let $L(t)$ and $B(t)$ be a pair of $n \times n$ time-dependent matrices acting on $\mathbb{R}^n$, L and B form a *Lax pair* if they satisfy the relation

$$\frac{dL}{dt} = [B, L] = BL - LB.$$

The first property of Lax pairs is described in the following Lemma.

Lemma 4.12. Let $L(t)$, $B(t)$ be a Lax pair. Any invertible solution $U(t)$ of the equation $\frac{dU}{dt} = B(t)U(t)$ satisfies the equality $\frac{d}{dt}(U^{-1}(t)L(t)U(t)) = 0$.

Using this property, it is easy to prove the following result.

Corollary 4.13. Let $L(t)$, $B(t)$ be a Lax pair. If $U(t)$ is an invertible solution of the equation $\frac{dU}{dt} = B(t)U(t)$ and $U(0) = Id$, then $L(t) = U(t)L(0)U^{-1}(t)$.

Finally, using the previous two results, one can prove the following result which is the main property of Lax pairs.

Theorem 4.14. Let $L(t)$, $B(t)$ a Lax pair. The functions $F_k = \mathrm{Tr}(L^k)$ and the eigenvalues of L are constants of the motion.

Proof. Let $U(t)$ be an invertible solution of equation $\frac{dU}{dt} = B(t)U(t)$ such that $U(0) = Id$. By Corollary 4.13

$$L(t) = U(t)L(0)U^{-1}(t).$$

Thus

$$L^k(t) = U(t)L^k(0)U^{-1}(t),$$

and

$$\mathrm{Tr}(L^k(t)) = \mathrm{Tr}(U(t)L^k(0)U^{-1}(t)) = \mathrm{Tr}(L^k(0)),$$

because of the invariance of the trace under conjugation. Then the functions $F_k = \mathrm{Tr}(L^k(t))$ are constants of motion.

On the other hand, the eigenvalues are roots of the equation

$$0 = \det(\lambda Id - L(t)),$$

but we have

$$\begin{aligned} 0 &= \det(\lambda Id - L(t)) \\ &= \det(\lambda Id - U(t)L(0)U^{-1}(t)) \\ &= \det(\lambda U(t)U^{-1}(t) - U(t)L(0)U^{-1}(t)) \\ &= \det(U(t)(\lambda Id - L(0))U^{-1}(t)) \\ &= \det(U(t))det(\lambda Id - L(0))det(U^{-1}(t)) \\ &= \det(\lambda Id - L(0)). \end{aligned}$$

We conclude that the eigenvalues of $L(t)$ are the same as those of $L(0)$ thus, are constants of the motion. □

Given a completely integrable system, a *Lax pair* describing this system is a pair of square matrices L and M which fulfill the equation

$$\dot{L} = [M, L],$$

and such that, by identifying element by element the two sides of this matrix-valued differential equation, we find the equations of motion of the original dynamical system. A *spectral Lax pair* is a Lax pair for which the matrices $L(\lambda)$ and $M(\lambda)$ depend on an extra parameter λ called *spectral parameter*. The *spectral curve* is defined by the characteristic polynomial of L, *i.e.*, by $\det(L(\lambda) - \mu I) = 0$. If the dependence of L on the spectral parameter is polynomial then the spectral Lax pair defines a spectral curve that is polynomial in the variables λ and μ and such that all its coefficients are constants of motion (due to Theorem 4.14).

The spectral curve is the main tool that we use to study Hamiltonian monodromy.

Examples

In this section, we give three examples of physical systems and their corresponding Lax pairs to better understand this tool.

As a first example we take a system already studied in the previous part, Euler equations for the rigid body:

$$\begin{aligned} \dot{M}_1 &= (\frac{1}{I_3} - \frac{1}{I_2})M_2M_3, \\ \dot{M}_2 &= (\frac{1}{I_1} - \frac{1}{I_3})M_1M_3, \\ \dot{M}_3 &= (\frac{1}{I_2} - \frac{1}{I_1})M_1M_2, \end{aligned}$$

with the relations $M_1 = I_1\Omega_1$, $M_2 = I_2\Omega_2$, $M_3 = I_3\Omega_3$.

We consider the following matrices

$$M = \begin{pmatrix} 0 & -M_3 & M_2 \\ M_3 & 0 & -M_1 \\ -M_2 & M_1 & 0 \end{pmatrix}, \quad \Omega = \begin{pmatrix} 0 & \Omega_3 & -\Omega_2 \\ -\Omega_3 & 0 & \Omega_1 \\ \Omega_2 & -\Omega_1 & 0 \end{pmatrix}.$$

It is easy to verify that M and Ω form a Lax pair. Now we are interested in finding a Lax pair depending on a spectral parameter in order to analyze the spectral curve. We introduce the matrix

$$J = \begin{pmatrix} J_1 & 0 & 0 \\ 0 & J_2 & 0 \\ 0 & 0 & J_3 \end{pmatrix} = \begin{pmatrix} \frac{I_3+I_2-I_1}{2} & 0 & 0 \\ 0 & \frac{I_3+I_1-I_2}{2} & 0 \\ 0 & 0 & \frac{I_1+I_2-I_3}{2} \end{pmatrix}$$

(note that $M = -(J\Omega + \Omega J)$) and we define the matrices $L(\lambda) = M + \lambda J^2$ and $N(\lambda) = \Omega - \lambda J$, $\lambda \in \mathbb{R}$.

The matrices $L(\lambda)$ and $N(\lambda)$ form a Lax pair depending on the spectral parameter λ. Thus, they satisfy equation $\dot{L} = [N, L]$, and these equations of motion are equivalent to Euler equations (this can be verified by direct computations).

The spectral curve is given by the equation

$$0 = \det(L(\lambda) - \mu Id) = \det \begin{pmatrix} \lambda J_1^2 - \mu & -M_3 & M_2 \\ M_3 & \lambda J_2^2 - \mu & -M_1 \\ -M_2 & M_1 & \lambda J_3^2 - \mu \end{pmatrix},$$

which can be written as

$$\begin{aligned} &\mu^3 - \mu^2\lambda(J_1^2 + J_2^2 + J_3^2) + \mu\lambda^2(J_1^2J_2^2 + J_1^2J_3^2 + J_2^2J_3^2) \\ &\quad -\lambda^3(J_1^2J_2^2J_3^2) - \lambda(J_1^2M_1^2 + J_2^2M_2^2 + J_3^2M_3^2) + \mu(M_1^2 + M_2^2 + M_3^2) = 0, \end{aligned}$$

this curve has a simple pole at $\lambda = \infty$.

In the article [38] some symmetries of this system are introduced, after reduction, the authors obtain a 4-dimensional system with two conserved quantities (two first integrals). Thus, this system (after reduction of symmetries) is a completely integrable system, nevertheless, the non-simply connectedness of its bifurcation diagram makes its study more complex, this point is addressed in Section A.3 of perspectives.

We now give the spectral Lax pairs of two systems that are described in Chapter 8, refer to this Chapter for details. In this part of the text, we just present the equations of motion and their corresponding Lax pairs.

The first system is the spherical pendulum (see Chapter 8 for details), the dynamical equations can be expressed as

$$\begin{aligned}\dot{\vec{q}} &= \vec{p} \\ \dot{\vec{p}} &= \vec{e}_z - (p_x^2 + p_y^2 + p_z^2 - z)\vec{q},\end{aligned}$$

where $\vec{e}_z = (0, 0, -1)$ is a unit vector along the z- direction.

To simplify the analysis, we introduce the coordinates (L_x, L_y, L_z) and (M_x, M_y, M_z) defined as

$$\begin{aligned}L_x &= x - \lambda K_x \\ L_y &= y - \lambda K_y \\ L_z &= z - \lambda K_z + \lambda^2\end{aligned}$$

and

$$\begin{aligned}M_x &= K_x \\ M_y &= K_y \\ M_z &= K_z - \lambda,\end{aligned}$$

where $\vec{K}$ is the angular momentum $\vec{K} = \vec{q} \times \vec{p}$ with $\dot{\vec{K}} = \vec{q} \times \vec{e}_z$.

Thus, the Lax matrices L and M (which satisfy $\dot{L} = [M, L]$) can be expressed as:

$$\begin{aligned}L &= L_x\sigma_x + L_y\sigma_y + L_z\sigma_z \\ M &= \frac{-i}{2}(M_x\sigma_x + M_y\sigma_y + M_z\sigma_z),\end{aligned}$$

where σ_x, σ_y, and σ_z are the Pauli matrices:

$$\sigma_x = \begin{pmatrix} 0 & 1 \\ 1 & 0 \end{pmatrix}, \quad \sigma_y = \begin{pmatrix} 0 & -i \\ i & 0 \end{pmatrix}, \quad \sigma_z = \begin{pmatrix} 1 & 0 \\ 0 & -1 \end{pmatrix}.$$

The spectral curve is given by

$$\mu^2 = \lambda^4 - 2K_z\lambda^3 + 2(\frac{1}{2}(p_x^2 + p_y^2 + p_z^2) + z)\lambda^2 + 1,$$

which is of the form $\mu^2 = Q(\lambda)$ with Q a polynomial of degree 4 with constants of motion as coefficients.

Finally, we consider the Jaynes-Cummings model (see Chapter 8 for details) whose phase space is $\mathbb{S}^2 \times \mathbb{R}^2$. The coordinates of $\mathbb{S}^2$ are denoted by (S_x, S_y, S_z), with the constraint $S_x^2 + S_y^2 + S_z^2 = S_0^2$ (where S_0 is a positive

constant). The coordinates of $\mathbb{R}^2$ are given by (q, p). Complex coordinates, S_+, S_- and b, are introduced to simplify the description, as follows

$$\begin{aligned} S_+ &= S_x + iS_y \\ S_- &= S_x - iS_y \\ b &= \frac{1}{\sqrt{2}}(q + ip). \end{aligned}$$

The Hamiltonian dynamics are governed by the following differential equations

$$\begin{aligned} \dot{S}_+ &= 2i\omega_0 S_+ - 2ig\bar{b}S_z \\ \dot{S}_z &= ig\bar{b}S_- - igbS_+ \\ \dot{b} &= -i\omega b - igS_-, \end{aligned} \tag{4.3}$$

where ω_0, ω, and g are real constants.

We consider the Lax matrices L and M defined by

$$L(\lambda) = \begin{pmatrix} \frac{(2\lambda-\omega)(\lambda-\omega_0)+g^2S_z}{g^2} & \frac{2b(\lambda-\omega_0)}{g} + S_- \\ \frac{2\bar{b}(\lambda-\omega_0)}{g} + S_+ & \frac{(\omega-2\lambda)(\lambda-\omega_0)-g^2S_z}{g^2} \end{pmatrix}$$

and

$$M(\lambda) = \begin{pmatrix} -i\lambda & -igb \\ -ig\bar{b} & i\lambda \end{pmatrix}.$$

Thus, they fulfill equation $\dot{L} = [M, L]$, and the equations obtained entry by entry are equivalent to the equations describing the Hamiltonian dynamics (4.3). The spectral curve is of the form $\mu^2 = Q(\lambda)$, where Q is a polynomial of degree 4 with constants of motion as coefficients. This spectral curve is explicitly given in Chapter 8.

We now proceed to the study of Hamiltonian monodromy using spectral Lax pairs, by first obtaining some auxiliary results that will help us to describe the geometric structure of the problem.

Chapter 5

Auxiliary results

As mentioned before, in this chapter we develop the technical results needed to prove the main results of this part. Since the main results describe Hamiltonian monodromy through the Lax pair structure, in this chapter we study the geometric and analytic structure of the type of spectral curves that one obtains from Lax pairs. In this study, these are elliptic curves.

We begin the study by describing meromorphic forms defined over these curves. Then, we derive a normal form for the spectral curve and, finally, we describe the movement of ramification points defining these elliptic curves, when the values of the parameters h and k vary.

The content of this Chapter, as well as the following ones: Chapters 6, 7, and 8, has been published in Journal of Mathematical Physics [37].

5.1 Meromorphic forms on Riemann surfaces

In this section, we show that meromorphic forms on elliptic curves $\mu^2 = Q_4(\lambda)$ having at most simple poles at infinity are generated by $\{\frac{\lambda d\lambda}{\mu}, \frac{d\lambda}{\mu}\}$. The following proposition states this result which is the first auxiliary result needed for the proofs of the main results.

Proposition 5.1. Consider a regular elliptic curve given by the equation $F(\lambda, \mu) = 0$, of the form $F(\lambda, \mu) = \mu^2 - Q(\lambda)$, with Q a square-free polynomial of degree four. Then, the space of meromorphic forms having at most simple poles at infinity is two-dimensional, generated by $\{\frac{\lambda d\lambda}{\mu}, \frac{d\lambda}{\mu}\}$.

Proof. The proof follows from the general study of the space of meromorphic functions and forms on Riemann surfaces in the spirit of the Riemann-Roch theorem. All the references can be found in the classical book [50].

Let X be a compact Riemann surface given by the compactification

$$X = F^{-1}(0) \cup \{-\infty, +\infty\}, \tag{5.1}$$

of the complexification of F^{-1}, obtained by adding two points at infinity (one for each leaf). We denote $\mathcal{M}$ and $\mathcal{M}^{(1)}$ respectively, the space of meromorphic functions and forms on X. Given $f \in \mathcal{M}$, we associate its divisor $\mathrm{div}(f) = \sum_{p \in X} \mathrm{ord}_p(f)p$. Taking $\omega \in \mathcal{M}^{(1)}$, we define similarly $\mathrm{div}(\omega)$, by using local uniformizations of ω at any point p of X. The supports of the sum are finite. Let D be a divisor. We define the vector spaces

$$L(D) = \{f \in \mathcal{M}(X) : \mathrm{div}(f) \geq -D\},$$

and

$$L^{(1)}(D) = \{\omega \in \mathcal{M}^{(1)}(X) : \mathrm{div}(\omega) \geq -D\}.$$

We are interested in one-forms having at most simple poles at infinity. Note that a form cannot have only one pole with nonzero residue as the sum of residues on a compact surface is zero. Hence, we take the divisor $D = 1 \cdot (+\infty) + 1 \cdot (-\infty)$ and consider $L^{(1)}(D)$. Using [50] (Chapter V, Lemma 3.11), we have for any Riemann surface

$$\dim L^{(1)}(D) = \dim L(D + K_d),$$

where K_d is a canonical divisor (i.e. divisor of any meromorphic form on the Riemann surface X).

Now, we restrict to X, given by Eq. (5.1). Note that the form $\omega = \frac{d\lambda}{\mu}$ is holomorphic on X and does not have zeros. Hence, the canonical divisor K_d is the zero divisor, so for the elliptic curve, we get $\dim L^{(1)}(D) = \dim L(D)$. The Riemann surface X is a torus and Proposition 3.14 of Chapter V [50] applies and gives $\dim(L(D)) = \deg(D) = 2$. Thus

$$\dim L^{(1)}(D) = 2.$$

On the other hand, by the same analysis, but for the 0 divisor, we obtain $\dim L^{(1)}(0) = 1$ (this space is generated by the holomorphic form $\frac{d\lambda}{\mu}$). One verifies easily that $\mathrm{Res}(\frac{\lambda d\lambda}{\mu}, \pm\infty) \neq 0$ (and this residue is equal to ± 1, when Q is unitary). Hence, the forms $\{\frac{\lambda d\lambda}{\mu}, \frac{d\lambda}{\mu}\}$ generate the space $L^{(1)}(D)$, and the differential one-forms in this space with nontrivial residues at $\pm\infty$ have a non-zero component in $\frac{\lambda d\lambda}{\mu}$. □

5.2 Normal form

The second step is to find a normal form of the spectral curves that we will study. In this way, the proofs and the geometric analysis will be simpler and easier to understand. In this section, we also formulate the genericity condition (G) that will be used in Theorem 6.1.

The conditions on the elliptic curves stated in the following lemma are conditions verified by the spectral curves that we study. The value (h_0, k_0) will play later the role of the critical value of the energy-momentum map of the system.

Lemma 5.2. Let $Q(\lambda, h, k)$ be a real polynomial of degree four. We assume that there exists (h_0, k_0) such that the polynomial $Q(\lambda, h_0, k_0) \in \mathbb{R}[\lambda]$ has two different double non-real roots. Assume that the differential of the function F (defined by Eq. (5.2) below) is invertible at (h_0, k_0). Moreover, by convention, we assume that[1]

$$\det \left[\frac{\partial F}{\partial (h,k)} \right]_{(h_0,k_0)} > 0. \tag{G}$$

Then there exists a local orientation preserving diffeomorphism

$$(\lambda, h, k) \mapsto (\hat{\lambda}(\lambda, h, k), \hat{h}(h, k), \hat{k}(h, k)),$$

which transforms the polynomial Q to the normal form polynomial

$$\hat{\lambda}^4 + (2 + \hat{h})\hat{\lambda}^2 + \hat{k}\hat{\lambda} + 1$$

multiplied by a unity.

Proof. First note that, since the polynomial Q has real coefficients, then its roots are complex conjugate. Let λ_0 and $\bar{\lambda}_0$ be the double roots for $(h, k) = (h_0, k_0)$.

After a first translation in the parameters (h, k), we set (h_0, k_0) equal to $(0, 0)$. By a translation and a homothety in the variable λ, the roots λ_0, $\bar{\lambda}_0$ are given by i and $-i$. We eliminate the cubic term by a translation in λ (which depends on h and k). In order to have the constant coefficient equal to 1, we consider a homothety on λ and factorize, leading to the polynomial

$$u(h, k)(\hat{\lambda}^4 + a(h, k)\hat{\lambda}^2 + b(h, k)\hat{\lambda} + 1),$$

[1] It is possible to work with the negative determinant but in this case, the change of orientation has to be taken into account.

where u is a unity in a neighborhood of (h_0, k_0) and $a(h_0, k_0) = 2$, $b(h_0, k_0) = 0$.

Finally, from the transformation $(h, k) \overset{F}{\mapsto} (\hat{h}, \hat{k})$, given by

$$F(h, k) = (a(h, k) - 2, b(h, k)), \tag{5.2}$$

which is a local diffeomorphism, by the inverse function theorem, we arrive at the normal form polynomial

$$\hat{Q}(\hat{\lambda}, \hat{h}, \hat{k}) = \hat{\lambda}^4 + (2 + \hat{h})\hat{\lambda}^2 + \hat{k}\hat{\lambda} + 1, \tag{5.3}$$

multiplied by the unity $u(F^{-1}(\hat{h}, \hat{k}))$. □

We point out that the change of variables in λ is global, while the change of variables in (h, k) is local. Thus, we can consider the transformation $(\lambda, \mu) \overset{G}{\mapsto} (\hat{\lambda}, \hat{\mu})$, where $\hat{\mu} = \frac{\mu}{\sqrt{u}}$, which is a global diffeomorphism and we obtain the normal form of the spectral curve

$$\hat{\mu}^2 = \hat{\lambda}^4 + (2 + \hat{h})\hat{\lambda}^2 + \hat{k}\hat{\lambda} + 1.$$

This normal form simplifies the calculations done in the next section, where the objective is to analyze the motion of the roots when the parameters $\hat{h}$ and $\hat{k}$ vary.

5.3 Monodromy of roots of the normal form polynomial

As mentioned before, in this section, we describe the motion of the roots of the normal form polynomial obtained in the previous Section when the parameters $\hat{h}$ and $\hat{k}$ vary along a circle around the origin (notice that this is equivalent to analyze the movement of the roots of the original polynomial when the parameters h and k vary along a circle around (h_0, k_0), but the computations are easier in the normalized case).

This is a key point in this work since, the monodromy of the surfaces of the form $\mu^2 = P_{h,k}(\lambda)$ is given by the movement of the roots of the polynomial $P_{h,k}(\lambda)$, when (h, k) varies along a loop around a singularity. In this sense, the monodromy of the roots codifies all the information about the monodromy of the surfaces and the loops on them. Thus, this is relevant to understand the geometric structure of the problem.

Lemma 5.3. Let $\hat{Q}(\hat{\lambda}, \hat{h}, \hat{k})$ be the polynomial defined by Eq. (5.3). For values of $(\hat{h}, \hat{k})$ close enough to $(0, 0)$, the polynomial $\hat{Q}(\hat{\lambda}, \hat{h}, \hat{k})$ has four roots of the form $i \pm \beta$, $-i \pm \bar{\beta}$, where $\beta \in \mathbb{C}$ depends on the value $(\hat{h}, \hat{k})$. Moreover, if $(\hat{h}, \hat{k})$ moves along a small loop around $(0, 0)$, then the two roots close to i turn around i until they exchange their positions, and the same statement holds for $-i$.

Proof. Consider a small circle $\mathcal{C}$ around the origin in the space $(\hat{h}, \hat{k})$ with positive orientation, *i.e.*,

$$\hat{h} = r\cos\phi$$
$$\hat{k} = r\sin\phi,$$

with $r \ll 1$ and $\phi \in [0, 2\pi]$. The polynomial

$$\hat{Q}_{\hat{h},\hat{k}}(\hat{\lambda}) = \hat{\lambda}^4 + (2 + \hat{h})\hat{\lambda}^2 + \hat{k}\hat{\lambda} + 1$$

has two double roots, i and $-i$, for $(\hat{h}, \hat{k}) = (0, 0)$. We set $\hat{\lambda} = \varepsilon i + z$, where $\varepsilon = \pm 1$. We substitute $\hat{\lambda}$ in the equation $\hat{Q}_{\hat{h},\hat{k}}(\hat{\lambda}) = 0$ and. The multivalued character of the roots is given by the terms obtained using a Newton diagram (See [21], Section 2.8). Thus, neglecting higher-order terms given by the Newton diagram of this polynomial equation, we obtain $-4z^2 \simeq \hat{h} - \varepsilon i\hat{k}$. The multivalued character of the roots is given by

$$-4z^2 = \hat{h} - \varepsilon i\hat{k}. \tag{5.4}$$

Thus, from Eq. (5.4), we deduce that the two roots near i behave like $i \pm \tilde{\beta}$ where $\tilde{\beta} = \sqrt{\frac{i\hat{k}-\hat{h}}{4}}$, with an appropriate logarithmic branch. Note that the square root argument is different from 0 because $\hat{h}$ and $\hat{k}$ are both real. Moreover, the roots can be written as $i \pm \beta$ (See [21], Section 2.8), and the roots near $-i$ are then of the form $-i \pm \bar{\beta}$ because the polynomial has real coefficients[2].

Now, we analyze the motion of these roots when $(\hat{h}, \hat{k})$ varies along $\mathcal{C}$. Setting $z = \rho e^{i\theta}$, with $\rho \ll 1$, and substituting the parametrization of $\mathcal{C}$, we obtain

$$-4\rho^2 e^{2i\theta} = re^{-i\varepsilon\phi},$$

which leads to

$$\rho = \frac{r^{1/2}}{2}$$
$$\theta = -\frac{\varepsilon\phi}{2} - \frac{\pi}{2} + k\pi,$$

with $k \in \mathbb{Z}$. We conclude that near each double root, we obtain two simple roots which exchange their positions along the loop $\mathcal{C}$ in the space $(\hat{h}, \hat{k})$. □

We now have all the auxiliary results that we need to prove the results linking the Hamiltonian monodromy of a system with the spectral curve and its algebraic structure. This is done in the following Chapter.

[2]The reader can refer to Section 8, Fig. 8.2, to see this behavior in a numerical plot obtained for a system presented as an example.

Chapter 6

Hamiltonian monodromy via spectral Lax pairs

The objective of this study is to obtain the monodromy matrix of a given system described by a spectral Lax pair using the algebraic structure of the spectral curve. In the previous chapter, we obtain auxiliary results describing the algebraic structure of spectral curves. In this chapter, we finally make this link explicit proving the main results of this part of the present thesis.

More explicitly, in this chapter, we study Hamiltonian Monodromy along loops around an isolated critical value of $\mathcal{EM}$, deriving a Riemann surface (given by the spectral curve of the spectral Lax pair) and using its algebraic structure.

Hence, in Theorem 6.1, we formulate a general result about integrals of meromorphic one-forms on this Riemann surface and, in Theorem 6.2, we give conditions under which the Monodromy is not trivial and calculate it using Theorem 6.1. As mentioned before, the conditions imposed on these results are obtained by studying well-known physical systems and their properties. Additionally, we present in Chapter 8 some of these well-known systems (which have a focus-focus singularity) and show that Theorem 6.2 applies and allows to easily derive the monodromy matrix of the systems.

6.1 Main results

We now recall the properties of the systems that we consider to establish the results of this work.

We focus on the study of Hamiltonian systems in $\mathbb{R}^4$ with Hamiltonian

H and an $\mathbb{S}^1$-action [1] generated by a second constant of motion K, that can be described by a spectral Lax pair, $L(\lambda)$, $M(\lambda)$, where L and M are complex 2×2 matrices and such that the matrix L can be expressed as follows

$$L(\lambda) = \begin{pmatrix} A(\lambda) & B(\lambda) \\ C(\lambda) & -A(\lambda) \end{pmatrix}. \tag{6.1}$$

Here A, B and C are polynomial functions of the parameter λ, with A of degree two, B and C of degree one.

Since Lax pairs are not unique, this requirement on the polynomial order is not strict, but we consider systems such that these degrees correspond to the simplest Lax pair. In other words, it corresponds to the simplest solution for which there exists a Lax pair.

The spectral curve is derived from the characteristic polynomial of L and is given by the equation $\mu^2 = A^2(\lambda) + B(\lambda)C(\lambda) = Q_{h,k}(\lambda)$, where μ denotes the eigenvalue of L and Q is a polynomial of degree four. Using the standard procedure of Lax pairs for defining separated variables [9], we introduce the functions $\tilde{\lambda}$ and $\tilde{\mu}$ respectively, as the solution of the implicit equation $C(\lambda) = 0$ and by the relation $\tilde{\mu}^2 = A(\tilde{\lambda})^2$.[2] This defines the multivalued mapping $\mathcal{L}\colon \mathbb{R}^4 \to \mathbb{C}^2 \times \mathbb{R}^2$ given by

$$\mathcal{L}(q,p) = (\tilde{\lambda}(q,p), \tilde{\mu}(q,p), \mathcal{EM}(q,p)),$$

that respects the fibers of the torus bundle. We point out that the variables $\tilde{\lambda}$ and $\tilde{\mu}$ can be viewed as the coordinates of a complex reduced phase space with respect to the momentum K [9]. In particular, the orbits of K are mapped to points in the image of $\mathcal{L}$ and the orbit of the Hamiltonian flow γ to a cycle $\mathcal{L}(\gamma)$ (see Fig. 6.1).

The different mappings are described by the commutative diagram given in Fig. 6.2. This diagram is schematically represented in Fig. 6.3. If $\mathcal{EM}$ has compact fibers for regular values, then, by the Arnold-Liouville theorem, the regular fibers of $\mathcal{EM}$ are real tori $\mathbb{T}^2$. In Sec. 6.2, we prove that the fibers of Φ are contained in Riemann surfaces. Let (h_0, k_0) be an isolated critical value in the bifurcation diagram and let Γ be a simple loop positively oriented contained in the set of regular values of $\mathcal{EM}$ around (h_0, k_0), such that (h_0, k_0) is the only critical value inside Γ. The first main result of this study is about the structure of the Riemann surface given by the spectral curve and it is stated as follows:

[1] As mentioned in Section 4.1, the definition of Hamiltonian monodromy does not require an $\mathbb{S}^1$-action but, if the system posses one, we can use the rotation number to compute the monodromy matrix.

[2] The solution of $C(\lambda) = 0$ also gives the position of the pole of the eigenvectors of L[9]

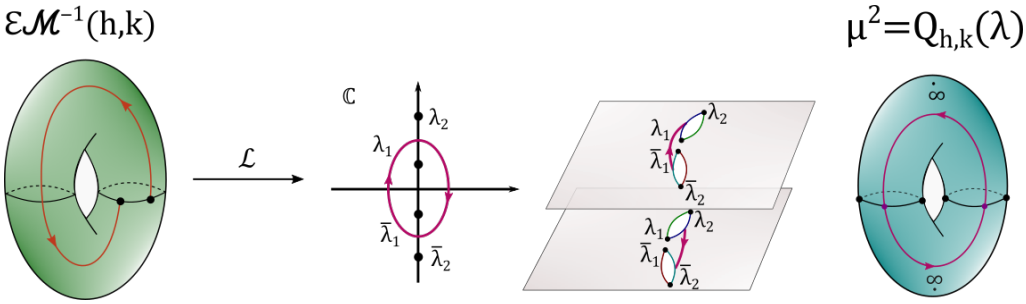

Figure 6.1: Image of the orbit of the Hamiltonian flow γ under the mapping $\mathcal{L}$. The first panel of the right-hand side is the complex plane where $\tilde{\lambda}$ lies, the two other panels on this side are different representations of the Riemann surface $\mu^2 = Q_{h,k}(\lambda)$.

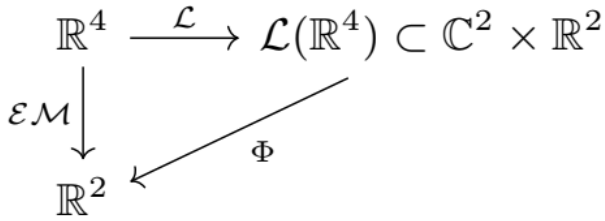

Figure 6.2: Commutative diagram between the mappings $\mathcal{EM}$, $\mathcal{L}$ and Φ, where Φ is the projection from $\mathcal{L}(\mathbb{R}^4) \subset \mathbb{C}^2 \times \mathbb{R}^2$ to $\mathbb{R}^2$.

Theorem 6.1. Under the above hypotheses on the system, assume that Q is a polynomial that has two non-real double roots for $(h, k) = (h_0, k_0)$ and fulfills the genericity condition (G) described in Section 5.2. Consider a one-form ξ in the space $(\tilde{\lambda}, \tilde{\mu})$ which can be written as $\xi = c_1 \frac{\tilde{\lambda} d\tilde{\lambda}}{\tilde{\mu}} + c_2 \frac{d\tilde{\lambda}}{\tilde{\mu}}$, $(c_1, c_2) \in \mathbb{C}^2$ (see Sec. 5.1). Let $\mathcal{I}$ be the integral $\int_{\mathcal{L}(\gamma)} \xi$, then the variation of $\mathcal{I}$ when h and k vary along Γ is given by $\Delta_\Gamma \mathcal{I} = 2\pi i \operatorname{Res}(\xi, +\infty)$.[3] Moreover, this residue can be expressed as

$$\operatorname{Res}(\xi, +\infty) = -\frac{c_1}{\sqrt{a_4}},$$

where a_4 is the leading coefficient of Q.

Theorem 6.1 is related to the Hamiltonian monodromy of the system because, as mentioned before, Hamiltonian monodromy can be studied from

[3] By $+\infty$ we mean the point at infinity in the upper leaf of the Riemann surface, *i.e.*, $\mu > 0$ for λ large enough.

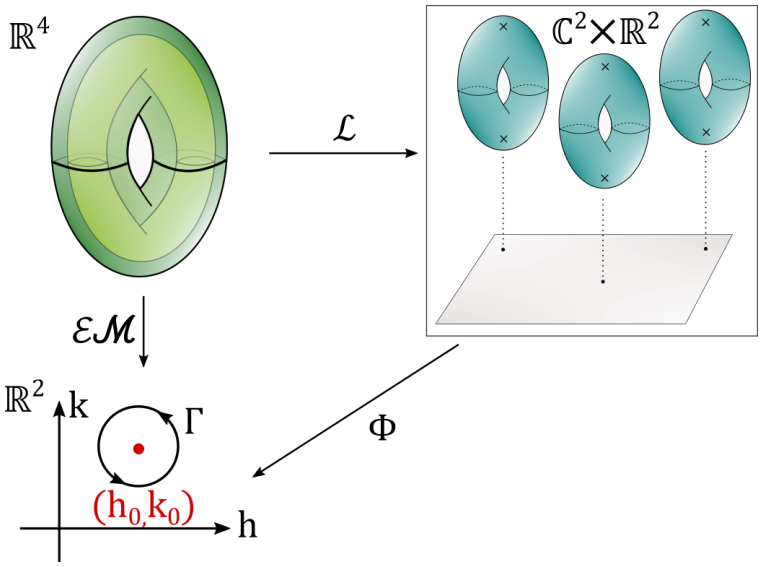

Figure 6.3: Schematic representation of the commutative diagram given in Fig. 6.2. The two upper panels describe respectively the fibration of the phase space by real tori $\mathbb{T}^2$ (left) and by complex tori (right). For each regular value (h,k), this complex torus is a Riemann surface with two points at infinity (crosses). The lower panel depicts the image of $\mathcal{EM}$ in the space (h,k). The red point indicates the position of the singular value (h_0,k_0). The oriented circle represents the loop Γ, for which the Monodromy matrix is computed.

the rotation number Θ, and Θ can be expressed as an integral of a one-form in the space $(\tilde{\lambda},\tilde{\mu})$.

More specifically, taking $\eta = \frac{\dot{\theta}}{\dot{\tilde{\lambda}}} d\tilde{\lambda}$, we get

$$\Theta = \int_\gamma d\theta = \int_{\mathcal{L}(\gamma)} \frac{d\theta}{d\tilde{\lambda}} d\tilde{\lambda} = \int_{\mathcal{L}(\gamma)} \eta.$$

Using the previous Theorem, we deduce that the study of HM boils down to the study of meromorphic forms in the space $(\tilde{\lambda},\tilde{\mu})$. As a consequence of Theorem 6.1, we obtain the following result.

Theorem 6.2. Consider a completely integrable Hamiltonian system in $\mathbb{R}^4$ as described above, in a neighborhood of an isolated critical point (q_0,p_0). Assume that $\mathrm{Res}(\eta,+\infty) = \frac{n}{i}$. Under the conditions given in Theorem 6.1, the Monodromy matrix $\mathbb{M}$, for Γ, is

$$\mathbb{M}_\Gamma = \begin{pmatrix} 1 & n \\ 0 & 1 \end{pmatrix},$$

in an appropriate basis.

We state the main results for two degrees of freedom systems but in Appendix A we discuss possible generalizations of the results to higher dimensional systems. Notice that the hypothesis of expressing ξ as $c_1\frac{\tilde{\lambda}d\tilde{\lambda}}{\tilde{\mu}} + c_2\frac{d\tilde{\lambda}}{\tilde{\mu}}$ comes form the study done in Sec. 5.1. In Sec. 8, we apply these results to two physical systems and we stress that the assumptions about the spectral Lax pair given by Eq. (6.1) are inspired by the study of well-known systems. Moreover, in Chapter 7, we show that any Hamiltonian system with a focus-focus singularity can be described, locally, by what we call a quasi-Lax pair of this form.

6.2 Proofs

The proofs of the main results are developed in this Section.

Proof of Theorem 6.1. The system is represented by a spectral Lax pair of the form given by Eq. (6.1) and the corresponding spectral curve is

$$\mu^2 = A^2(\lambda) + B(\lambda)C(\lambda)$$

where $Q_{h,k}(\lambda) = A^2(\lambda) + B(\lambda)C(\lambda)$ is a polynomial in λ. For fixed values of the constants of motion, the spectral curve, $\mu^2 = Q_{h,k}(\lambda)$, defines a Riemann surface. A link between the initial phase space and the Riemann surface can be established from the set $(\tilde{\lambda}, \tilde{\mu})$ where $\tilde{\lambda}$ is a solution of the implicit equation $C(\tilde{\lambda}) = 0$ and $\tilde{\mu}^2 = A(\tilde{\lambda})^2$. [4]

First, note that $\tilde{\lambda}, \tilde{\mu}\colon \mathbb{R}^4 \to \mathbb{C}$ are complex-valued functions that depend on the original variables of the system. The multivalued mapping $\mathcal{L}(q,p) = (\tilde{\lambda}(q,p), \tilde{\mu}(q,p), \mathcal{EM}(q,p))$ is such that $\mathcal{L}\colon \mathbb{R}^4 \to \mathbb{C}^2 \times \mathbb{R}^2$, and we obtain the commutative diagram of Fig. 6.2.

From the definition of $\tilde{\lambda}$ and $\tilde{\mu}$, it is straightforward to deduce that

$$\tilde{\mu}^2 = Q_{h,k}(\tilde{\lambda}). \tag{6.2}$$

Equation (6.2) tells us that the fibers of Φ are contained in Riemann surfaces defined by the same equation as the spectral curve.

Now, we analyze these Riemann surfaces for a fixed value of $(h,k) \neq (h_0,k_0)$ close enough to (h_0,k_0). Using Lemma 5.2, we know that the Riemann surface given by $\tilde{\mu}^2 = Q_{h,k}(\tilde{\lambda})$ is diffeomorphic to the one given by

[4] The set of coordinates $(\tilde{\lambda}, \tilde{\mu})$ is related to a vector bundle that can be defined through the eigenvectors associated with the eigenvalues given by μ [9]. Note also that we can replace C by B everywhere.

the equation $\hat{\mu}^2 = \hat{\lambda}^4 + (2+\hat{h})\hat{\lambda}^2 + \hat{k}\hat{\lambda} + 1$, and from Lemma 5.3 we obtain that this polynomial has four different non-real roots, which are complex conjugate. The Riemann surface is therefore a torus with two points at infinity (see Fig. 6.4).

We assume that the image of the cycle $\mathcal{L}(\gamma)$ under the map $\tilde{\lambda}$ can be deformed (in the complex plane) to a simple loop that goes around two conjugate roots of $Q_{h,k}(\tilde{\lambda})$. This hypothesis can be verified directly for the two examples in Sec. 8. In other words, $\mathcal{L}(\gamma)$ is homotopic on the Riemann surface $\tilde{\mu}^2 = Q_{h,k}(\tilde{\lambda})$ to a cycle, $\tilde{\gamma}$, of the form described in Fig. 6.5.[5]

We consider the one-form ξ on this Riemann surface and, since the value of the integral only depends on the homology class, we obtain

$$\mathcal{I} = \int_{\mathcal{L}(\gamma)} \xi = \int_{\tilde{\gamma}} \xi.$$

Thus,

$$\Delta_\Gamma \mathcal{I} = \int_{\tilde{\gamma}_f} \xi - \int_{\tilde{\gamma}_i} \xi = \int_{\tilde{\gamma}_f - \tilde{\gamma}_i} \xi,$$

where $\tilde{\gamma}_i$ and $\tilde{\gamma}_f$ are the initial and final cycles obtained by turning around the point (h_0, k_0) along Γ.

The cycle $\tilde{\gamma}_f$ can be found by following the transformation of $\tilde{\gamma}_i$ when the constants of motion vary along Γ, and, this transformation is completely determined by the movement of the roots of the polynomial $Q_{h,k}(\tilde{\lambda})$ [75]. It is then enough to analyze the movement of the roots which is given by Lemma 5.3, since F is an orientation preserving local diffeomorphism in the variables (H, K) (Lemma 5.2) and the diffeomorphism in $(\tilde{\lambda}, \tilde{\mu})$ maps the roots of one polynomial to the roots of the new one. Thus, using Lemma 5.3, one obtains the movement of the roots represented in Fig. 6.6. The initial and final cycles are represented on the Riemann surface in Fig. 6.7.

The cycles $\tilde{\gamma}_i$ and $\tilde{\gamma}_f$ are respectively diffeomorphic to the left-hand side and right-hand side cycles in Fig. 6.7. Hence, the chain $\tilde{\gamma}_f - \tilde{\gamma}_i$ is homologous to the chain formed by the two cycles shown in the first torus of Fig. 6.8. We can deform these two cycles as shown in Fig. 6.8 to obtain a positively oriented cycle near $+\infty$.

Let $\tilde{\delta}$ denote this cycle. We get

$$\Delta_\Gamma \mathcal{I} = \int_{\tilde{\delta}} \xi = 2\pi i \operatorname{Res}(\xi, +\infty),$$

[5]Note that it is possible to take the opposite orientation of the cycle giving rise to a change of sign of the integral.

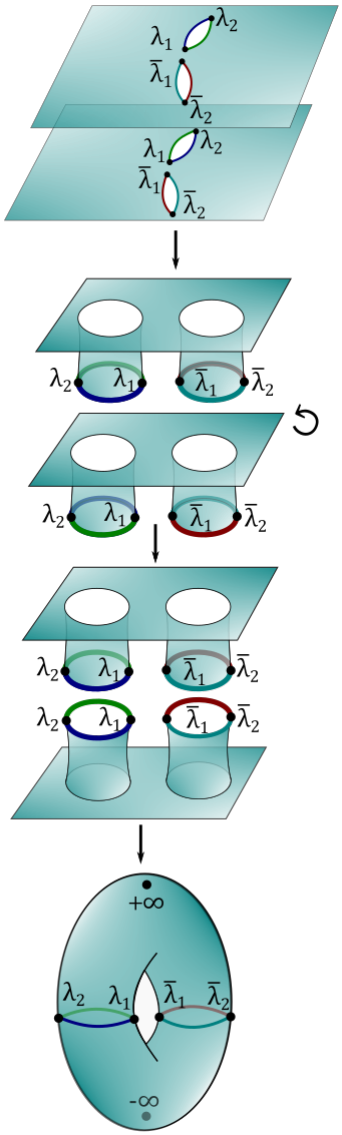

Figure 6.4: The upper panel represents two complex planes where cuts between the roots of the polynomial have been added. The segments with the same color in both planes are identified. Schematically, the Riemann surface can be constructed by performing the different deformations shown in this Figure.

since, by hypothesis, $\xi = c_1 \frac{\tilde{\lambda} d\tilde{\lambda}}{\tilde{\mu}} + c_2 \frac{d\tilde{\lambda}}{\tilde{\mu}}$, where $(c_1, c_2) \in \mathbb{C}^2$. Hence, ξ only has (at most) poles at infinity.

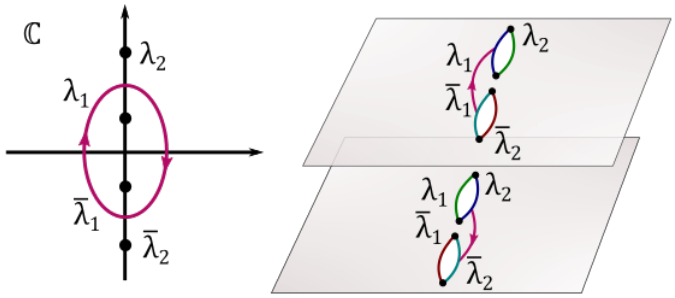

Figure 6.5: Configuration for the normal form with $\hat{k} = 0$, $\hat{h} > 0$. In the complex plane (left-hand side), the cycle is a simple loop that goes around the two conjugate roots λ_1 and $\bar{\lambda}_1$. On the right-hand side, we have the representation of this loop on the Riemann surface.

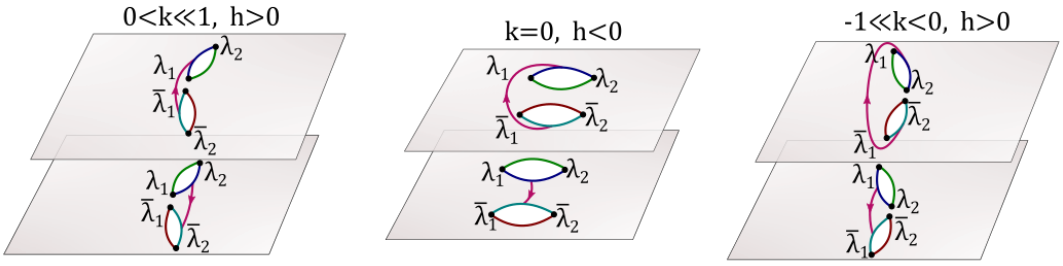

Figure 6.6: For $\hat{k} = 0$ and $\hat{h} > 0$ the roots are purely imaginary. Hence, they are aligned along the imaginary axis. Then, they start rotating counterclockwise until they exchange their positions (pairwise).

Finally, computing $\mathrm{Res}(\xi, +\infty)$, we arrive at

$$\begin{aligned}\mathrm{Res}(\xi, +\infty) &= \mathrm{Res}\left(\frac{c_1 \frac{1}{z} + c_2}{\sqrt{\tilde{Q}(\frac{1}{z})}}(\frac{-1}{z^2})dz, 0\right) \\ &= -\frac{c_1}{\sqrt{a_4}},\end{aligned}$$

where a_4 is the leading coefficient of $Q(\tilde{\lambda})$. □

Proof of Theorem 6.2. By definition of η, we have

$$\int_0^T \dot{\theta} dt = \int_{\mathcal{L}(\gamma)} \frac{\dot{\theta}}{\dot{\tilde{\lambda}}} d\tilde{\lambda} = \int_{\mathcal{L}(\gamma)} \eta.$$

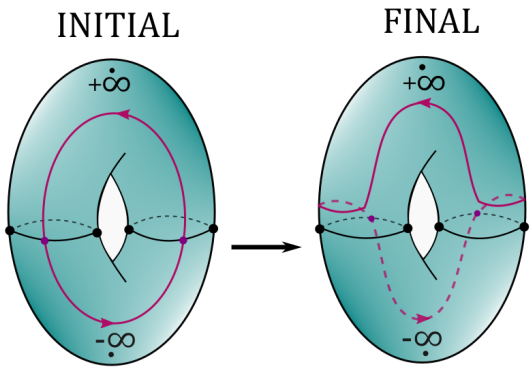

Figure 6.7: Analyzing the movement of the roots (Figure 6.6), we obtain the initial and the final cycles on the Riemann surface.

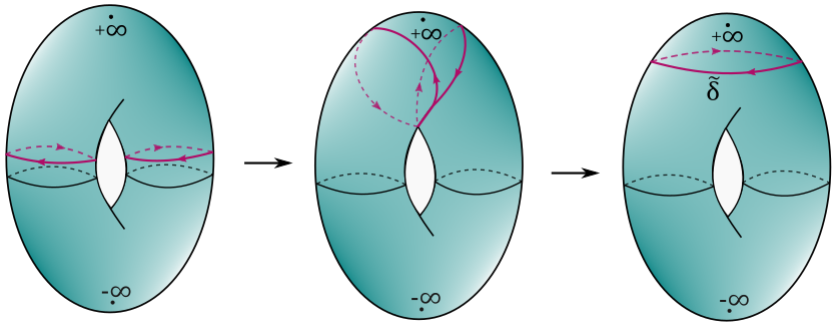

Figure 6.8: Deformation of the two cycles (that are homologous to $\tilde{\gamma}_f - \tilde{\gamma}_f$) into the positively oriented cycle $\tilde{\delta}$ near $+\infty$.

Then, using Theorem 6.1, we obtain that the variation of the rotation number, when the constants of motion vary along Γ, is given by $\Delta_\Gamma \Theta = 2\pi n$.

A basis for the homology group of a regular torus $\mathcal{EM}^{-1}(h,k)$ can be defined as $\{\gamma_K, \gamma_H\}$, where γ_K is the closed orbit of the flow generated by K starting at a point $(q,p) \in \mathcal{EM}^{-1}(h,k)$ and γ_H is the cycle obtained by concatenating γ and the orbit of K between this final point and the initial one (this is equivalent to follow the flow of K for a time $-\Theta$).

Since we have a global $\mathbb{S}^1$-action, the first element of the basis remains the same after a turnaround Γ. The second element, γ_H, transforms into itself plus n-times the cycle γ_K, since $\Delta_\Gamma \Theta = 2\pi n$.

Thus, the Monodromy matrix in the basis described before is

$$\mathbb{M} = \begin{pmatrix} 1 & n \\ 0 & 1 \end{pmatrix}.$$

□

In chapter 8, we present two examples where it can be observed that this result simplifies the calculation of the monodromy matrix. The difficulty of this method is that a spectral Lax pair is needed to obtain the algebraic structure. For many physical systems Lax pairs are known. Nevertheless finding a Lax pair for a given system is not an easy task and there is no general algorithm to derive them.

On the other hand, it is already known that the Hamiltonian monodromy is a local property around the critical point [31]. For this reason, it is natural to try to study it with a local normal form.

In the following chapter we prove that for a system with a local form corresponding to a focus-focus critical point, an approximate Lax pair can be used in a neighborhood of a focus-focus singularity.

Chapter 7

Quasi Lax pair of a system with a focus-focus singularity

In Chapter 8, the method described in the previous chapter is applied to two classical systems whose Lax pairs are known and that have a focus-focus singularity. Another problem related to this later one is to prove, using complex geometry, the non-triviality of the monodromy of any system with a focus-focus singularity.

The major restriction of our method is the fact that there is no algorithm to find a spectral Lax pair for a given physical system and, to the best of my knowledge, there is no known spectral Lax pair for the local model of a focus-focus singularity. For this reason, in this Chapter, we approach the aforementioned problem by introducing the notion of quasi-Lax pair for systems with a focus-focus singularity and show that the monodromy matrix of these systems can be calculated from this new notion.

We call this new notion quasi-Lax pair of the dynamical system because the dynamical equations are only reproduced up to some terms by the Lax equation, where the rest of the terms are negligible in a neighborhood of the focus-focus singularity. Another feature of this Chapter is that the simplicity of the differential equations treated in this case highlights the geometric constructions of the previous Chapter.

We consider a two-degree of freedom system with the coordinates $(a, \bar{a})$ and $(b, \bar{b})$, such that $\{a, \bar{a}\} = \{b, \bar{b}\} = -i$ and the other brackets vanish. The Hamiltonian defined as

$$H = ab + \bar{a}\bar{b}$$

is Liouville-integrable with the constant of motion K given by

$$K = \bar{b}b - a\bar{a}.$$

This system corresponds to a 1:-1 resonant system, which is the non-compact local normal form for dynamics with a single focus-focus point in $a = b = 0$. The nontrivial Monodromy of the Hamiltonian dynamics is e.g. shown in [31, 73] with standard techniques. The Hamiltonian dynamics are governed in a neighborhood V of the focus-focus point by the following differential equations

$$\begin{aligned} \dot{a} &= -i\bar{b};\ \dot{\bar{a}} = ib \\ \dot{b} &= -i\bar{a};\ \dot{\bar{b}} = ia. \end{aligned} \tag{7.1}$$

The quasi-Lax pair is defined by the two matrices L and M given by

$$L = (\lambda^2 + 1 - a\bar{a}/2)\sigma_z + (b\lambda + \bar{a})\sigma_+ + (\bar{b}\lambda + a)\sigma_-$$

and

$$M = \frac{1}{2}(-i\lambda\sigma_z - ib\sigma_+ - i\bar{b}\sigma_-),$$

where we use the Pauli matrices $\sigma_{x,y,z}$ and $\sigma_\pm = \frac{1}{2}(\sigma_x \pm i\sigma_y)$. We find the equations of motion from $\dot{L} = [M, L]$ in which terms of order larger than (or equal to) 3 are neglected.

In this case, we define[1] the spectral curve by $\det(L(\lambda) - \mu\,\mathrm{Id}) = 0$ and the new set of coordinates $(\tilde{\lambda}, \tilde{\mu})$, where $\tilde{\mu} = A(\tilde{\lambda})$ and $\tilde{\lambda}$ is the solution of the implicit equation $C(\lambda) = 0$.

We stress that the spectral curve given by

$$\tilde{\mu}^2 = \tilde{\lambda}^4 + (2 + k)\tilde{\lambda}^2 - h\tilde{\lambda} + 1 - \frac{a^2\bar{a}^2}{4} \tag{7.2}$$

depends on time (not all its coefficients are constants of motion), but if we neglect terms of order larger than three we directly obtain the normal form of the spectral curve derived in Sec. 5.2.

At this level appears the major difficulty in the method proposed in this Chapter: the last term of the right-hand side of Eq. (7.2), $-\frac{a^2\bar{a}^2}{4}$, causes the Riemann surface to be different for each point of the Hamiltonian flow. Even if we still have a torus for each value of a, the image of each point of the Hamiltonian flow under the mapping $(\tilde{\lambda}, \tilde{\mu})$ belongs to a different torus, which is a small perturbation of the one given by the normal form of the spectral curve. This fact makes the use of the spectral curve more difficult.

Nevertheless, since in this section, we consider a local study, in a neighborhood of the focus-focus point, it is not necessary to have all the information provided by the tori described by the variables $(\tilde{\lambda}, \tilde{\mu})$. As we show in

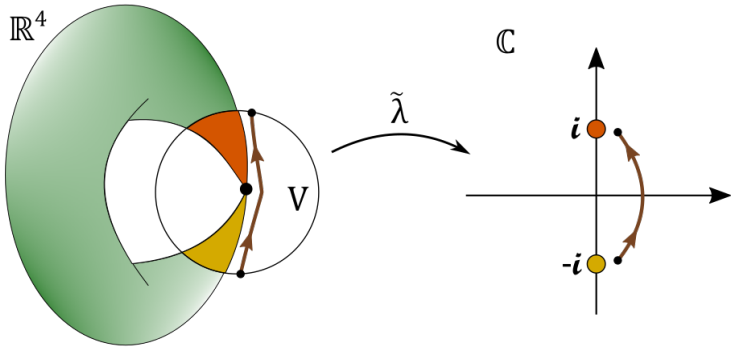

Figure 7.1: Schematic representation of the mapping $\tilde{\lambda}$ in a neighborhood V of the focus-focus point.

this section, it is enough to work with the information given by the variable $\tilde{\lambda} \in \hat{\mathbb{C}}$.

First, notice that the change of variables

$$\tilde{\lambda} = -\frac{a}{\bar{b}},$$
$$\tilde{\mu} = \tilde{\lambda}^2 + 1 - \frac{a\bar{a}}{2},$$

obtained from the quasi-Lax pair, can be applied to derive a new expression of the Liouville two-form. This latter can either be expressed as

$$\Omega = ida \wedge d\bar{a} + idb \wedge d\bar{b}$$

or

$$\Omega = -id\ln(\bar{b}) \wedge dK - \frac{2i}{\tilde{\lambda}} d\tilde{\lambda} \wedge d\tilde{\mu} \tag{7.3}$$

and, using Eq. (7.3), we obtain the one-form $d\theta = -id\ln(\bar{b})$, which leads to $\dot{\theta} = -\tilde{\lambda}$. We also have $\{\tilde{\lambda}, \tilde{\mu}\} = \frac{i}{2}\tilde{\lambda}$ and, using Eq. (7.1), we arrive at

$$\dot{\tilde{\lambda}} = \{\tilde{\lambda}, H\} = i(1 + \tilde{\lambda}^2). \tag{7.4}$$

In order to analyze the monodromy of the system in a small neighborhood[2] V of the focus-focus point, we have to work with relative cycles [31].

[1]Following the idea presented the previous Chapter.

[2]We can consider, e.g., a ball of radius R small enough such that $\|a\|^2 + \|b\|^2 \leq R^2$.

Consider the fiber $\mathcal{EM}^{-1}(h,k)$ for (h,k) sufficiently close to $(0,0)$ so that $\mathcal{EM}^{-1}(h,k)\cap\partial V$ is the disjoint union of two $\mathbb{S}^1$ orbits S_- and S_+. We make the convention that the Hamiltonian flow in the intersection $\mathcal{EM}^{-1}(h,k)\cap V$ (which is homeomorphic to a cylinder) sends points on S_- to S_+. For any point $p\in\mathcal{EM}^{-1}(h,k)\cap V$ let $\gamma_{rel}(p)$ be the part of the orbit of X_H in V that goes through p. Such curve joins a point $p_-\in S_-$ to a point $p_+\in S_+$. (see [31] for details). Then, the rotation number Θ can be expressed as

$$\Theta=\int_{\gamma_{rel}}d\theta=\int_{\tilde{\gamma}_{\text{rel}}}\frac{-\tilde{\lambda}}{i(1+\tilde{\lambda}^2)}d\tilde{\lambda}, \tag{7.5}$$

where $\tilde{\gamma}_{\text{rel}}$ is the image under the mapping $\tilde{\lambda}$ of γ_{rel}. The crucial point is that the 1-form that we integrate only depends on $\tilde{\lambda}$, this makes the information given by this variable sufficient for this local study. Notice that, in this case, we have two branching points that are located in $\pm i$.

The variation of the rotation number is given by

$$\Delta\Theta=\int_{\Delta\tilde{\gamma}_{rel}}\frac{-\tilde{\lambda}}{i(1+\tilde{\lambda}^2)}d\tilde{\lambda}.$$

It is then enough to study the behavior of $\tilde{\lambda}$ over the Hamiltonian flow in V. This behavior is described in Lemma 7.1. First, we integrate Eq. (7.1), obtaining that the Hamiltonian flow in V is given by

$$\begin{aligned}a(t)&=a_0\cosh(t)-i\bar{b}_0\sinh(t)\\ \bar{b}(t)&=\bar{b}_0\cosh(t)+ia_0\sinh(t),\end{aligned}$$

where a_0 and $\bar{b}_0$ are the initial values at $t=0$ of a and $\bar{b}$. The proof of the following Lemma uses these expressions.

Lemma 7.1. The mapping $\tilde{\lambda}$, restricted to V, has the following properties

1. On the singular fiber $\mathcal{EM}^{-1}(0,0)\setminus\{(0,0,0,0)\}$, the function $\tilde{\lambda}$ takes two values i and $-i$ (one on each connected component).

2. In a regular fiber $\mathcal{EM}^{-1}(h,k)$, $\tilde{\lambda}$ does not take the value i nor $-i$ and it is injective on each Hamiltonian trajectory.

3. $\tilde{\lambda}$ is well-defined and continuous on each regular fiber, except for those fibers for which $h=0$ and $k<0$, where $\tilde{\lambda}$ takes the value ∞.[3]

[3]In other words, if we consider $\tilde{\lambda}\colon V\to\hat{\mathbb{C}}$, then it is well defined and continuous on each regular fiber, where $\hat{\mathbb{C}}$ is the Riemann sphere.

4. In a regular fiber $\mathcal{EM}^{-1}(h,k)$, the image of the Hamiltonian flow is a curve that starts and ends near $-i$ and i, respectively. When (h,k) goes to $(0,0)$, the initial and final points converge to $-i$ and i.

Proof. 1. For the singular fiber for which $h = k = 0$, the initial condition $(0,0) \neq (a_0, b_0) \in V$ of the Hamiltonian flow verifies

$$||a_0|| = ||b_0||, \tag{7.6}$$
$$\mathrm{Re}(a_0 b_0) = 0. \tag{7.7}$$

Note that Eq. (7.6) implies that $a_0 \neq 0$ and $b_0 \neq 0$. Using Eq. (7.7), we get $a_0 b_0 = ir$, with $r \in \mathbb{R}$, which, from Eq. (7.6) leads to $\|r\| = \|b_0\|^2$. Since $\bar{b}_0 = \frac{\|b_0\|^2}{b_0}$, we obtain

$$a_0 = \pm i\bar{b}_0,$$

for $\|r\| = \pm r$. We use this relation to compute the image of a solution curve $\varphi(t)$, contained in the singular fiber

$$\begin{aligned}\tilde{\lambda}(\varphi(t)) &= \frac{i\bar{b}_0 \sinh(t) - a_0 \cosh(t)}{\bar{b}_0 \cosh(t) + i a_0 \sinh(t)} \\ &= \frac{i\bar{b}_0 \sinh(t) \mp i\bar{b}_0 \cosh(t)}{\bar{b}_0 \cosh(t) \pm i\bar{b}_0 i \sinh(t)} \\ &= \mp i.\end{aligned}$$

We conclude that $\tilde{\lambda}$ is constant, for the trajectories contained in the singular fiber and that it only takes two values, i (when $a_0 = -i\bar{b}_0$) and $-i$ (when $a_0 = i\bar{b}_0$).

2. (Proof by contradiction) First, let us suppose that there exists a regular fiber $\mathcal{EM}^{-1}(h,k)$ and an initial condition $(a_0, b_0) \in V$ contained in this fiber such that $\tilde{\lambda}(\varphi(a_0, b_0))$ takes the value i or $-i$ for some value of t.

This condition implies that there exists t_1 such that

$$\tilde{\lambda}(\varphi(t_1)) = \frac{-a(t_1)}{\bar{b}(t_1)} = \frac{-a_0 \cosh(t_1) + i\bar{b}_0 \sinh(t_1)}{\bar{b}_0 \cosh(t_1) + i a_0 \sinh(t_1)} = \pm i,$$

equivalently,

$$-a_0 \cosh(t_1) + i\bar{b}_0 \sinh(t_1) = \pm i\bar{b}_0 \cosh(t_1) \pm (-a_0) \sinh(t_1),$$

which implies,

$$\begin{aligned} 0 &= a_0(-\cosh(t_1) \pm \sinh(t_1)) - i\bar{b}_0(-\sinh(t_1) \pm \cosh(t_1) \\ &= (a_0 \pm i\bar{b}_0)(-e^{\mp t_1}). \end{aligned}$$

From the last equation, one gets that: $a_0 \pm i\bar{b}_0 = 0$. Hence, $k = 0$ and $h = 0$, which is a contradiction with the fact that we are considering a regular fiber.

For the second part, let us suppose that $(a_0, b_0) \in V$ is an initial condition contained in a regular fiber $\mathcal{EM}^{-1}(h, k)$ such that, for the corresponding Hamiltonian trajectory φ, there exist t_1 and t_2 with $t_1 \neq t_2$ fulfilling

$$\tilde{\lambda}(\varphi(t_1)) = \tilde{\lambda}(\varphi(t_2)).$$

Equivalently,

$$\frac{-a_0\cosh(t_1) + i\bar{b}_0\sinh(t_1)}{\bar{b}_0\cosh(t_1) + ia_0\sinh(t_1)} = \frac{-a_0\cosh(t_2) + i\bar{b}_0\sinh(t_2)}{\bar{b}_0\cosh(t_2) + ia_0\sinh(t_2)},$$

multiplying by -1 both sides of the equality, we get the following equation

$$\begin{aligned} ia_0^2\cosh(t_1)\sinh(t_2) - i\bar{b}_0^2\sinh(t_1)\cosh(t_2) \\ = ia_0^2\cosh(t_2)\sinh(t_1) - i\bar{b}_0^2\sinh(t_2)\cosh(t_1), \end{aligned}$$

obtaining,

$$\begin{aligned} 0 &= i(a_0^2 + \bar{b}_0^2)(\sinh(t_2)\cosh(t_1) - \sinh(t_1)\cosh(t_2)) \\ &= i(a_0^2 + \bar{b}_0^2)(\sinh(t_2 - t_1)). \end{aligned}$$

Since $t_1 \neq t_2$ we have that $\sinh(t_2 - t_1) \neq 0$. Thus, $a_0^2 + \bar{b}_0^2 = 0$, which implies $k = 0$ and $h = 0$ and this is a contradiction with the fact that we are considering a regular fiber.

3. Recall that the function $\tilde{\lambda}$ is defined as $\tilde{\lambda} = \frac{-a}{\bar{b}}$. Thus, when $b \neq 0$ the function is well-defined and continuous.

   First, notice that $b = 0$ implies $h = 0$, giving that for the fibers $\mathcal{EM}^{-1}(h, k)$ such that $h \neq 0$, b does not vanish on this fiber. Hence, the function $\tilde{\lambda}$ is well-defined and continuous for the fibers $\mathcal{EM}^{-1}(h, k)$ with $h \neq 0$.

   For the regular fibers $\mathcal{EM}^{-1}(h, k)$ such that $h = 0$ we have that $k \neq 0$. By definition, $k = b\bar{b} - a\bar{a}$ which is equivalent to $k = ||b||^2 - ||a||^2$.

Thus, if b vanishes on a given fiber one gets $k < 0$. We conclude that, for $k > 0$, b does not vanish and $\tilde{\lambda}$ is well-defined and continuous on these fibers.

Now, we prove the footnote: for the regular fibers $\mathcal{EM}^{-1}(h, k)$ such that $h = 0$, $k < 0$, let us set $k = -k_0$, with $0 < k_0 \ll 1$, and analyze the function $\tilde{\lambda}$ in the fiber $\mathcal{EM}^{-1}(0, -k_0)$.

Let us first prove that, for every Hamiltonian trajectory on this fiber, there exists a time where the trajectory takes the value $\bar{b} = 0$.

If the initial condition is such that $b_0 = 0$, there is nothing to prove. When the initial condition (a_0, b_0) is such that $b_0 \neq 0$ we have that $\bar{b}_0 \neq 0$ and $a_0 \neq 0$ (because $a_0 = 0$ implies $k > 0$). We study the quotient $\frac{-\bar{b}_0}{ia_0}$. Since $h = 0$ we have that the real part of $a_0 b_0$ vanishes, thus $a_0 b_0 = ir_0$ with $r_0 \in \mathbb{R}$, this implies that $\frac{-\bar{b}_0}{ia_0} = \frac{||b_0||}{r_0} \in \mathbb{R}$. We also have that $k = ||b_0||^2 - ||a_0||^2 = -k_0$, equivalently, $||b_0||^2 = ||a_0||^2 - k_0$ which implies that $||\frac{-\bar{b}_0}{ia_0}||^2 = 1 - \frac{k_0}{||a_0||^2} < 1$. We conclude that $\frac{-\bar{b}_0}{ia_0}$ is a real number of norm less than 1.

We consider $t_1 = \operatorname{arctanh}\left(\frac{-\bar{b}_0}{ia_0}\right)$ and

$$\frac{\bar{b}(t_1)}{\cosh(t_1)} = \bar{b}_0 + ia_0 \tanh(t_1) = \bar{b}_0 + ia_0 \frac{-\bar{b}_0}{ia_0} = 0.$$

Since $\cosh(t)$ does not vanish we conclude that $\bar{b}(t_1) = 0$ which is what we wanted to prove.

We now analyze the behavior of $\tilde{\lambda}$, on this fiber, near the points such that $b = 0$. First notice that $-k_0 = k = ||b||^2 - ||a||^2$ implies $||a||^2 = ||b||^2 + k_0$. Thus, we can consider a point $(a^*, 0)$ in the fiber and obtain

$$\begin{aligned}
\lim_{(a,b)\to(a^*,0)} \|\tilde{\lambda}(a,b)\|^2 &= \lim_{(a,b)\to(a^*,0)} \left\| \frac{-a}{\bar{b}} \right\|^2 \\
&= \lim_{(a,b)\to(a^*,0)} \frac{||b||^2 + k_0}{||b||^2} \\
&= \lim_{(a,b)\to(a^*,0)} \left(1 + \frac{k_0}{||b||^2}\right) = \infty.
\end{aligned}$$

We conclude that the function restricted to this fiber is well-defined and continuous when the codomain of the function is considered to be the Riemann sphere.

4. First notice that

$$\begin{aligned}\tilde{\lambda}(\varphi(t)) &= \frac{i\bar{b}_0 \sinh(t) - a_0 \cosh(t)}{\bar{b}_0 \cosh(t) + i a_0 \sinh(t)} \\ &= \frac{i\bar{b}_0 \tanh(t) - a_0}{\bar{b}_0 + i a_0 \tanh(t)},\end{aligned}$$

and, by definition,

$$\tanh(t) = \frac{e^t - e^{-t}}{e^t + e^{-t}}.$$

Hence, tanh converges exponentially to ± 1 when $t \to \pm\infty$.

From where one gets that

$$\frac{i\bar{b}_0 \sinh(t) - a_0 \cosh(t)}{\bar{b}_0 \cosh(t) + i a_0 \sinh(t)}$$

converge exponentially to $\pm i$ when $t \to \pm\infty$.

On the other hand, when (h, k) goes to $(0, 0)$ the time such that a Hamiltonian trajectory φ, on the fiber $\mathcal{EM}^{-1}(h, k)$, reaches the boundary of V tends to infinity. For this reason, the initial and final points of the image of the trajectories tend to $-i$ and i respectively. □

The mapping $\tilde{\lambda}$ is schematically represented in Fig. 7.1 with $\mathbb{C}$ as codomain and in Fig. 7.2 with $\hat{\mathbb{C}}$ as codomain.

The image of a regular fiber $\mathcal{EM}^{-1}(h, k)$ under $\tilde{\lambda}$ can be described as follows. For $h > 0$ (resp. $h < 0$) and $k = 0$, the image is contained in the left (resp. right) part of the unitary circle. For $k > 0$ (resp. $k < 0$), the norm of the points in the image of the fiber is smaller (resp. larger) than 1. For $h = 0$ and $k > 0$, the image is contained in the imaginary axis between i and $-i$, while it belongs to the imaginary axis outside of the segment between i and $-i$, for $h = 0$ and $k < 0$. We point out that there is no intersection between the different trajectories. Indeed, they are given as solutions of the differential equation $\dot{\lambda} = 1 + \lambda^2$. Hence, by the uniqueness theorem for differential equations, they cannot intersect, unless they coincide, which is not the case.

We now consider a small circle Γ, of radius ρ in the space of parameters (h, k) starting in $h = 0$, $k < 0$, and positively oriented. The previous analysis gives the behavior of $\tilde{\gamma}_{\text{rel}}$, when (h, k) vary along Γ. These results are illustrated numerically in Fig. 7.3.

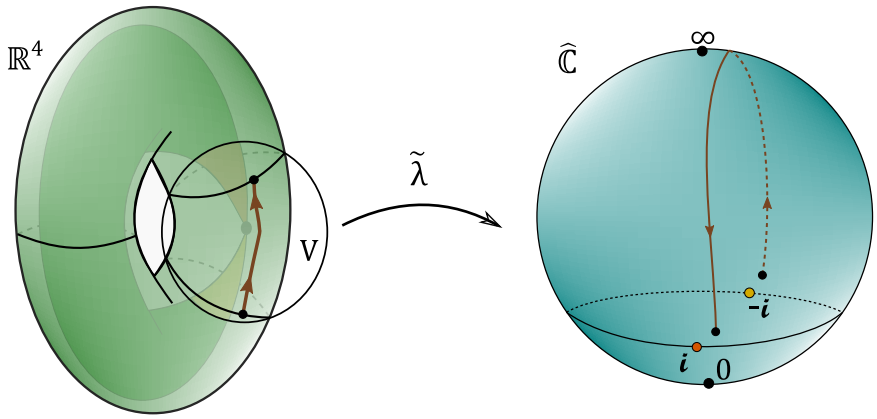

Figure 7.2: Schematic description of the mapping $\tilde{\lambda}$ in a neighborhood V (here a ball) of the focus-focus point. The image of $\tilde{\lambda}$ lies on the Riemann sphere which is the compactification of the complex plane by the stereographic projection.

We have all the tools in hand to compute the variation of the rotation number along Γ

$$\Delta_\Gamma \Theta = \int_{\Delta_\Gamma \tilde{\gamma}_{\rm rel}} \frac{-\tilde{\lambda}}{i(1+\tilde{\lambda}^2)} d\tilde{\lambda}.$$

Note that the one-form has a pole at infinity and, for the value $h = 0$, $k < 0$, $\tilde{\gamma}_{\rm rel}$ goes through this point. For this reason, we parameterize Γ as $h + ik = \rho e^{i\phi}$, with $\phi \in [-\frac{\pi}{2}, \frac{3\pi}{2}]$ and we consider the limit

$$\begin{aligned}\Delta_\Gamma \Theta &= \lim_{\varepsilon \to 0^+} \left(\Theta(\rho e^{i(\frac{3\pi}{2} - \varepsilon)}) - \Theta(\rho e^{i(\frac{-\pi}{2} + \varepsilon)}) \right) \\ &= \lim_{\varepsilon \to 0^+} \left(\int_{\Delta_\varepsilon \Gamma_{rel}} \frac{-\tilde{\lambda}}{i(1+\tilde{\lambda}^2)} d\tilde{\lambda} \right),\end{aligned}$$

where $\Delta_\varepsilon \Gamma_{\rm rel} = \tilde{\gamma}_{\rm rel}(\rho e^{i(\frac{3\pi}{2} - \varepsilon)}) - \tilde{\gamma}_{rel}(\rho e^{i(\frac{-\pi}{2} + \varepsilon)})$.

Let δ_0 be the segment starting and ending respectively at the initial points of $\tilde{\gamma}_{rel}(\rho e^{i(\frac{-\pi}{2} + \varepsilon)})$ and $\tilde{\gamma}_{rel}(\rho e^{i(\frac{3\pi}{2} - \varepsilon)})$ and δ_1 the segment starting and ending respectively at the final points of $\tilde{\gamma}_{rel}(\rho e^{i(\frac{3\pi}{2} - \varepsilon)})$ and $\tilde{\gamma}_{rel}(\rho e^{i(\frac{-\pi}{2} + \varepsilon)})$. The circle Γ in the space (h, k) and the different paths on the Riemann sphere are represented schematically in Fig. 7.4. A numerical plot is given in Fig. 7.5.

The segments δ_0 and δ_1 are contained in the domain of analyticity of the function $\log(1+\tilde{\lambda}^2)$, where log is taken in the $(0, 2\pi)$- branch. This domain

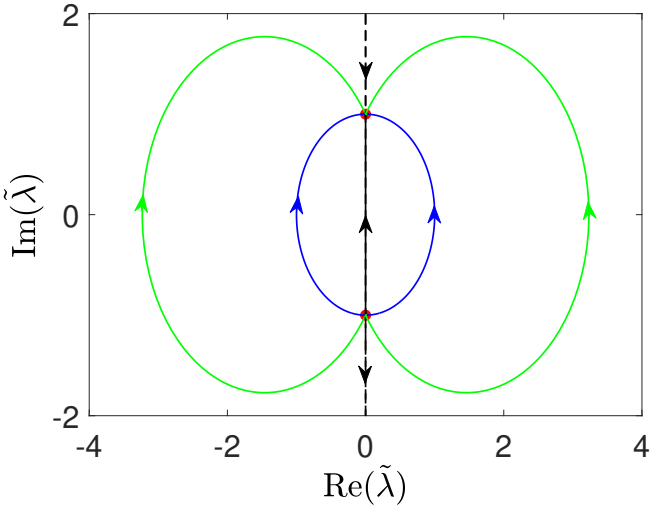

Figure 7.3: Plot of the trajectories in the complex plane of $\tilde{\lambda}$. The red points correspond to $+i$ and $-i$. The blue and green curves represent, respectively, the Hamiltonian flows for $\phi = 0$, π and $\frac{3\pi}{2} - \varepsilon$, $-\frac{\pi}{2} + \varepsilon$. The solid and dashed black lines depict, respectively, the trajectories for $\phi = \frac{\pi}{2}$ and $-\frac{\pi}{2}$. The trajectories converge to the points $\pm i$ when $t \to \pm\infty$. Numerical values are set to $\rho = 0.1$, $a_0 = 0.5$ and $\varepsilon = 0.6$.

is $\mathbb{C} \setminus \mathbb{R} \cup i[-1, 1]$. We have

$$\lim_{\varepsilon \to 0^+} \left(\int_{\delta_j} \frac{-\tilde{\lambda}}{i(1+\tilde{\lambda}^2)} d\tilde{\lambda} \right) = 0,$$

with $j = 0, 1$. Using this result, we obtain

$$\Delta_\Gamma \Theta = \lim_{\varepsilon \to 0^+} \left(\int_{\delta_\varepsilon} \frac{-\tilde{\lambda}}{i(1+\tilde{\lambda}^2)} d\tilde{\lambda} \right),$$

where δ_ε is $\tilde{\gamma}_{rel}(\rho e^{i(\frac{3\pi}{2} - \varepsilon)}) * \delta_1 * -\tilde{\gamma}_{rel}(\rho e^{i(\frac{-\pi}{2} + \varepsilon)}) * \delta_0$, $*$ corresponding to the concatenation of paths.

Finally, we get for $\varepsilon > 0$

$$\begin{aligned} \int_{\delta_\varepsilon} \frac{-\tilde{\lambda}}{i(1+\tilde{\lambda}^2)} d\tilde{\lambda} &= 2\pi i \times \text{Res} \left(\frac{-\tilde{\lambda}}{i(1+\tilde{\lambda}^2)} d\tilde{\lambda}, \tilde{\lambda} = \infty \right) \\ &= 2\pi, \end{aligned}$$

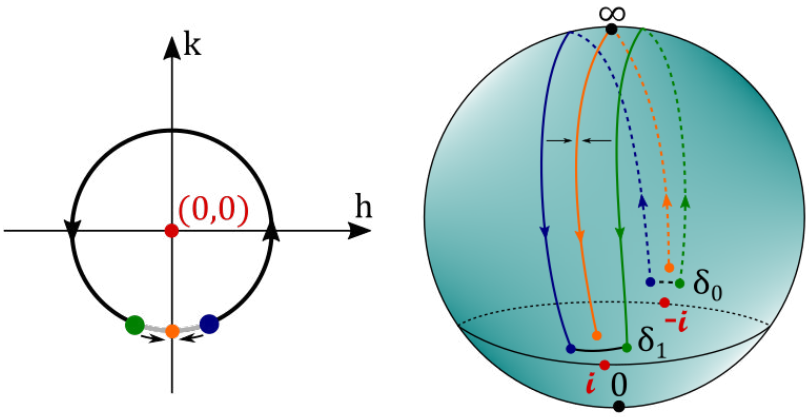

Figure 7.4: The left panel depicts the loop Γ in the space (h, k). The position of the blue, green, yellow and red points are respectively $\rho e^{i(-\frac{\pi}{2}+\varepsilon)}$, $\rho e^{i(\frac{3\pi}{2}-\varepsilon)}$, $\rho e^{\frac{3i\pi}{2}}$ and 0. The corresponding trajectories are represented schematically on the Riemann sphere in the right panel, with the same color code. The segments δ_0 and δ_1 joining respectively the initial and final points of the trajectories are also plotted (see the text for details).

which leads to

$$\Delta_\Gamma \Theta = \lim_{\varepsilon \to 0^+} (2\pi) = 2\pi.$$

We conclude that the monodromy matrix of any system with a focus-focus singularity can be computed from this complex approach using quasi-Lax pairs and the corresponding change of variables defined by $\tilde{\lambda}$ and $\tilde{\mu}$.

Through the analysis of the complex geometry of a Riemann surface given by the Lax pair of a Hamiltonian system, we have shown that Hamiltonian monodromy can be completely described by the properties of this surface defined by a polynomial of degree four. More precisely, the monodromy matrix can be computed from a meromorphic form of this surface with a pole at infinity. The general approach is illustrated by two relevant examples, namely the Jaynes-Cumming model and the spherical pendulum, for which a Lax pair is known in the next Chapter.

However, the main weak point of this method is the need to know a Lax pair. This description has been achieved only for a few integrable systems, while Hamiltonian monodromy and its generalizations appear generically in such systems, for instance in any system with a focus-focus singularity. We proposed, in this Chapter, to answer this question by deriving a quasi-Lax pair in a small neighborhood of the singularity, which allows us to apply, with some adaptations, the general results of this study. This idea originates

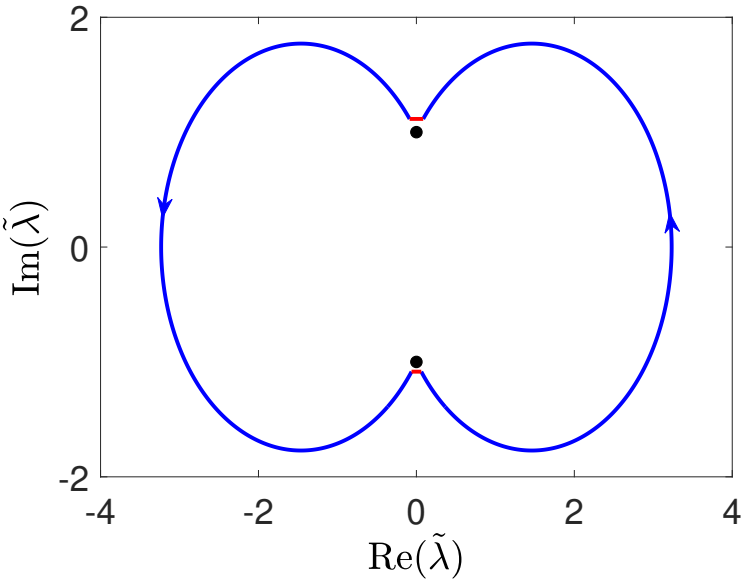

Figure 7.5: Plot of the cycle δ_ε. The relative cycles and the segments δ_0, δ_1 are, respectively, represented in blue and red. The black dots correspond to $\pm i$. Numerical values are set to $\rho = 0.1$, $a_0 = 0.4$ and $\varepsilon = 0.6$. The neighborhood V is a ball of radius 1.

from the fact that Hamiltonian monodromy is a local phenomenon that does not depend on the global Hamiltonian dynamics. Thus, we think that the notion of quasi-Lax pair will be a valuable tool in the study of Hamiltonian systems with singularities.

Chapter 8

Physical Examples

In this Chapter, we present two relevant examples of this theory. The first example is the James-Cummings model whose relevance comes from the fact that it is the classical limit of an important system in quantum optics. The second example is the spherical pendulum which is the most representative example of Hamiltonian monodromy, since it was the first example for which the non-triviality of the Hamiltonian monodromy was proved. We show, using these two examples, that the computation of the monodromy matrix is relatively simple using the Lax pair method.

8.1 The Jaynes-Cummings model

As a first example, we consider the classical Jaynes-Cummings model (JC). Its quantum counterpart has been widely studied as a basic model system in quantum optics [27, 39] describing the interaction of a two-level quantum system with a quantized mode of an optical cavity [60]. The global dynamics of the classical version have been recently explored in a series of papers showing, in particular, the possible non-trivial monodromy of this integrable system [10, 11, 57, 12, 40, 2].

The classical JC describes the interaction of a classical spin coupled to a Harmonic oscillator on the phase space $\mathbb{S}^2 \times \mathbb{R}^2$. The Hamiltonian of the system can be expressed as

$$H = 2\omega_0 S_z + \omega \bar{b} b + g(\bar{b} S_- + b S_+), \tag{8.1}$$

where ω_0, ω, and g are real constants representing respectively the frequencies of the spin and of the Harmonic oscillator and the coupling strength between the two sub-systems. The coordinates describing the spin and the Harmonic oscillator are denoted by (S_x, S_y, S_z) and $(b, \bar{b})$, respectively, with

the constraint $S_x^2 + S_y^2 + S_z^2 = S_0^2$, where S_0 is a positive constant. To simplify the description, we also introduce the components S_+ and S_-, given by

$$S_+ = S_x + iS_y$$
$$S_- = S_x - iS_y.$$

The spin dynamics is obtained from the following Poisson bracket

$$\{S_a, S_b\} = \varepsilon_{abc} S_c,$$

where ε_{abc} is the completely anti-symmetric tensor with indices a, b and c belonging to the set $\{x, y, z\}$. Note that

$$\{S_\pm, S_z\} = \pm iS_\pm$$
$$\{S_+, S_-\} = -2iS_z.$$

For the Harmonic oscillator, we have $\{b, \bar{b}\} = -i$, which can be deduced from $b = \frac{1}{\sqrt{2}}(q + ip)$ and $\bar{b} = \frac{1}{\sqrt{2}}(q - ip)$ and the relation $\{q, p\} = 1$, where q and p are the real position and momentum of the oscillator.

The Hamiltonian H defines a completely integrable dynamics on the phase space of dimension four. The second constant of motion, K, can be written as $K = S_z + \bar{b}b$ and verifies $\{K, H\} = 0$. The Hamiltonian dynamics are then governed by the following differential equations

$$\begin{aligned} \dot{S}_+ &= \{S_+, H\} = 2i\omega_0 S_+ - 2ig\bar{b}S_z \\ \dot{S}_z &= ig\bar{b}S_- - igbS_+ \\ \dot{b} &= -i\omega b - igS_-. \end{aligned} \tag{8.2}$$

A standard computation of the bifurcation diagram [11] shows that this system has a focus-focus singularity for some values of the parameters, and thus a non-trivial monodromy around this point. The corresponding isolated singular value of the bifurcation diagram has the coordinates $(h_0, k_0) = (2\omega_0 S_0, S_0)$. Note that the dynamics has another fixed point on the fiber $(-2\omega_0 S_0, -S_0)$. Figure 8.1 displays the bifurcation diagram, for a specific set of parameters.

The Lax Pair approach

We now describe the dynamics by using Lax pairs. We consider the Lax matrices L and M defined by

$$L(\lambda) = \begin{pmatrix} \frac{(2\lambda-\omega)(\lambda-\omega_0)+g^2 S_z}{g^2} & \frac{2b(\lambda-\omega_0)}{g} + S_- \\ \frac{2\bar{b}(\lambda-\omega_0)}{g} + S_+ & \frac{(\omega-2\lambda)(\lambda-\omega_0)-g^2 S_z}{g^2} \end{pmatrix}$$

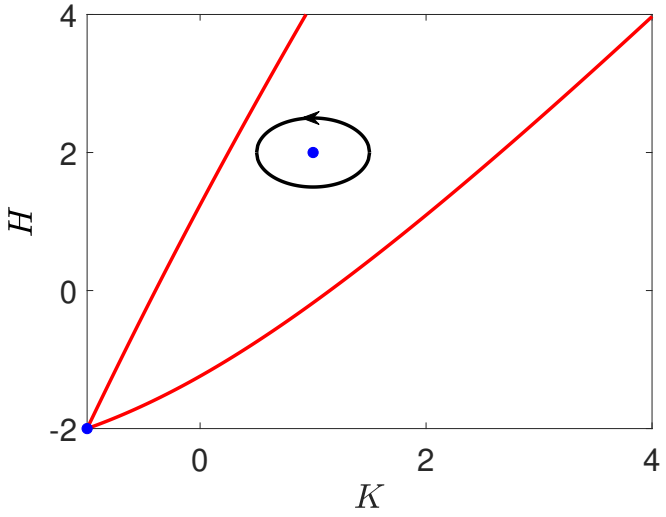

Figure 8.1: Plot of the JC bifurcation diagram. Numerical parameters are set to $S_0 = 1$, $\omega_0 = 1$, $\omega = 2$ and $g = 1$. The points, for which $d\mathcal{EM}$ has rank 0 and 1, are respectively plotted in blue and red. The blue points have the coordinates $(S_0, 2\omega_0 S_0)$ and $(-S_0, -2\omega_0 S_0)$. A loop around the focus-focus point is displayed in black.

and

$$M(\lambda) = \begin{pmatrix} -i\lambda & -igb \\ -ig\bar{b} & i\lambda \end{pmatrix}.$$

The matrix L has the form described by Eq. (6.1). The Lax equation reads

$$\dot{L}(\lambda) = [M(\lambda), L(\lambda)],$$

and is equivalent to Eq. (8.2). The spectral curve is given by

$$\mu^2 = A^2 + BC = Q(\lambda), \tag{8.3}$$

where $Q(\lambda)$ is a polynomial of order four in λ, which can be expressed as

$$\begin{aligned} Q(\lambda) = &\frac{(2\lambda - \omega)^2}{g^4}(\lambda - \omega_0)^2 + \frac{4}{g^2}K(\lambda - \omega_0)^2 \\ &+ \frac{2}{g^2}(H - \omega K)(\lambda - \omega_0) + S_0^2. \end{aligned}$$

As mentioned in the general case, it can be verified that all the coefficients of the polynomial are constants of the motion. The movement of the roots

along a loop in the bifurcation diagram can be computed numerically. To this aim, we consider a loop defined by $k = k_0 + r\cos(\chi)$ and $h = h_0 + r\sin(\chi)$, with $r = 0.5$ and $\chi \in [0, 2\pi]$. We denote by χ_c the angle defined by $\chi_c = \pi + \arctan(2\omega_0)$, which leads to the point $(h_c = h_0 + r\sin(\chi_c), k_c = k_0 + r\cos(\chi_c)$. The roots for this specific loop are displayed in Fig. 8.2.

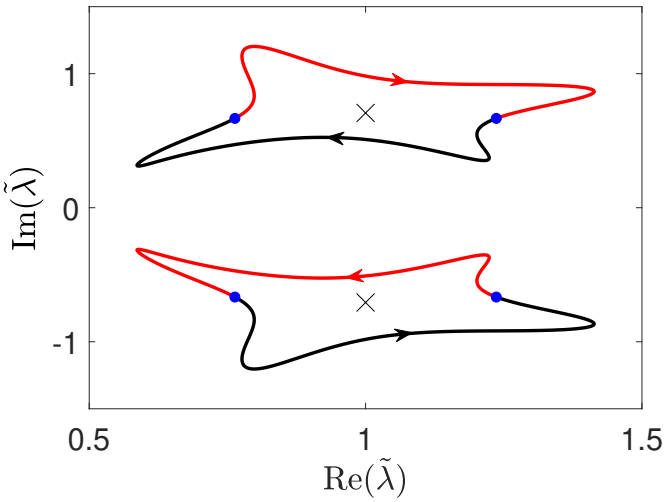

Figure 8.2: Plot of the movement of the roots of the polynomial Q along the loop of Fig. 8.1. Numerical parameters are set to $S_0 = 1$, $\omega_0 = 1$, $\omega = 2$ and $g = 1$. The crosses correspond to (k_0, h_0) and the blue points to (k_c, h_c).

The Hamiltonian dynamics on this surface are obtained from the functions $(\tilde{\lambda}, \tilde{\mu})$. We recall that $\tilde{\lambda}$ is the solution of the implicit equation $C(\lambda) = 0$ and $\tilde{\mu} = A(\tilde{\lambda})$. We deduce that

$$\begin{aligned} \tilde{\lambda} &= \omega_0 - \frac{g}{2}\frac{S_+}{\bar{b}}, \\ \tilde{\mu} &= \left(\frac{\omega - 2\omega_0}{2g}\right)\frac{S_+}{\bar{b}} + \frac{S_+^2}{2\bar{b}^2} + S_z. \end{aligned} \tag{8.4}$$

It is then straightforward to verify that

$$\{\tilde{\lambda}, \tilde{\mu}\} = \{-\frac{gS_+}{2\bar{b}}, S_z\} = i(\tilde{\lambda} - \omega_0)$$

and $\{\tilde{\lambda}, K\} = 0$, $\{\tilde{\mu}, K\} = 0$, *i.e.*, $\tilde{\lambda}$ and $\tilde{\mu}$ are coordinates of the reduced phase space. Figure 8.3 illustrates numerically the Hamiltonian trajectory on the Riemann surface. This loop can be derived either using the

Hamiltonian flow in the original coordinates, given by Eq. (8.2) and the relations (8.4), or by using the Riemann surface (8.3). In this latter case, we have

$$\dot{\tilde{\lambda}} = \{\tilde{\lambda}, H\} = \frac{g^2}{2(\tilde{\lambda} - \omega_0)}\{\tilde{\lambda}, \tilde{\mu}^2\} = ig^2\tilde{\mu},$$

which leads to

$$\dot{\tilde{\lambda}} = ig^2\sqrt{Q(\tilde{\lambda})}.$$

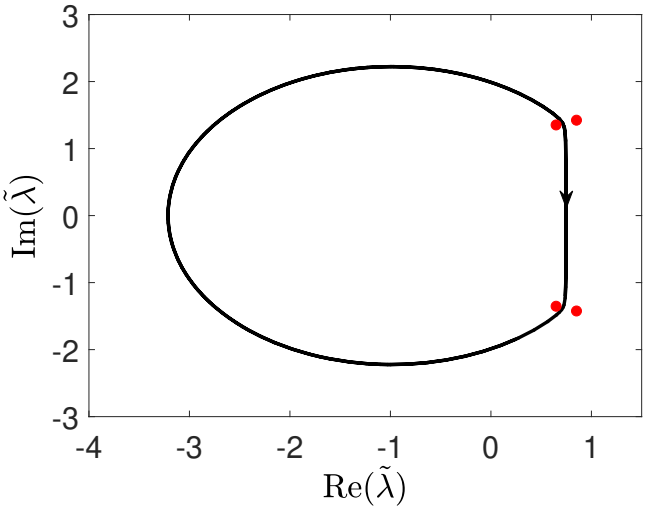

Figure 8.3: Plot of the image of the Hamiltonian flow under $\tilde{\lambda}$, for $k_1 = k_0 - 0.01$ and $h_1 = h_0$. The red points correspond to the position of the branch points of the Riemann surface.

The normal form

The next step of our general approach consists of analyzing the polynomial $Q_{h,k}(\tilde{\lambda})$ around the point (h_0, k_0) in the bifurcation diagram. Since $Q \in \mathbb{R}[\tilde{\lambda}]$, we have $\overline{Q(\tilde{\lambda})} = Q(\bar{\tilde{\lambda}})$, which implies that the roots of $Q_{k,h}$ are pairwise complex conjugate. We first compute $Q_{h_0,k_0}(\tilde{\lambda})$ and its roots:

$$\begin{aligned} Q_{h_0,k_0}(\tilde{\lambda}) &= \left(\frac{(2\tilde{\lambda} - \omega)(\tilde{\lambda} - \omega_0)}{g^2} + S_0\right)^2 \\ &= \frac{4}{g^4}\left(\tilde{\lambda}^2 - \frac{2\omega_0 + \omega}{2}\tilde{\lambda} + \frac{\omega_0\omega + g^2 S_0}{2}\right)^2. \end{aligned}$$

Since this polynomial has conjugate roots, we also have

$$\begin{aligned} Q_{h_0,k_0}(\tilde{\lambda}) &= \frac{4}{g^4}((\tilde{\lambda}-\lambda_0)(\tilde{\lambda}-\bar{\lambda}_0))^2 \\ &= \frac{4}{g^4}(\tilde{\lambda}^2 - 2\mathrm{Re}\,(\lambda_0)\tilde{\lambda} + ||\lambda_0||^2)^2, \end{aligned}$$

and we arrive at

$$\begin{aligned} \mathrm{Re}\,(\lambda_0) &= \frac{2\omega_0+\omega}{4} \\ \mathrm{Im}\,(\lambda_0) &= \left(\frac{g^2 S_0}{2} - \left(\frac{\omega-2\omega_0}{4}\right)^2\right)^{\frac{1}{2}}. \end{aligned}$$

Then, we apply the general procedure described in Sec. 5 to transform this polynomial to the one of the normal form. We have:

$$\begin{aligned} &Q_{h,k}(\tilde{\lambda}) = \frac{4}{g^4}\tilde{\lambda}^4 - \frac{4}{g^4}(\omega+2\omega_0)\tilde{\lambda}^3 \\ &+\frac{4}{g^4}((\omega_0+\frac{\omega}{2})^2 + \omega\omega_0 + g^2 k)\tilde{\lambda}^2 \\ &-\frac{4}{g^4}(\omega\omega_0(\omega_0+\frac{\omega}{2}) + \frac{g^2}{2}(k(\omega+4\omega_0)-h))\tilde{\lambda} \\ &+\frac{4}{g^4}(\frac{\omega^2\omega_0^2}{4} + \frac{g^4 S_0^2}{4} + \frac{\omega_0 g^2}{2}(k(\omega+2\omega_0)-h)). \end{aligned}$$

From a direct calculation, we obtain that the derivative at (h_0, k_0) of the transformation F defined in Lemma 5.2 has the following form

$$D = \begin{pmatrix} \frac{g^2(\omega_0 - \mathrm{Re}(\lambda_0))}{2\mathrm{Im}(\lambda_0)^4} & \frac{g^2(s)}{2\mathrm{Im}(\lambda_0)^4} \\ \frac{g^2}{2\mathrm{Im}(\lambda_0)^3} & \frac{g^2(2-(\omega+4\omega_0))}{2\mathrm{Im}(\lambda_0)^3} \end{pmatrix},$$

where

$$s = 2\mathrm{Im}(\lambda_0)^2 - 2\mathrm{Re}(\lambda_0)^2 + \mathrm{Re}(\lambda_0)(\omega+4\omega_0) - \omega_0(\omega+2\omega_0).$$

The determinant of the matrix D is

$$\begin{aligned} &\det(D) = \frac{g^4}{4\mathrm{Im}(\lambda_0)^7}(-\mathrm{Im}(\lambda_0)^2 + 2\mathrm{Re}(\lambda_0)^2 \\ &-\mathrm{Re}(\lambda_0)(\omega+4\omega_0) + \omega_0(\omega+2\omega_0) \\ &+(\omega_0 - \mathrm{Re}(\lambda_0))(2-(\omega+4\omega_0))). \end{aligned}$$

Substituting the values of $\mathrm{Re}(\lambda_0)$ and $\mathrm{Im}(\lambda_0)$, we obtain

$$\det D = \frac{g^4(-g^2 S_0 - \frac{\omega_0^2}{2} - \frac{\omega}{2} + \frac{\omega^2}{4} + \omega_0)}{4\mathrm{Im}(\lambda_0)^7}.$$

If $\det D \neq 0$, then Q can be transformed to the normal form polynomial.

Hamiltonian Monodromy

We have now all the tools in hand to compute the monodromy matrix. The angle θ conjugate to K verifies $\{\theta, K\} = 1$ and $\{\theta, \tilde{\lambda}\} = \{\theta, \tilde{\mu}\} = 0$. Using Eq. (8.3), we have

$$\dot{\theta} = \{\theta, H\} = \{\theta, -2K(\tilde{\lambda} - \omega_0) + \omega K\},$$

which gives

$$\dot{\theta} = \omega + 2\omega_0 - 2\tilde{\lambda}$$

and we obtain the following expression for the one-form $d\theta$, as a function of $\tilde{\lambda}$ and $\tilde{\mu}$

$$d\theta = \frac{((\omega + 2\omega_0) - 2\tilde{\lambda})d\tilde{\lambda}}{ig^2\tilde{\mu}}. \tag{8.5}$$

From Eq. (8.5), it is clear that $d\theta$ is of the form described in Theorem 6.1. We deduce that the residue of this form at infinity is equal to $\frac{2}{ig^2}$ divided by the square root of the leading coefficient of the polynomial Q, *i.e.*,

$$\frac{\frac{2}{ig^2}}{\sqrt{\frac{4}{g^4}}} = \frac{2g^2}{2g^2 i} = \frac{1}{i}.$$

Finally, using Theorem 6.2, we obtain that the monodromy matrix is

$$\mathbb{M} = \begin{pmatrix} 1 & 1 \\ 0 & 1 \end{pmatrix}.$$

8.2 The spherical pendulum

As a second example, we consider the historical system for which a non-trivial monodromy was for the first time highlighted [28], namely the spherical pendulum. Since then, this system has been extensively studied both from classical and quantum point of view [23, 35, 22, 15, 8, 30]. The corresponding Lax pair has been described in [8, 32]. The spherical pendulum consists of a mass moving without friction on a sphere. The dynamics are governed on the phase space TS^2 by the following Hamiltonian expressed in dimensionless coordinates [22]:

$$H = \frac{1}{2}(p_x^2 + p_y^2 + p_z^2) + z,$$

with the constraints $x^2+y^2+z^2 = 1$ and $xp_x+yp_y+zp_z = 0$. The dynamical equations can be expressed as

$$\begin{aligned}\dot{\vec{q}} &= \vec{p}\\ \dot{\vec{p}} &= \vec{e}_z - (p_x^2 + p_y^2 + p_z^2 - z)\vec{q},\end{aligned}$$

where $\vec{e}_z = (0, 0, -1)$ is a unit vector along the z- direction. We introduce the angular momentum $\vec{K} = \vec{q} \times \vec{p}$, with $\dot{\vec{K}} = \vec{q} \times \vec{e}_z$. We deduce that the system is completely integrable, since it has a second constant of motion, $K = K_z$, such that $\{H, K\} = 0$. It can be shown that the spherical pendulum has a non-trivial Monodromy, due to a focus-focus singularity corresponding to the point $(h_0, k_0) = (1, 0)$ of the bifurcation diagram [22, 30].

The Lax Pair approach

With the coordinates (L_x, L_y, L_z) and (M_x, M_y, M_z) defined as

$$\begin{aligned}L_x &= x - \lambda K_x,\\ L_y &= y - \lambda K_y,\\ L_z &= z - \lambda K_z + \lambda^2.\end{aligned}$$

and

$$\begin{aligned}M_x &= K_x,\\ M_y &= K_y,\\ M_z &= K_z - \lambda,\end{aligned}$$

the Lax matrices L and M, which satisfy $\dot{L} = [M, L]$, can then be expressed as:

$$L = L_x\sigma_x + L_y\sigma_y + L_z\sigma_z$$
$$M = \frac{-i}{2}(M_x\sigma_x + M_y\sigma_y + M_z\sigma_z),$$

where σ_x, σ_y, and σ_z are the Pauli matrices.

The spectral curve is given by the eigenvalues of L

$$\mu^2 = L_x^2 + L_y^2 + L_z^2.$$

A straightforward computation leads to

$$\mu^2 = \lambda^4 - 2K\lambda^3 + 2H\lambda^2 + 1. \tag{8.6}$$

We have

$$A(\lambda) = L_z$$
$$C(\lambda) = L_x - iL_y$$

and we deduce that

$$\tilde{\lambda} = \frac{x + iy}{K_x + iK_y}$$

and

$$\tilde{\mu} = A(\tilde{\lambda}) = z - \tilde{\lambda}K_z + \tilde{\lambda}^2.$$

As expected, it can be verified that

$$\{\tilde{\lambda}, K\} = \{\tilde{\mu}, K\} = 0.$$

Using $\{K_x, z\} = -y$ and $\{K_y, z\} = x$, we get

$$\{\tilde{\lambda}, \tilde{\mu}\} = \{\tilde{\lambda}, z\} = -i\tilde{\lambda}^2.$$

Finally, from Eq. (8.6), we arrive at

$$\dot{\tilde{\lambda}} = \{\tilde{\lambda}, H\} = \frac{\tilde{\mu}}{\tilde{\lambda}^2}\{\tilde{\lambda}, \tilde{\mu}\} = -i\tilde{\mu}.$$

The normal form

As in the JC model, we apply the procedure described in Sec. 5.2 to transform the polynomial

$$Q_{h,k}(\tilde{\lambda}) = \tilde{\lambda}^4 - 2k\tilde{\lambda}^3 + 2h\tilde{\lambda}^2 + 1$$

to the normal form polynomial. The polynomial $Q_{h_0,k_0}(\tilde{\lambda})$ given by

$$Q_{h_0,k_0}(\tilde{\lambda}) = \tilde{\lambda}^4 + 2\tilde{\lambda}^2 + 1,$$

has the roots $\pm i$. Following Lemma 5.2, we obtain that the derivative at (h_0, k_0) of the transformation F is

$$D = \begin{pmatrix} 0 & 2 \\ 2 & 0 \end{pmatrix}.$$

Since $\det D \neq 0$, the polynomial Q can be transformed to the normal form.

Hamiltonian Monodromy

The last step to compute the monodromy matrix consists of expressing the one-form $d\theta$ in the coordinates $(\tilde{\lambda}, \tilde{\mu})$. The angle θ conjugate to K verifies $\{\theta, K\} = 1$ and $\{\theta, \tilde{\lambda}\} = \{\theta, \tilde{\mu}\} = 0$. Starting from Eq. (8.6), we deduce that

$$\dot{\theta} = \{\theta, H\} = \tilde{\lambda}.$$

Finally, we arrive at

$$d\theta = \dot{\theta}\frac{d\tilde{\lambda}}{\dot{\tilde{\lambda}}} = i\frac{\tilde{\lambda}d\tilde{\lambda}}{\tilde{\mu}}. \tag{8.7}$$

The one-form given in Eq. (8.7) corresponds to the expression described in Theorem 6.1 and its residue at infinity is equal to $-i = \frac{1}{i}$. Using Theorem 6.2, we conclude that the Hamiltonian monodromy matrix is

$$\mathbb{M} = \begin{pmatrix} 1 & 1 \\ 0 & 1 \end{pmatrix}.$$

Part III

Conclusions

Chapter 9

General Conclusions

In this thesis, two main topics have been treated, namely, rotating rigid body dynamics and Hamiltonian monodromy. Throughout the different chapters of this work, these problems were developed and the necessary concepts were introduced. We now give a summary of the different results obtained as a general conclusion. Details are given in the referred chapters.

In Chapter 2, we proved a result (Th. 2.1) that ensures the existence and robustness (with respect to c) of the tennis racket effect (TRE) in a neighborhood of the separatrix in the region $|\beta| < |u|$. For the region $u < |\beta|$, we find that the asymptotic behavior of the function $F_{a,b,c}(u)$ describing the tennis racket effect is completely different from the asymptotic behavior in the region $|\beta| < |u|$, since $F_{a,b,c}(u)$ has a logarithmic behavior in the variable u in the region $|\beta| < |u|$ and a square root behavior in the region $u < |\beta|$. These two regions are found using the fact that the abelian integral defining $F_{a,b,c}(u)$ has a different multivaluated character in these two regions.

For the Dhzanibekov effect we found, under certain hypotheses on the parameters a and b, an approximation of the variation of the angle ϕ as a function of the distance to the separatrix c. This allows us to predict, with good accuracy [48], the number of rotations necessary (given the initial condition c) to observe the π-flip of the wing nut.

On the other hand, recall that the monster flip is intended to avoid any extra rotation when the skateboard performs a full turn along the intermediate axis of the skateboard. Since the tennis racket effect predicts a π-flip in the transverse axis of the skateboard, to describe this trick, it is necessary to find an approximation of this possible extra rotation for a given initial condition. Thus, for the monster flip, we give an approximation of this possible rotation, under conditions on the parameters a and b, and, assuming that the corresponding rotation angle is small, we see that this imposes a strong constraint on these parameters.

In Chapter 3, for an asymmetric rigid body such that $I_z < I_y < I_x$, we search for the signatures of the physical constraint $I_y + I_z \geq I_x$. We define the physical case when the moments of inertia fulfill this inequality and the non-physical case otherwise. In this chapter, we study the tennis racket effect from a new perspective by investigating the pairs (c, ε) that describe the tennis racket effect ($2\pi = \Delta\phi = F_{a,b}(c, \varepsilon)$) and taking into account the physical constraint. We prove that these pairs describe a curve, $\mathcal{C}$, which turns out to be injective in the physical case and non-injective in the non-physical case. As part of the mathematical framework that leads to these results, we introduce implicit equations describing this curve that allow us to perform a quantitative analysis. We take advantage of this description of the tennis racket effect to prove that the TRE on the separatrix always exists and to give conditions under which a perfect TRE is observed. For the Montgomery phase, we detect the signature of the physical constraint on oscillating trajectories. We show (Th. 3.14) that the Montgomery phase is greater than or equal to 2π in the physical case and is less than 2π in the non-physical case. Moreover, for rotating trajectories, we find the infimum of the values of the Montgomery phase along these trajectories. Finally, we take advantage of the analysis done for the Montgomery phase for rotating trajectories to give a result about the existence of the Dhzanibekov effect with a given value α of the rotation angle required to observe the flip of the wing nut. It turns out that in this case, for rotating trajectories, we also find a minimum possible value of α given by $\frac{1}{2}$ of the minimum value of the Montgomery phase, which implies that if α is smaller than this value, it is not possible to observe the Dhzanibekov effect for this given angle.

In Chapter 4 we present introductory material and, in Chapter 5, auxiliary results are obtained. In Chapter 6, we study the Hamiltonian monodromy of two degrees of freedom systems in $\mathbb{R}^4$ with a globally defined $\mathbb{S}^1$-action which is described by a spectral Lax pair. This analysis is done around an isolated critical value of the energy-momentum map (H, K), where H is the total energy of the system and K is the first integral defined by the $\mathbb{S}^1$-action. Using the spectral Lax pair of the system, we derive a Riemann surface with the property that the variation of the rotation number $\Delta\Theta$ boils down to the computation of a residue at infinity of a meromorphic 1-form defined on this Riemann surface. Moreover, we give an explicit expression of this residue (Th. 6.1, Th. 6.2). We show in Chapter 8, that these results simplify the computations of the monodromy matrix in two relevant examples in physics, namely, the spherical pendulum and the Jaynes-Cummings model.

Since the spectral Lax pair is not known for all completely integrable systems, in Chapter 7, we introduce what we call a quasi-Lax pair, which is

an approximate Lax pair obtained by neglecting high-order terms. In this chapter, we proved that for systems with a focus-focus singularity, this tool allows to calculate the monodromy matrix for this type of system using the Lax pair approach.

Finally, in Appendix A, we briefly describe three problems that could be solved in the near future with the tools introduced in this thesis. One problem is to study the equations of the rigid body with a rotor. The second one is the study of a generalization of the Jaynes-Cummings model called the Tavis-Cummings model. The third problem links Part 1 and Part 2, and the goal is to find a connection between Hamiltonian monodromy and the Montgomery phase.

Appendix A

Perspectives

Throughout this thesis, we have tackled different physical problems using complex foliations tools. This approach invites the study of physical problems from this perspective. This appendix is dedicated to the description of physical problems that could be analyzed using similar tools or ideas to those introduced in this thesis. We also discuss possible generalizations and, in particular, we describe three problems that started to be investigated during the PhD thesis.

We begin this appendix by presenting these three problems and, in Section A.4, we briefly describe other possible research directions.

A.1 Rigid body with a rotor

The article [16] describes the dynamics of a rigid body with an attached rotor that can be switched on and off. This model describes, for example, the dynamics of a somersault for a diver. Applications can also be found in space mechanics on the dynamics of satellites. The equations of motion of this system are very similar to Euler's equations, except for some extra terms that we now describe. As before, we denote by (x, y, z) and (X, Y, Z) the body-fixed and the space-fixed frames respectively, and by (I_x, I_y, I_z) the moments of inertia characterizing the rigid body. We assume that the rotor leads to an additional (non-time dependent) angular momentum $\vec{A}$ along the z- axis[1], which can be switched on or off. For a diver, this additional angular momentum corresponds to the motion of the arms during a somersault.

The angular momentum of the body $\vec{L}$ has coordinates (L_x, L_y, L_z) and

[1]The case where the additional angular momentum is along the z-axis is the easiest to study due to some simplifications in the calculations.

fulfills

$$\vec{L} = I\vec{\Omega} + \vec{A},$$

where $\vec{\Omega}$ is the angular velocity of the rigid body and the vector $\vec{A}$ has the coordinates $(0, 0, A)$. The equations of motion can be written as $\dot{\vec{L}} = \vec{L} \times \vec{\Omega}$. Leading to

$$\begin{aligned}
\dot{L}_x &= (\frac{1}{I_z} - \frac{1}{I_y})L_y L_z - \frac{AL_y}{I_z} \\
\dot{L}_y &= (\frac{1}{I_x} - \frac{1}{I_z})L_x L_z + \frac{AL_x}{I_z} \\
\dot{L}_z &= (\frac{1}{I_y} - \frac{1}{I_x})L_x L_y
\end{aligned}$$

In [68], the phase portraits of this system are presented for some values of A. Moreover, Euler angles can be introduced as well for this system.

Using similar techniques as those introduced in this thesis, the different phase portraits of this system can be obtained. Using Euler angles, we can then describe different effects (an equivalent of the TRE for example) on this system as abelian integrals and, hence, provide a geometric analysis of the dynamics. We note that the addition of the rotor rotating in one or the other sense at a given speed breaks the symmetry of the system.

A.2 Tavis-Cummings model: Chern class and monodromy in higher dimensions

In chapter 8, the Jaynes-Cummings model was presented. This model has a generalization to higher dimensions (when considering more spins). This system is called the Tavis-Cummings model and we now present the model for two spins. The classical Tavis-Cummings model for two spins is defined in the phase space $S^2 \times S^2 \times \mathbb{R}^2$ by the Hamiltonian given by

$$H = 2\varepsilon_1 S_1^z + 2\varepsilon_2 S_2^z + \omega \bar{b} b + g(\bar{b} S_1^- + b S_1^+) + g(\bar{b} S_2^- + b S_2^+),$$

where ε_1, ε_2, ω, and g are real parameters representing, respectively, the frequencies of the spins and of the Harmonic oscillator and the coupling strength between the sub-systems. The coordinates describing the spin and the Harmonic oscillator are respectively denoted by (S_1^x, S_1^y, S_1^z), (S_2^x, S_2^y, S_2^z) and $(b, \bar{b})$, with the constraints

$$(S_1^z)^2 + S_1^+ S_1^- = S_0^2;\ (S_2^z)^2 + S_2^+ S_2^- = S_0^2.$$

Here, S_0 is a positive constant and S^+ and S^- are given by

$$S^+ = S^x + iS^y,$$
$$S^- = S^x - iS^y.$$

Finally, the system has the following Poisson brackets

$$\{b, \bar{b}\} = -i,$$
$$\{S^+, S^z\} = iS^+,$$
$$\{S^-, S^z\} = -iS^-,$$
$$\{S^+, S^-\} = -2iS^z.$$

For any number of spins, this system is a completely integrable system described by a spectral Lax pair. Generically, for three degrees of freedom systems, the singular values of the energy-momentum map are surfaces on $\mathbb{R}^3$. Nevertheless, for specific values of ω, ε_1, ε_2, S_0 and g, we have found an isolated curve of critical values, using the Lax pair. Moreover, this curve is not smooth and it is, in fact, a cusp. For each point of this curve, one can find a circle of critical points, in the respective fiber. Thus, this is a very degenerate case for which, the study of the Hamiltonian monodromy around this curve is an interesting problem.

Moreover, given the fact that for a 3-tori foliation over $\mathbb{R}^3$ with parameters, it is very degenerate to have an isolated curve of singular values it is still a possibility to find an isolated critical value, by choosing correctly the values of the parameters. If this is the case, then the Hamiltonian monodromy around this point is trivial and the study of the Chern class [28] could be a very interesting work. Since, to the best of our knowledge, no physical system with trivial monodromy and non-trivial Chern class has been found.

Finally, given the fact that this system has a spectral Lax pair for any number of spins, we consider that it could be a key system to investigate how to use spectral Lax pairs to study Hamiltonian monodromy in higher dimensions.

A.3 Hamiltonian monodromy and Montgomery phase: Monodromy vs Holonomy

The Montgomery phase, as described in Section 3.5, is the variation of a specific angle when we follow the flow of the system given by Euler's equations,

i.e., a holonomy phenomenon. On the other hand, the rotation number is one of the main ingredients in Hamiltonian monodromy as described in the second part of this thesis. We strongly believe that there is a link between the two main problems treated in this work, rotating rigid body dynamics and Hamiltonian monodromy.

This idea comes from the fact that in [38] some symmetries of Euler's equations are used to perform reductions and obtain a completely integrable system with two degrees of freedom. Then, an expression of the rotation number of this reduced system is obtained and it turns out to be equal to the Mongomery phase. Nevertheless, in this article, the Hamiltonian monodromy of the reduced system is not investigated since the set of regular values of the bifurcation diagram is not connected.

Thus, finding a way to study the Hamiltonian monodromy of this system (possibly by complexification) would link a holonomy phenomenon and a monodromy one through a formula, which would be a relevant property of this system and would give a nice connection between the first and second parts of this work. A similar discussion about monodromy vs holonomy can be found in [26].

A.4 Other problems

In this section, we briefly mention different problems as perspectives for further research. The first direction of research is the use of the algebraic structure of Lax pairs in other problems. For example, there exists a Lax pair for Euler's equations in higher dimensions (which is a generalization of the one introduced in Chapter 4). A specific problem in this context is to find robust "effects" like the TRE in higher dimensions using the Lax pair structure. The goal of doing this is, first, to understand the dynamics in higher dimensions and, second, to follow the ideas presented in [70] to construct convenient control fields using robust effects. Another problem is the study of Euler's equation in $\mathbb{R}^3$ with time-dependent moments of inertia. This idea has been investigated in [55].

On the other hand, following the guideline of applying existing theories in foliations to the study of physical systems, one interesting problem is to compare the two classifications of foliations near a pinched torus given in the papers [67] and [56]. On the first one, a classification of foliations obtained through completely integrable systems near a focus-focus singularity (which corresponds to a pinched point on a torus) is given. In the second one, a classification of complex foliations near a homoclinic loop (which corresponds to a pinched torus) is given. To relate these works is a natural

problem and could lead to generalizations, in particular, in the case of small deformations of the integrable systems.

Another relevant idea is to investigate which of the results obtained can be extended to quantum mechanics. That is, either to find signatures of the obtained results in quantum mechanics or to use the methods already described to obtain information on quantum systems. As an example of the first idea, in the paper [59] the classical and quantum control of rotating asymmetric molecules are studied. Hence, a question that arises is whether or not the physical and non-physical cases discussed in this thesis have different properties in this framework. Finally, an example of the second direction is to investigate the use of the Lax pair structure to describe quantum monodromy.

Bibliography

[1] R. Abraham and J. E. Marsden, *Foundations of Mechanics*, no. 364, American Mathematical Soc., 2008.

[2] J. Alonso, H. Dullin, and S. Hohloch, *Taylor series and twisting-index invariants of coupled spin-oscillators*, J. Geom. Phys. Vol.140 Pag.131, (2019).

[3] V. I. Arnold, *Mathematical Methods of Classical Mechanics*, Springer-Verlag, New York, 1989.

[4] V. I. Arnold, S. M. Goussein-Zade, and A. N. Varchenko, *Singularities of Differentiable Mappings*, Birkhauser, 1988.

[5] M. Ashbaugh, C. Chicone, and R. Cushman, *The twisting tennis racket*, J. Dyn. Diff. Equat., 3 (1991), p. 67.

[6] E. Assémat, K. Efstathiou, M. Joyeux, and D. Sugny, *Fractional bidromy in the vibrational spectrum of hocl*, Phys. Rev. Lett., 104 (2010).

[7] M. Audin, *Spinning tops: A course on integrable systems*, vol. 51, Cambridge University Press, 1999.

[8] M. Audin, *Hamiltonian monodromy via Picard-Lefschetz theory*, Comm. Math. Phys. Vol.229 Pag.459, (2002).

[9] O. Babelon, D. Bernard, and M. Talon, *Introduction to Classical Integrable Systems*, Cambridge University Press, 2003.

[10] O. Babelon and B. Dou¸cot, *A semi-classical study of the Jaynes-Cummings model*, J. Stat. Mech., (2009).

[11] O. Babelon and B. Douçot, *Classical Bethe ansatz and normal forms in an integrable version of the Dicke model*, Physica D Vol.241, (2012).

[12] ——, *Higher index focus-focus singularities in the Jaynes-Cummings-Gaudin model: Symplectic invariants and monodromy*, J. Geom. Phys. Vol.87 Pag.3, (2015).

[13] L. Bates, *Monodromy in the champagne bottle*, J. Appl. Math. Phys., 42 (1991).

[14] P. Ben, *Dancing t-handle in zero-g.* `https://youtu.be/1n-HMSCDYtM?si=ACgq8jTNb9b16X1Q`, March 2009. Last Checked: December 2023.

[15] F. Beukers and R. Cushman, *The complex geometry of the spherical pendulum*, Contemp. Math. Vol.292 Pag.47, (2002).

[16] S. Bharadwaj, N. Duignan, H. R. Dullin, K. Leung, and W. Tong, *The diver with a rotor*, Indagationes Mathematicae, 27 (2016), pp. 1147–1161.

[17] A. Bohm, A. Mostafazadeh, H. Koizumi, Q. Niu, and J. Zwanziger, *The Geometric Phase in Quantum Systems*, Springer, Berlin, 2003.

[18] A. V. Bolsinov and A. T. Fomenko, *Integrable Hamiltonian systems: Geometry, topology, classification*, CRC Press, (2004).

[19] C. Chann, *Monster flip/trick challenge.* `https://youtu.be/vkMmbWYnBHg?si=1vtOBDnoMVNk4b1C`, July 2015. Last Checked: December 2023.

[20] M. S. Child, *Quantum monodromy and molecular spectroscopy*, Adv. Chem. Phys., 136 (2007), p. 39.

[21] S.-N. Chow and J. K. Hale, *Methods of Bifurcation Theory*, vol. 251, Springer Science & Business Media, 2012.

[22] R. H. Cushman and L. Bates, *Global Aspects of Classical Integrable Systems*, Birkhauser, Basel, 1997.

[23] R. H. Cushman and J. J. Duistermaat, *The quantum mechanical spherical pendulum*, Bull. Amer. Math. Soc. Vol.19 Pag.475, (1988).

[24] R. H. Cushman, H. R. Dullin, A. Giacobbe, M. Joyeux, P. Lynch, D. A. Sadovskii, and B. I. Zhilinskii, *Co2 molecule as a quantum realization of the* $1:1:2$ *resonant swing-spring with monodromy*, Phys. Rev. Lett., 93 (2004).

[25] R. H. Cushman and D. Sadovskii, *Monodromy in the hydrogen atom in crossed fields*, Physica D, 65 (2000), p. 166.

[26] M. Dauge, M. A. Hall, and S. V. Ngoc, *Asymptotic lattices, good labellings, and the rotation number for quantum integrable systems*, Discrete and Continous Dynamical Systems, (2022).

[27] R. H. Dicke, *Coherence in spontaneous radiation processes*, Phys. Rev. Vol.93 Pag.99, (1954).

[28] J. J. Duistermaat, *On global action-angle coordinates*, Comm. Pure Appl. Math., (1980).

[29] H. R. Dullin and H. Waalkens, *Defect in the joint spectrum of hydrogen due to monodromy*, Phys. Rev. Lett., 120 (2018).

[30] K. Efstathiou, *Metamorphoses of Hamiltonian Systems with Symmetries*, Springer, 2005.

[31] K. Efstathiou, A. Giacobbe, P. Mardesic, and D. Sugny, *Rotation forms and local hamiltonian monodromy*, J. Math. Phys. Vol.58, (2017).

[32] L. Gavrilov, *Jacobians of singularized spectral curves and completely integrable systems*, Kovalevski property, CRM Proceedings and Lectures Notes Vol.32 Pag.59, (2002).

[33] P. Girl, *Why this trick should be impossible ft. Rodney Mullen-skateboarding science.* `https://youtu.be/yFRPhi0jhGc?si=W8RI_Ksoi1HyS-J_`, May 2018. Last Checked: December 2023.

[34] H. Goldstein, *Classical Mechanics*, Addison-Wesley, Reading, MA, 1950.

[35] V. Guillemin and A. Uribe, *Monodromy in the quantum spherical pendulum*, Comm. Math. Phys. Vol.122 Pag.563, (1989).

[36] G. Gutierrez, A. Arroyo, P. Mardesic, and D. Sugny, *Signatures of physical constraints in rotating rigid bodies*, Journal of Physics A: Mathematical and Theoretical, (2023).

[37] G. Gutierrez Guillen, D. Sugny, and P. Mardešić, *Hamiltonian monodromy via spectral Lax pairs*, Journal of Mathematical Physics, 65 (2024).

[38] K. Hamraoui, L. Van Damme, P. Mardešić, and D. Sugny, *Classical and quantum rotation numbers of asymmetric-top molecules*, Phys. Rev. A, 97 (2018), p. 032118.

[39] E. Jaynes and F. Cummings, *Comparison of quantum and semi-classical radiation theories with application to the beam maser*, Proc. IEEE Vol.51 Pag.89, (1963).

[40] M. Kloc, P. Strnasky, and P. Cejnar, *Monodromy in Dicke superradiance*, J. Phys. A: Math. Gen. Vol.50, (2017).

[41] L. D. Landau and E. M. Lifshitz, *Mechanics*, Pergamon Press, Oxford, 1960.

[42] P. D. Lax, *Integrals of nonlinear equations of evolution and solitary waves*, Comm. Pure Appl. Math., 21 (1968), p. 467.

[43] J. M. Lee and J. M. Lee, *Smooth Manifolds*, Springer, 2012.

[44] M. Levi, *Geometric phases in the motion of rigid bodies*, Arch. Rational Mech. Anal., 122 (1993), pp. 213–229.

[45] P. Libermann and C.-M. Marle, *Symplectic geometry and analytical mechanics*, vol. 35, Springer Science & Business Media, 2012.

[46] O. Lukina, F. Takens, and H. Broer, *Global properties of integrable Hamiltonian systems*, Regular and Chaotic Dynamics, 13 (2008), pp. 602–644.

[47] Y. Ma, K. E. Khosla, B. A. Stickler, and M. S. Kim, *Quantum persistent tennis racket dynamics of nanorotors*, Phys. Rev. Lett., 125 (2020), p. 053604.

[48] P. Mardešić, G. J. Gutierrez Guillen, L. Van Damme, and D. Sugny, *Geometric origin of the tennis racket effect*, Phys. Rev. Lett., 125 (2020), p. 064301.

[49] N. Martynchuk, H. W. Broer, and K. Efstathiou, *Hamiltonian monodromy and Morse theory*, Commun. Math. Phys., 375 (2020).

[50] R. Miranda, *Algebraic Curves and Riemann Surfaces*, American Mathematical Society, 1995.

[51] R. Montgomery, *How much does the rigid body rotate? a Berry's phase from the 18th century*, American Journal of Physics, 59 (1991), pp. 394–398.

[52] J. Natário, *An elementary derivation of the Montgomery phase formula for the Euler top*, Journal of Geometric Mechanics, 2 (2010), pp. 113–118.

[53] N. N. Nekhoroshev, D. A. Sadovskii, and B. I. Zhilinskii, *Fractional Hamiltonian monodromy*, Ann. Henri Poincaré, 7 (2006).

[54] O. O'Reilly, *Intermediate Dynamics for Engineers: Newton-Euler and Lagrangian Mechanics*, Cambridge, Cambridge University Press, 2020.

[55] I. Ostanin and M. Sperl, *Arbitrary controlled re-orientation of a spinning body by evolving its tensor of inertia*, 2023.

[56] D. Panazzolo, M. Resman, and L. Teyssier, *Rigidity of saddle loops*, 2021.

[57] A. Pelayo and S. Vu Ngoc, *Hamiltonian dynamical and spectral theory for spin-oscillators*, Commun. Math. Phys. Vol.309 Pag.123, (2012).

[58] A. G. Petrov and S. E. Volodin, *Janibekov's effect and the laws of mechanics*, Dokl. Phys., 58 (2013), pp. 349–353.

[59] E. Pozzoli, *Classical and quantum controllability of a rotating asymmetric molecule*, Appl. Math. Optim., 85 (2022), p. 8.

[60] J. M. Raimond, M. Brune, and S. Haroche, *Manipulating quantum entanglement with atoms and photons in a cavity*, Rev. Mod. Phys. Vol.73 Pag.565, (2001).

[61] D. Russell, *Tennis racket theorem.* `https://youtu.be/4dqCQqI-Gis?si=gOgi_Mx3fYf34zz8`, March 2010. Last Checked: December 2023.

[62] D. A. Sadovskii and B. I. Zhilinskii, *Monodromy, diabolic points, and angular momentum coupling*, Phys. Lett. A, 256 (1999), p. 235.

[63] V. N. San, *Quantum monodromy and bohr–sommerfeld rules*, Letters in Mathematical Physics, 55 (2001), pp. 205–217.

[64] S. Smale, *Topology and mechanics i*, Inventiones mathematicae, 10 (1970), pp. 305–331.

[65] E. C. G. Sudarshan and N. Mukunda, *Classical dynamics: a modern perspective*, World Scientific, 1974.

[66] D. Sugny, P. Mardesic, M. Pelletier, A. Jebrane, and H. R. Jauslin, *Fractional Hamiltonian monodromy from a Gauss-Manin monodromy*, J. Math. Phys., 49 (2008).

[67] S. Vũ Ngoc, *On semi-global invariants for focus–focus singularities*, Topology, 42 (2003), pp. 365–380.

[68] L. Van Damme, *Contrôle optimal de la dynamique des spins: Applications en Résonance Magnétique Nucléaire et en Information Quantique*, Doctoral dissertation, Université de Bourgogne-Franche Comté, 2016.

[69] L. Van Damme, D. Leiner, P. Mardesic, S. J. Glaser, and D. Sugny, *Linking the rotation of a rigid body to the Schrödinger equation: The quantum tennis racket effect and beyond*, Sci. Rep., 7 (2017), p. 3998.

[70] L. Van Damme, P. Mardešić, and D. Sugny, *The tennis racket effect in a three-dimensional rigid body*, Physica D: Nonlinear Phenomena, 338 (2017), pp. 17–25.

[71] Veritasium, *The bizarre behavior of rotating bodies.* `https://youtu.be/1VPfZ_XzisU?si=UkOTdFmDEqAYFpVY`, September 2019. Last Checked: December 2023.

[72] S. Vu Ngoc, *Quantum monodromy in integrable systems*, Comm. Math. Phys. Vol.203 Pag.465, (1999).

[73] S. Vũ Ngoc, *Bohr-Sommerfeld conditions for integrable systems with critical manifolds of focus-focus type*, Communications on Pure and Applied Mathematics: A Journal Issued by the Courant Institute of Mathematical Sciences, 53 (2000), pp. 143–217.

[74] M. S. Wheatland, T. Murphy, D. Naoumenko, D. v. Schijndel, and G. Katsifis, *The mobile phone as a free-rotation laboratory*, American Journal of Physics, 89 (2021), pp. 342–348.

[75] H. Żołądek, *The Monodromy Group*, vol. 67, Springer, 2006.

[76] N. T. Zung, *A note on focus-focus singularities*, Differential Geom. Appl., 7 (1997), p. 123.